Modélisation de la dynamique de spin d'un atome magnétique individuel dans une boîte quantique

Chong Long Cao

UNIVERSITÉ DE GRENOBLE

THÈSE

Pour obtenir le grade de

DOCTEUR DE L'UNIVERSITÉ DE GRENOBLE

Spécialité : **Physique**

Arrêté ministériel : 7 août 2006

Présentée par

Chong Long CAO

Thèse dirigée par **H. MARIETTE**
et codirigée par **L. BESOMBES , J. FERNANDEZ-ROSSIER**

préparée au sein de **l'Institut Néel, CNRS**
dans **l'École Doctorale de Physique**

Modélisation de la dynamique de spin d'un atome magnetique individuel dans une boite quantique

Thèse soutenue publiquement le **13 janvier 2012**,
devant le jury composé de :

Mr Ramón AGUADO
Senior Researcher, Instituto de Ciencia de Materiales de Madrid, Rapporteur
Mr Paul M. KOENRAAD
Prof., Eindhoven University of Technology, Rapporteur
Mr Philippe PEYLA
Prof., Université Joseph Fourier, Membre
Mr Joaquín FERNANDEZ-ROSSIER
Prof., International Iberian Nanotechnology Laboratory, Membre
Mr Lucien BESOMBES
CR, Institut Néel CNRS, Membre
Mr Henri MARIETTE
DR, Institut Néel CNRS and CEA/INAC/SP2M, Membre

Contents

Introduction

The tremendous progress in the miniaturization of electronic devices has reached the point that makes it crucial to address the effect of a single dopant in a device and motivates the study of a single dopant spin to store digital information (1). The manipulation of a single atom spin in a solid state environment has been demonstrated using several approaches, like scanning tunnelling microscope on magnetic adatoms (2, 3), or optical probing of nitrogen-vacancy centres in diamond (4) and single magnetic atoms in semiconductor quantum dots. Single quantum dots doped with a single Mn atom can be probed by means of single exciton spectroscopy in photoluminescence experiments. This has been done both in II-VI (5, 6), and III-V (7, 8) materials. In the case of single Mn doped CdTe dots, information about the quantum spin state of a single Mn atom is extracted from the single exciton quantum dot photoluminescence due to the one on one relation between photon energy and polarization and the electronic spin state of the Mn atom. This has made it possible to measure the spin relaxation time of a single Mn atom in a quantum dot, using photon autocorrelation measurements (9), and to realize the optical initialization and readout of the spin of the Mn atom (6, 10, 11). The observation of Mn spin orientation under quasiresonant optical pumping can be accounted for if the Mn spin relaxation time is shorter in the presence of a quantum dot exciton (11, 12, 13, 14). In that situation, resonant excitation of an optical transition associated to a given Mn spin projection results in the depletion of the laser driven Mn spin state, via Mn spin relaxation in the presence of the exciton. Whereas theoretical understanding of the exchange couplings between electrons, holes and Mn spin in quantum dots permits to account for the observed photoluminescence spectra (5, 15, 16, 17), a complete understanding of the spin dynamics under the combined action of laser pumping, incoherent spin relaxation and coherent spin-flips is still missing. Here, in thesis, we will discuss the spin relaxation mechanism, taking fully into account the interplay between incoherent dynamics due to the coupling to a reservoir and the coherent spin flips associated to exciton-Mn exchange in the quantum dot.

The aim of this Ph.D thesis is to further investigate the spin relaxation mechanism in a CdTe semiconductor quantum dot containing an individual Mn atom first observed

in Grenoble in 2004. Full investigation of spin relaxation mechanism due to spin-phonon coupling are discussed in detail. The coherent evolution of states are also discussed at the end of this thesis. The spin-phonon coupling relaxation mechanism explains the Mn-spin polarization mechanism observed in resonant time resolved optical pumping experiments.

This thesis is organized as follows: In chapter 1, we present basic background on spintronics, diluted magnetic semiconductors and quantum dots. In chapter 2, we present a summary of some recent experimental results on the optical pumping of a Mn spin in a single quantum dot. Chapter 3, 4, 5, and 6 constitute the central part of this work. In chapter 3, a theoretical model of the quantum dot and its corresponding Hamiltonian are described. A model is introduced to describe the mixing of the valence bands. Then, a spin effective Hamiltonian is used to model the details of the optical spectrum of quantum dots containing one or two Mn atoms. This model is compared with experiments. In chapter 4, the coupling between spin and phonon in a single quantum dot with a single Mn atom is discussed. In chapter 5, The spin dynamics is analyzed using a rate equation model for the exciton-Mn system and calculated phonon induced spin flip rates. Chapter 6 discusses the coherent evolution of the exciton and Mn system under the combined action of resonant laser and microwave excitation. Concluding remarks are given in chapter 7. Some details on the calculation of the valence band structure in quantum dots are discussed in the appendix.

1

Spintronics, diluted magnetic semiconductors and quantum dots

Contents

Since the 60's, the density of transistors integrated on a microprocessor doubles every 18 months, driven by Moore's law. The last generation of MOS transistors, has typical dimensions below 45 nm. At a length scale of a few nm, pure quantum effects like energy quantization in the channel of the transistor or tunneling from the gate to the channel, will strongly degrade the performances of this device. CMOS technology scaling to smaller and smaller dimensions is therefore likely to be compromised by these quantum effects and fundamental limits of miniaturization are expected to be reached in the near future, even if progress in materials can still significantly improve transistor performance. Nevertheless, quantum physics provides new principles for information processing. The inexorable decrease of structure size in semiconductor devices inevitably leads from todays quasiclassical devices to quantum mechanical

devices. These quantum mechanical devices might rely not only on the charge of electrons, i.e., on the spatial part of the electron wave function, but also on the much more robust spin part of the wave function.

1.1 Spintronics

Spintronics, is an emerging technology which has recently become one of the key research areas connected with the magnetic-recording and semiconductor industries. It tries to answer the question: can magnetic materials be used in electronic components and circuits? The hope of using the spins of single electrons, rather than their charge, for storing, transmitting and processing quantum information invoked a great deal of interest in spin effects and magnetism in semiconductors. Spintronics emerged from discoveries in the 1980s concerning spin-dependent electron transport phenomena in solid-state devices. This includes the observation of spin-polarized electron injection from a ferromagnetic metal to a normal metal by Johnson and Silsbee (1985) (18) and the discovery of giant magnetoresistance independently by Albert Fert et al. (19) and Peter Grunberg et al. (1988) (20).

The use of semiconductors for spintronics can be traced back at least as far as the theoretical proposal of a spin field-effect-transistor by Datta and Das in 1990. The robustness of the electron spin motivates the current extensive research on the spin dynamics in semiconductors and might lead to spintronic devices with superior functionality and to the enchanting goal of spin quantum information processing. A valuable testing ground for spintronics, for various theoretical ideas and device applications, comes from the diluted magnetic (also called semimagnetic) semiconductors.

Thanks to the increase of purity of semiconductor materials, besides the study of spintronics for a spin ensemble, the study of one single spin also becomes possible. For example, the nitrogen-vacancy centers in diamond (21), the isolated Mn spin in a CdTe quantum dot (5) and a single phosphorous dopant in a nano-FET (22) are possible ways to study single dopant spin properties. These examples may be viewed as the initial demonstrations of model single spin devices, which requires considerable additional fundamental study. These single-spins can be addressed and manipulated in various ways, for example, the Mn spin can be addressed and manipulated optically using microspectroscopy (23) in single Mn doped quantum dots. Individual Mn atoms can also be addressed in III-V Material by scanning tunneling microscopy (24) (Figure 1.1). The desirable features of single dopants, such as reproducible quantized properties, make them ideal objects for further scientific study and robust applications. However, it is still a challenge to control the properties of a single dopant because their properties strongly depends on their local environment (strain, electronic, magnetic and optical fields). In this thesis, we focus on the influence of the environment on the spin dynamics

of a Mn atom embedded in a CdTe quantum dots.

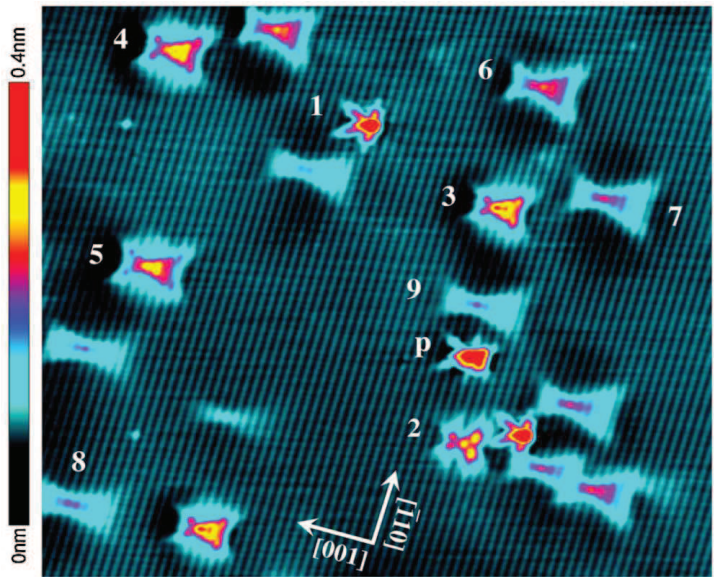

Figure 1.1: $(45 \times 35\ nm^2)$ constant-current topography map of the GaAs(110) surface showing a number of Mn acceptors in their neutral charge state. The numbers correspond with the atomic layer position of the Mn acceptors in GaAs. See reference (24).

1.2 Diluted magnetic semiconductors

Diluted magnetic semiconductors (DMS) are semiconducting alloys whose lattice is made up in part of substitutional magnetic atoms, it forms a class of magnetic materials, filling the gap between ferromagnets and semiconductors. In the early literature these DMS were often named semimagnetic semiconductors, because they are midway between nonmagnetic and magnetic materials. DMS are semiconductor compounds $A_{1-x}M_xB$ in which a fraction x of the cations is substituted by magnetic impurities (Mn, Co ...), thereby introducing magnetic properties into the host semiconductor AB. They can be II-VI materials like CdTe or ZnSe, IV-VI materials like PbTe or SnTe, or III-V materials like GaAs or InSb. These DMS exhibit exciting phenomena like giant magneto resistance and giant Faraday rotation.

With the fabrication of semiconductor nanostructures being well known, the search for the benefits of nanoscale structures made from DMS began. Among the principal DMS families, II-VI and, to a less extent, III-V based DMS, with Mn as the magnetic impurity, are the best understood. The band structures of DMS are quite similar to those of their host II-VI or III-V compounds. They exhibit the band structures of zinc-blende or wurtzite semiconductors, and, except for some III-V compounds, they

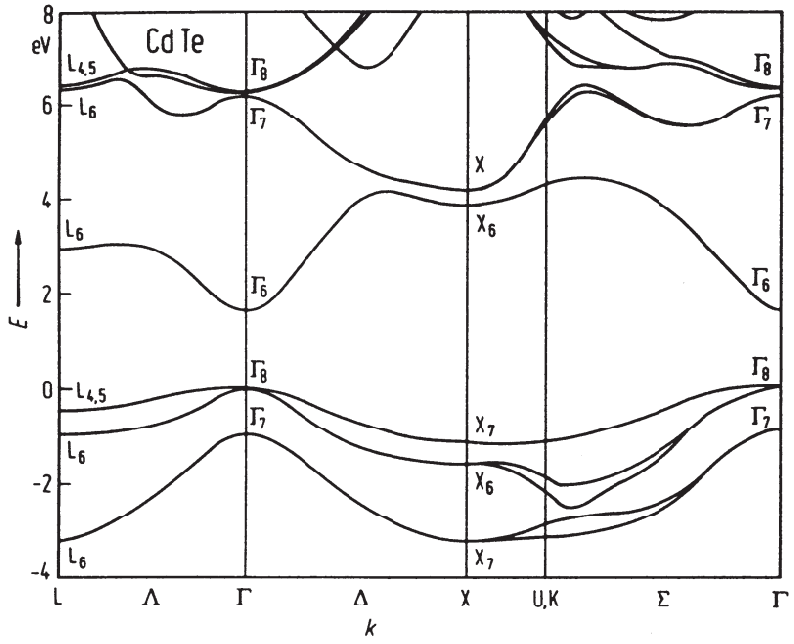

Figure 1.2: Band structure of CdTe

possess a direct band gap (Figure 1.2). But in addition, the d-states of the Mn atoms, with a more or less localized character, contribute to the total density of states, and they are responsible for the important magnetic properties of DMS.

In II-VI based DMS, Mn atoms behave as isoelectronic impurities, and in general do not introduce bound states. The two 4s electrons of Mn atoms participate to the covalent bonding, while the Mn d shell remains relatively inert. Hence, in zero magnetic field, the semiconducting properties of DMS look like those of non magnetic II-VI alloys. As in other standard alloys, DMS exhibit a shift of the energy gap with Mn concentration, and alloy fluctuations responsible for potential fluctuations, and eventually tails of localized states at the band edges. In III-V DMS, Mn atoms introduce energy levels in the gap of the semiconductor. In the best understood case of antimonides and arsenides, Mn behaves as a shallow acceptor. It keeps its d5 configuration and is surrounded by a weak bound hole.

When a magnetic field is applied, or a spontaneous magnetization appears, magnetic properties of DMS come into play. The pd hybridization is essential to understand magnetic and magneto-optical properties of DMS. This leads to a strong exchange interaction between holes in the valence band and Mn atoms. Therefore the magnetic properties of DMS depend critically on pd hybridization and on the positions of d-levels in the host band structure (Figure 1.3 (25)). These positions determine the

energy needed to promote an electron from the occupied d-level of the Mn to the top of the valence band (d5/d4 donor level), or to promote an electron from the top of the valence band to the unoccupied d-level (d5/d6 acceptor level). In the latter case there is an extra energy cost due to the intra-d-shell Coulomb energy (the energy to be paid to add an electron on the Mn d orbitals).

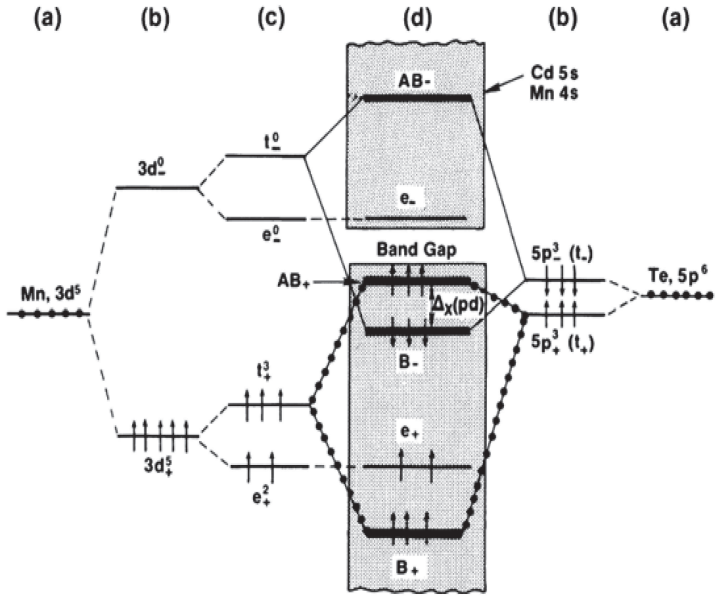

Figure 1.3: Schematic diagram of the p-d hybridization in CdMnTe (a) Atomic unpolarized levels, (b) exchange-split atomic levels, (c) crystal-field split levels, (d) final interaction states. (see (25))

DMS of the II-VI type are of special interest for several distinct reasons. Their ternary nature offers the possibility of tuning the lattice constant, band parameters and magneto-optical properties by the band structure and magnetic ion concentrations. The techniques developed for semiconductor heterostructures enable incorporation of DMS layers into quantum wells, quantum dots and other electro-optical devices in which the spin splitting can also be tuned by the confinement energy and the size quantization. The presence of localized magnetic ions in these semiconductor alloys leads to an extremely large Zeeman splittings of electronic levels. This selective amplification of spin-dependent properties leads to new effects, such as the giant Faraday rotation, the magnetic-field-induced metal-insulator transition, and the formation of bound magnetic polarons.

1.3 Diluted magnetic semiconductor quantum dots

A quantum dot, also called artificial atom, is a semiconductor nanostructure where the electrons are confined in all three spatial directions in nanometer scale, which leads to the formation of discrete energy levels. The properties of quantum dots can be controlled by the material and their shape, which can be controlled by the growth process. There are several fabrication methods, the most prominent being self-assembled growth, also known as Stranski-Krastanov growth. Semiconductor quantum dots have been the subject of research for about 30 years. They are expected to become a basic ingredient for many applications in optics and optoelectronics in the near future. Since the proposal of Di Vincenzo and Loss, quantum dots are moreover dealt as promising candidates for qubits in a quantum computer (26).

1.3.1 State of the art

Carrier-Mn coupling was mostly studied in bulk DMS made of II-VI semiconductors in which Mn impurities were introduced (see the review papers (27, 28)). In these materials, Mn impurities have the d^5 electronic configuration and substitute the cations from column II (Zn, Cd or Hg) up to 100%. An important point for the study of magnetic quantum dots is that Mn is an isoelectronic impurity in II-VIs - by contrast to the acceptor character observed in GaAs and similar III-Vs (29, 30). The Mn ground state is 6S, introducing localized spins with S=5/2. If not interacting, these localized spins follow Maxwell-Boltzmann statistics, resulting in a magnetization induced by an applied field given by a Brillouin function. Optical spectroscopy around the bandgap reveals the giant Zeeman effect, with a spin splitting proportional to the Mn magnetization (31). Several studies have demonstrated this proportionality and measured the strength of the coupling (32). Magneto-optical spectroscopy is now a very sensitive method for measuring locally the magnetization of the Mn system (33). Altogether, this excellent knowledge of II-VI DMS, and of the coupling between the localized spins and carriers, constitutes a very firm basis for the further studies described below.

In a magnetic quantum dot, the sp-d interaction takes place with a single carrier or a single electron-hole pair. However, besides effects related to the carriers-Mn exchange interaction such as giant Zeeman shift, it was found that even a small content of Mn introduced in a II-VI semiconductor material can strongly suppress photoluminescence (PL) if the energy gap E_g exceeds the energy of the Mn internal transition. This strongly limits the study of individual DMS quantum dots (34). The first studies of individual quantum dots doped with Mn atoms were reported by Maksimov et al (35). They studied CdMnTe quantum dots inserted in CdMgTe barriers in which the optical transition energies are lower than the energy of the internal transition of the Mn atom. This suppresses the non-radiative losses due to the transfer of confined carriers to

the Mn internal levels. This system allowed observing the formation of quasi zero-dimensional magnetic polaron.

Another way to reduce the non-radiative losses was to introduce the magnetic atoms in the quantum dots barriers. This was realized for self-assembled CdSe dots embedded in ZnMnSe barriers by Seufert et al. (36). In this system, the interaction between the confined exciton and the magnetic atoms is due to the spread of the wave function in the barriers and to a small diffusion of the magnetic atoms in the quantum dots. In these DMS structures, the formation of a ferromagnetically aligned spin complex was demonstrated to be surprisingly stable as compared to bulk magnetic polaron (37, 38) even at elevated temperature and high magnetic fields. The PL of a single electron-hole pair confined in one magnetic quantum dot, which sensitively depends on the alignment of the magnetic atoms spins, allowed to measure the statistical fluctuation of the magnetization on the nanometer scale. Quantitative access to statistical magnetic fluctuations was obtained by analyzing the linewidth broadening of the single dot emission. This all optical technique allowed to address a magnetic moment of about 100 μ_B and to resolve changes in the order of a few μ_B (39, 40, 41).

A huge effort has also been done to incorporate magnetic ions in chemically synthesized II-VI nanocrystals (42). The incorporation of the magnetic atoms is strongly dependent on the growth conditions and controlled by the adsorption of atoms on the nanocrystal surface during growth (43). The doping of nanocrystals with magnetic impurities also leads to interesting magneto-optical properties (44) but once again, in these highly confined systems, the transfer of confined carriers to the Mn internal levels strongly reduces their quantum efficiency and prevents the optical study of individual Mn-doped nanocrystals. However, by looking to magnetic circular dichroism absorption spectra, it is possible to observe a giant excitonic Zeeman splitting and to deduce directly the sp-d exchange interaction (45). Recently, a very robust light induced spontaneous spin polarization (46) was obtained in large CdSe nanocrystals containing a few percent of Mn and emitting at lower energy than the internal transition of the Mn.

1.3.2 Magnetic Cd(Mn)Te quantum dots

In this thesis, we focus on self-assembled CdTe quantum dots grown on a ZnTe substrate. Theorefore, in this section, we first discuss the band structure of bulk CdTe and then present the CdTe quantum dots modeled in our theory.

The band structure of CdTe is shown in Figure 1.2. CdTe has a Zinc-Blende type structure: Cd and Te atoms are both on a face-centered cubic crystal, the two lattice are shifted from each other by a quarter of the [111] diagonal. Hence CdTe has a T_d symmetry. As shown in Figure 1.2, the valence band splits into two banches near the Γ_8 point. The one with the smallest curvature (highest effective mass) is called the heavy-hole band and the other is called the light-hole band. If we include spin-

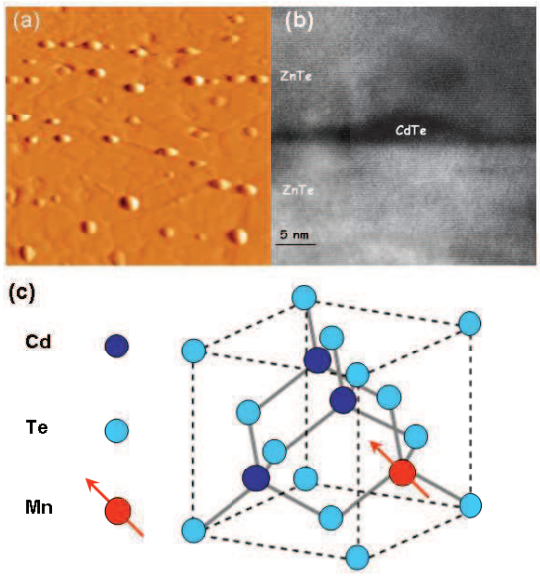

Figure 1.4: (a) AFM image of a CdTe surface deposited on a ZnTe substrate before deposition of a ZnTe capping layer. (b) High resolution TEM image showing the structure of a CdTe/ZnTe quantqum dot. (c) Crystalline structure of CdTe with the substitution of a Cd atom by a magnetic Mn atom.

orbit coupling, the valence band maximum with $L = 1$ is split into a quadruplet with $J = 3/2$ (Γ_8 point) and at lower energy, a doublet with $J = 1/2$ (Γ_7 point). The energy splitting at the Γ point between the valence band and the split-off band (Γ_7) is 0.9eV approximately for CdTe and ZnTe. The valence band eigenstates at the Γ point can be expressed as a function of the three electronic states $|X>$, $|Y>$, $|Z>$ and the spin-states $|\uparrow>$ and $|\downarrow>$. We define the eigenstates of $L_z = 0, \pm 1$:

$$\begin{aligned} |+1\rangle &= -\frac{|X\rangle + i|Y\rangle}{\sqrt{2}} \\ |0\rangle &= |Z\rangle \\ |-1\rangle &= \frac{|X\rangle - i|Y\rangle}{\sqrt{2}} \end{aligned} \tag{1.1}$$

The composition with the 1/2 spin leads to:

$$\begin{aligned} \Gamma_6 : \quad & |\frac{1}{2}, \frac{1}{2}\rangle = |S\rangle|\uparrow\rangle \\ & |\frac{1}{2}, -\frac{1}{2}\rangle = |S\rangle|\downarrow\rangle \end{aligned}$$

$$
\begin{aligned}
\Gamma_8 : \quad & |\frac{3}{2},\frac{1}{2}\rangle = \sqrt{\frac{2}{3}}|0\rangle|\uparrow\rangle + \sqrt{\frac{1}{3}}|1\rangle|\downarrow\rangle \\
& |\frac{3}{2},-\frac{1}{2}\rangle = \sqrt{\frac{2}{3}}|0\rangle|\downarrow\rangle + \sqrt{\frac{1}{3}}|-1\rangle|\uparrow\rangle \\
& |\frac{3}{2},\frac{3}{2}\rangle = |1\rangle|\uparrow\rangle \\
& |\frac{3}{2},-\frac{3}{2}\rangle = |-1\rangle|\downarrow\rangle
\end{aligned}
\tag{1.2}
$$

$$
\begin{aligned}
\Gamma_7 : \quad & |\frac{1}{2},\frac{1}{2}\rangle = \sqrt{\frac{2}{3}}|1\rangle|\downarrow\rangle - \sqrt{\frac{1}{3}}|0\rangle|\uparrow\rangle \\
& |\frac{1}{2},-\frac{1}{2}\rangle = -\sqrt{\frac{2}{3}}|-1\rangle|\uparrow\rangle + \sqrt{\frac{1}{3}}|0\rangle|\downarrow\rangle
\end{aligned}
$$

These eigenstates give directly the optical selection rules at the Γ point. In chapter 3, we will discuss in detail the eigenstates of holes (Γ_8 band) in quantum dots using Kohn-Luttinger and Bir-Pikus Hamiltonian and derive the effective interacting Hamiltonian between hole and Mn spins.

Self-assembled quantum dots based on CdTe usually present an emission energy below the internal transition of the Mn atom. The incorporation of magnetic atoms is then possible without loosing the good optical properties of these quantum dots. Most of the experimental studies on these quantum dots are focused on the interaction of a single carrier spin with its paramagnetic environment (large number of magnetic atoms) (47, 48). CdTe/ZnTe quantum dots structures doped with a low density of Mn allow to control optically the spin states of a single magnetic atom interacting with a single electron-hole pair or a single carrier (49).

The CdTe/ZnTe quantum dots samples used in our study (Figure 1.4) are all grown on ZnTe substrates. A 6.5- monolayer-thick CdTe layer is deposited by atomic layer epitaxy on a ZnTe barrier grown by molecular beam epitaxy. The dots are formed by the well-established Tellurium deposition/desorption process (50) and protected by a 100-nm-thick ZnTe top barrier. Single Mn atoms are introduced in CdTe/ZnTe quantum dots during their growth adjusting the density of Mn atoms to be roughly equal to the density of quantum dots (51). The height of the quantum dots core is a few nanometers and their diameter is in the 10 nm range.

1.4 Singly Mn doped CdTe quantum dots

Micro-spectroscopy can be used to study the magneto-optical properties of individual CdTe/ZnTe quantum dots containing an individual Mn atom. Typical PL and PL

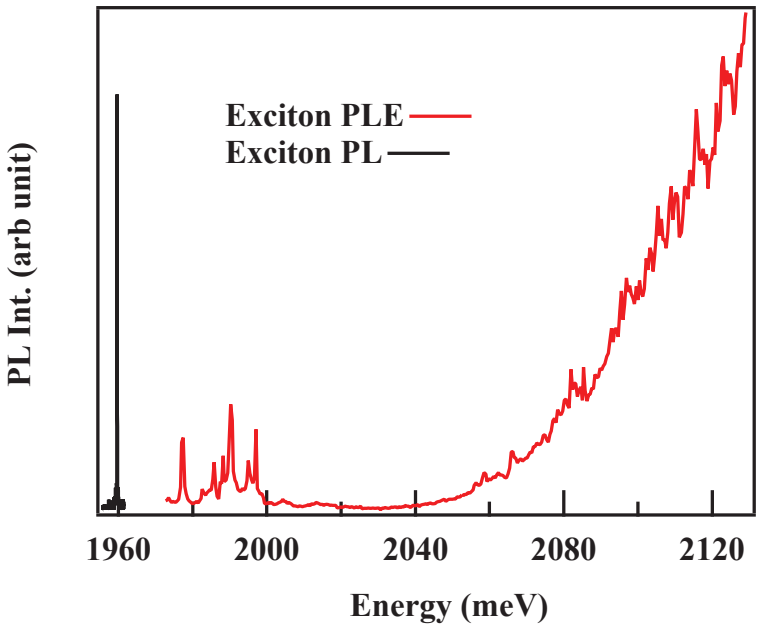

Figure 1.5: Photoluminescence and photoluminescence excitation spectra of an exciton in a single CdTe/ZnTe quantum dot.

excitation spectra of an exciton in a single CdTe/ZnTe quantum dot are shown on Figure 1.5.

In Figure 1.6, PL spectra of an individual Mn-doped quantum dot are compared to those of a non-magnetic CdTe/ZnTe reference sample. In non-magnetic samples, narrow PL peaks can be resolved, each attributed to the recombination of a single electron-hole pair in a single quantum dot. The emission of neutral quantum dots is split by the e-h exchange interaction and usually a linearly polarized doublet is observed (11). On the over hand, most of the individual emission peaks of magnetic single quantum dots are characterized by a rather large linewidth of about 0.5 meV. For some of these quantum dots, a fine structure can be resolved and six emission lines are clearly observed at zero magnetic field. The measured splitting changes from dot to dot. This fine structure splitting as well as the broadening is obviously related to the influence of the magnetic ions located within the spatial extent of the exciton wave function. The broadening observed in magnetic quantum dots has been attributed by Bacher *et al.* to the magnetic fluctuations of the spin projection of a *large number* of Mn spins interacting with the confined exciton (39). In the low concentration Mn-doped samples, the observation of a fine structure shows that the quantum dot exciton interacts with a single Mn spin. In time-averaged experiments, the statistical fluctuations of a single Mn spin (M=5/2) can be described in terms of populations of its six spin states quantized

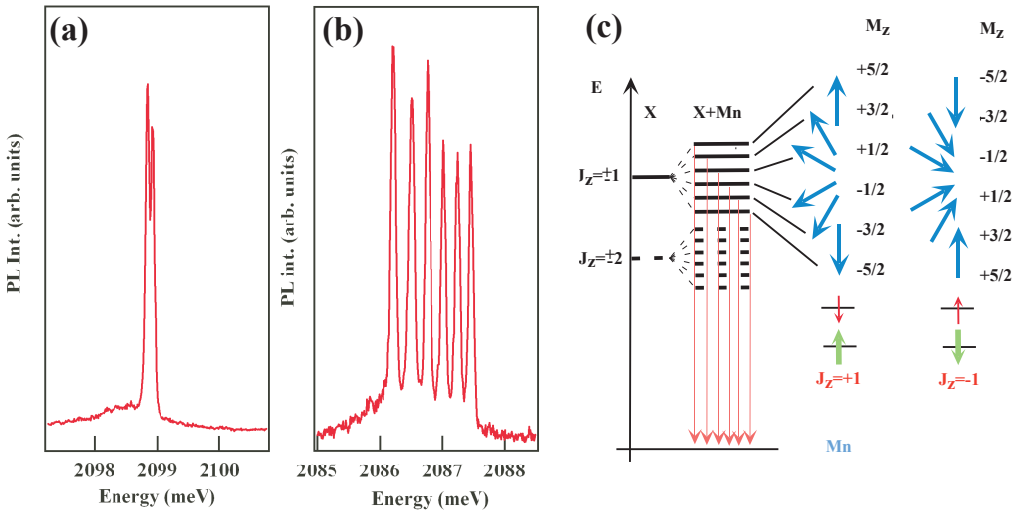

Figure 1.6: Low temperature (T=5K) PL spectra obtained at B=0T for an individual CdTe/ZnTe quantum dot (a) and a Mn-doped quantum dot (b). (c) Scheme of the energy levels of the Mn-exciton coupled system at zero magnetic field. The exciton-Mn exchange interaction shift the energy of the exciton depending on the S_z component of the Mn spin projection.

along the direction normal to the quantum dot plane. The exchange interaction of the confined exciton with the Mn atom shifts its energy depending on the Mn spin projection.

At zero magnetic field, the quantum dot emission presents a fine structure composed of six doubly degenerated transitions roughly equally spaced in energy. The lower energy bright states, $|+1/2\rangle_e|-3/2\rangle_h|+5/2\rangle_{Mn}$ and $|-1/2\rangle_e|+3/2\rangle_h|-5/2\rangle_{Mn}$ are characterized by an anti-ferromagnetic coupling between the hole and the Mn atom. The following states are associated with the Mn spin projections $S_z = \pm 3/2, \pm 1/2$ until the higher energy states $|-1/2\rangle_e|+3/2\rangle_h|+5/2\rangle_{Mn}$ and $|+1/2\rangle_e|-3/2\rangle_h|-5/2\rangle_{Mn}$ corresponding to ferromagnetically coupled hole and manganese. In this simple model the zero field splitting $\delta_{Mn} = \frac{1}{2}(j_e - 3j_h)$ depends only on the electron-Mn exchange integral (j_e) and hole-Mn exchange integral (j_h). As we will see, they are related to the position of the Mn atom within the exciton wave function.

When an external magnetic field is applied in the Faraday geometry (Figure 1.7), each PL peak is further split and twelve lines are observed, six in each circular polarization. The Zeeman effect of the Mn states is identical in the initial and final states of the optical transitions then the six lines in a given polarization follow the Zeeman and diamagnetic shift of the exciton, as in a non-magnetic quantum dot. The parallel

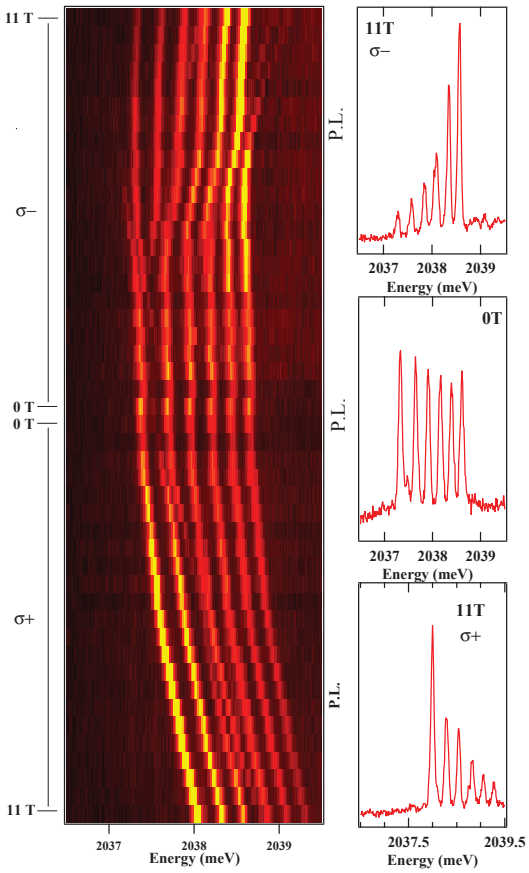

Figure 1.7: Magnetic field dependence of the emission of a Mn-doped quantum dot recorded in $\sigma+$ and $\sigma-$ polarisation. Anticrossing of the bright and dark states appears around 7T in $\sigma-$ polarisation. From reference (5)

evolution of the six lines is perturbed around 7T in $\sigma-$ polarization by anti-crossings observed for five of the lines. In addition, as the magnetic field increases, one line in each circular polarization increases in intensity and progressively dominates the others.

The electron-Mn part of the interaction Hamiltonian $j_e(S \cdot M)$ couples the dark $(J_z + S_z = \pm 2)$ and bright $(J_z + S_z = \pm 1)$ heavy hole exciton states. This coupling corresponds to a simultaneous electron and Mn spin flip changing a bright exciton into a dark exciton. In a first approximation, because of the strain induced splitting of light hole and heavy hole levels, a similar Mn-hole spin flip scattering is not allowed. The electron-Mn spin flip is enhanced as the corresponding levels of bright and dark excitons are brought into coincidence by the Zeeman effect. An anti-crossing is observed around 7T for five of the bright states in $\sigma-$ polarization (Figure 1.7). It induces a transfer of oscillator strength to the dark states. The lower energy state in $\sigma-$

polarization ($|+1/2\rangle_e|-3/2\rangle_h|+5/2\rangle_{Mn}$) does not present any anti-crossing. In this spin configuration, both the electron and the Mn atom have maximum spin projection and a spin flip is not possible.

The minimum energy splitting at the anti-crossing is directly related to the electron-Mn exchange integral J_e. For instance, the splitting measured for the higher energy line in $\sigma-$ polarisation (Figure 1.7), $\Delta E = 150\mu$eV gives $j_e \approx$-70μeV. From the overall splitting measured at zero field ($1.3meV$) and with this value of j_e, we obtain $j_h \approx$150μeV. These are typical values for the exchange integrals in CdTe magnetic quantum dots.

1.5 Summary

In this chapter, we introduced basis on spintronics, diluted magnetic semiconductor, and single spin based devices. We then discussed the basic properties of CdTe and CdTe base self-assembled quantum dots. We then introduced the optical properties of single Mn doped quantum dots. In the next chapter, we will give more experimental evidence on the optical pumping and the dynamics of an individual Mn spin in a quantum dots.

1. SPINTRONICS, DILUTED MAGNETIC SEMICONDUCTORS AND QUANTUM DOTS

2

Optical pumping of an individual Mn spin: Experiments and Rate equations

Contents

We will first present in this chapter a summary of some recent experiments showing that the spin state of a single magnetic atom embedded in an individual semiconductor quantum dot can be optically probed and controlled using micro-spectroscopy[1]. A high degree of spin polarization has been achieved for an individual Mn atom using quasi-resonant or fully-resonant optical excitation of the quantum dot at zero magnetic field. Under quasi-resonant excitation, optically created spin polarized carriers generate an energy splitting of the Mn spin and enable magnetic moment orientation controlled by the photon helicity and energy. Monitoring the time dependence of the intensity of the fluorescence during a resonant optical pumping process allows to directly probe the dynamics of the initialization

[1] most of the experimental data of this chapter comes from the reference (10) and (11), published by the author's group

of the Mn spin: the optical initialization can take place in less than 100ns. The Mn spin state prepared by optical pumping is fully conserved for a few microseconds. These experiments suggest a complex carriers-Mn spin dynamics we will describe in the following chapters. In the last part of this chapter, we give a simple rate equations model for the exciton-Mn system, with the phenomenological parameter and discuss the pumping of Mn spin by a resonant laser excitation.

2.1 Optical Mn spin orientation

To optically pump the Mn spin, Mn-doped quantum dots were quasi-resonantly excited with a tunable continuous wave (CW) dye laser. In order to record the dynamics of the preparation of the Mn spin (spin transients), the linear polarization of the excitation laser was modulated between two orthogonal states by switching an electro-optic modulator, and converted to circular polarization with a quarter-wave plate. Trains of resonant light with variable duration were generated from the CW laser using acousto-optical modulators with a switching time of 10 ns. The circularly polarized collected light was dispersed by a 1 m double monochrometer before being detected by a fast avalanche photodiode in conjunction with a time correlated photon counting unit.

Figure 2.1 and 2.2 summarize the main features of the time-resolved optical orientation experiment. The PL of the exciton-Mn (X-Mn) complex was excited about 20 meV above the PL (top of Figure 2.1(a)), on an excited state of the X-Mn complex (52); the PL intensity was detected in circular polarization (*e.g.*, σ^-, corresponding to the recombination of the -1 exciton). The relative intensities of the six lines dramatically depend on the excitation energy (bottom of Figure 2.1(a)): as each line corresponds to one value of the Mn spin projection M_z, the whole process creates a non-equilibrium occupation probability of the Mn spin states. Under these conditions, switching the circular polarization of the excitation produces a change of the σ^- PL intensity (Figure 2.1(b)) with two transients: first an abrupt one with the same sign for all six lines, reflecting the population change of the spin polarized excitons; then a slower transient reflecting an increase or a decrease of the occupation of the detected Mn spin state. This slow transient has an opposite sign for the two extreme PL lines (*i.e.*, when monitoring the Mn spin states $M_z = \pm 5/2$, Figure 2.2(b)), and a characteristic time which is inversely proportional to the pump intensity (Figure 2.2(a)). This is the signature of an optical pumping process which realizes a spin orientation of the Mn atom. We first discuss the details of this process, then use it to study the spin dynamics of the single Mn in the quantum dot.

The relevant sub-levels of X-Mn and Mn are schematized in Figure 2.2(c). For the sake of simplicity, we omit the dark exciton states which will be included for a quantitative analysis and consider that the dynamics can be described by two spin

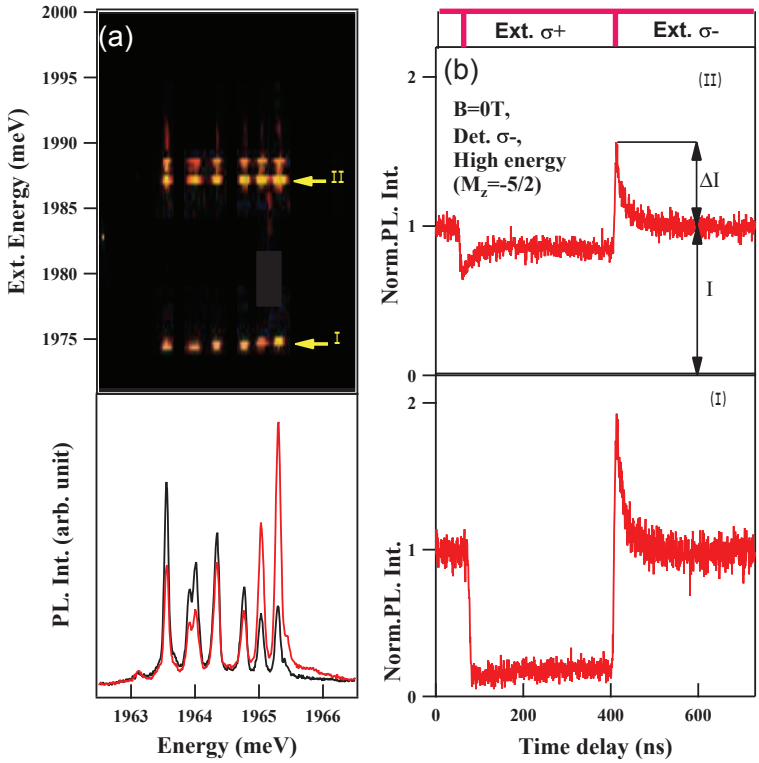

Figure 2.1: (a) PL and PLE of a Mn-doped quantum dot (quantum dot 1) at $B = 0$ T and $T = 5$ K. The PL is detected in circular polarization under an alternate σ^-/σ^+ excitation at two different wavelengths: 1987.0 meV (black) and 1987.4 meV (red). (b) PL transient under polarization switching at $B = 0$ T. The PL is detected on the high energy line of X-Mn in σ^- polarization (Mn spin $M_z = -5/2$). Transient (I) (resp. (II)) was observed under resonant excitation at 1975 meV (resp. 1987 meV). From reference (10)

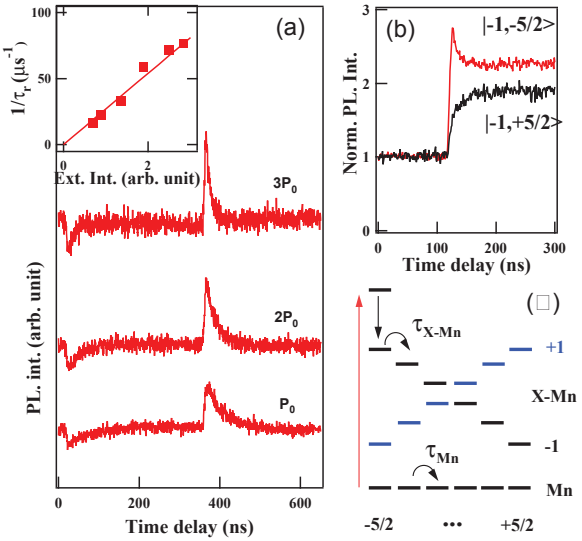

Figure 2.2: PL transients at different values of the excitation power. Inset: power dependence of the inverse response time τ_r, taken at the $1/e$ point of the spin-related transient. (b) PL transients recorded in σ^- polarization on the high (M_z=-5/2) and low (M_z=+5/2) energy line of the X-Mn complex. (c) Simplified level diagram of a Mn-doped quantum dot, as a function of Mn spin (X-Mn: bright exciton-Mn). From reference (10)

relaxation rates, one for the Mn alone $\Gamma_{Mn,G}$ and one within the X-Mn complex Γ_{X-Mn} (12, 53). As spin orientation results from a cumulative effect of relaxation in presence of the exciton, it can be performed only if Γ_{X-Mn} is faster than $\Gamma_{Mn,G}$. When exciting one of the low energy excited states of the quantum dot, two mechanisms are expected to contribute to the observed spin orientation: the selective excitation of the quantum dot can show a dependence on the Mn spin state (52), and the relaxation of the Mn spin within the X-Mn system is driven by the interaction with the spin polarized carriers which have been injected.

Under spin selective excitation, the spin relaxation of X-Mn tends to empty the spin state of the Mn which is most absorbant (12). Under injection of spin polarized carriers, relaxation processes tend to anti-align the Mn spin with the X exchange field to reach a thermal equilibrium on the X-Mn levels (12). Hence, optical pumping with σ^- photons for instance, tends to decrease the population of the spin state M_z=-5/2 and increase that of M_z=+5/2, as observed in Figure 2.2(b). Both mechanisms, absorption selectivity and spin injection, depend on the structure of the excited states, resulting in a pumping signal which depends on the excitation energy (Figure 2.1). An efficient pumping of the Mn spin can be performed within a few tens of ns, showing that at $B = 0$T the spin relaxation time of the Mn alone is long enough compared to the X-Mn

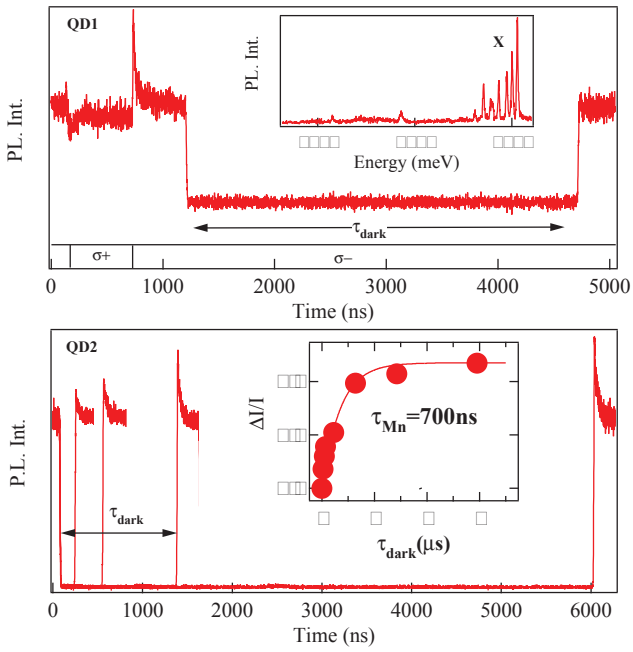

Figure 2.3: (a) PL transients recorded on quantum dot 1 (corresponding PL in the inset) under the optical polarization sequence displayed at the bottom of the plot. The spin distribution prepared by optical pumping is conserved during τ_{dark}=3.5μs. (b) PL transients recorded on quantum dot 2. The amplitude of the pumping signal is restored after $\tau_{dark}\sim$3μs. From the delay dependence of this amplitude we deduce a Mn relaxation time of $\sim$700ns.

dynamics.

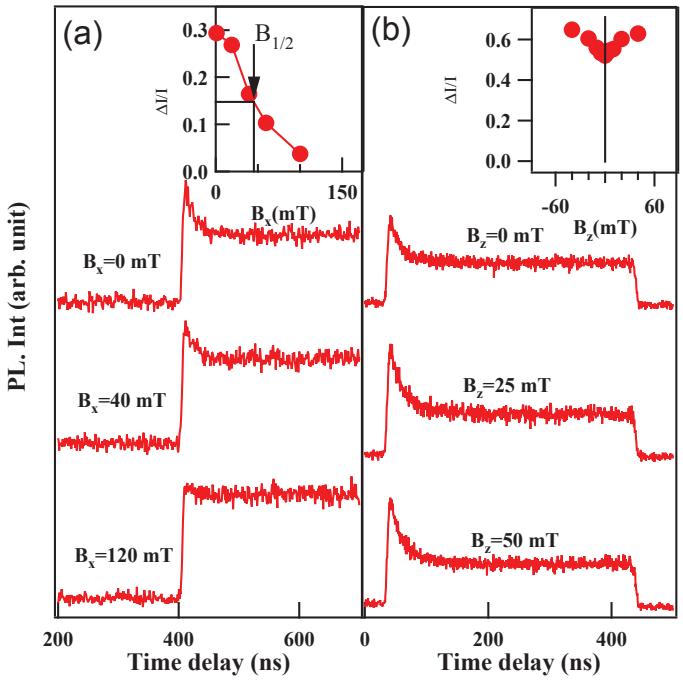

Figure 2.4: Mn spin transient as a function of a magnetic field applied in-plane (a) and out-of-plane (b). Inset: transverse field dependence of the transient amplitude $\Delta I/I$). $B_{1/2}$ is the half width at half maximum. From reference (10)

Having established a method to prepare the Mn spin, we will perform pump-probe experiments to observe how long the Mn polarization can be conserved (Figure 2.3). We prepare a non-equilibrium distribution of the Mn spin with a $\sigma^{\pm}$ pump pulse. The pump laser is then switched off, and switched on again after a dark time τ_{dark}. The amplitude of the pumping transient after τ_{dark} depends on the Mn spin relaxation in the dark. For quantum dot 1 (Figure 2.3(a)) no transients are observed after a dark time of 3.5μs. This demonstrates that in the absence of charges fluctuations (*i.e.* neutral quantum dot (see inset of Figure 2.3(a))) the prepared Mn spin is conserved over μs. For quantum dot 2 (Figure 2.3(b)) the amplitude of the pumping signal is restored after $\tau_{dark}\sim$3μs. From the delay dependence of this amplitude we deduce a Mn relaxation time of $\sim$700ns. These two examples show that the measured spin relaxation is not intrinsic to the Mn spin but depends on its local environment (strain, presence of carriers...).

More information on the Mn local environment can be obtained from the magnetic field dependence of the optical pumping signal. For an isotropic Mn spin, the deco-

herence of the precessing spin in a transverse field gives rise to the standard Hanle depolarization curve with a Lorentzian shape and a width proportional to $1/T_2$ (54).

In the present case, a magnetic field in the Faraday configuration (B_z) does not change significantly the PL transients (Figure 2.4(b)): a weak increase of the spin orientation efficiency is observed as soon as a field of a few mT is applied. By contrast, an in-plane field (B_x) induces a coherent precession of the Mn spin away from the optical axis (= quantum dots' growth axis), so that the average spin polarization, and therefore the amplitude of the optical pumping signal, decays (Figure 2.4(a)).

It is known from electron paramagnetic resonance spectroscopy that the ground state of Mn^{2+} presents a fine structure (55). In a cubic crystal, it results from a hyperfine coupling with the Mn nuclear spin, $A\vec{I}\cdot\vec{M}$ (with I=5/2 and A$\approx 0.7\mu$eV), and the crystal field. In addition, in epitaxial structures, built-in strains due to the lattice mismatch induce a magnetic anisotropy with an easy axis along the quantum dot's axis. It scales as $D_0 M_z^2$, with D_0 proportional to the biaxial strain (55).

This fine structure controls the Mn spin dynamics at zero or weak magnetic field. At zero field, in the absence of anisotropy, the precession of the electronic spin of the Mn in its own hyperfine field should erase any information stored on the electronic spin (56). In the presence of magnetic anisotropy, the precession of the Mn spin in the nuclear field is blocked even at $B = 0T$. The magnetic anisotropy also blocks the Mn spin precession in a weak transverse magnetic field. Then the tranverse field dependence of the optical pumping efficiency is controlled both by the anisotropy D_0 and the coherence time T_2.

2.2 Resonant optical pumping of a single Mn spin.

As proposed by Govorov *et al.* (12), the direct resonant excitation of one optical transition of the ground X-Mn complex can be used to perform a direct and more efficient optical pumping of the Mn spin. In this optical pumping process, a laser drives resonantly one of the exciton-Mn transition ($|-1, M_z = -5/2\rangle$ in Figure 2.5) with a Rabi frequency $\Omega = \mathcal{P}\mathcal{E}/\hbar$, $\mathcal{P}$ is the dipolar moment of the quantum dot transition and $\mathcal{E}$ the amplitude of the electric field of the resonant laser. A photon absorption occurs only if the Mn spin in the quantum dot is in the $M_z = -5/2$ spin state. The resultant exciton can radiatively recombine via the same channel, or a spin-flip process can project the X-Mn complex in a state with $M_z \neq -5/2$. After a few cycles of absorption-emission, the probability of detecting the Mn in the $M_z = -5/2$ state decreases. In this mechanism, we have assumed that the Mn spin was conserved once the exciton has recombined. The conservation of the Mn spin between the recombination of an exciton and the absorption of a photon can be altered in two ways: either by a relaxation process involving an exchange of energy or by a coherent evolution (10, 56).

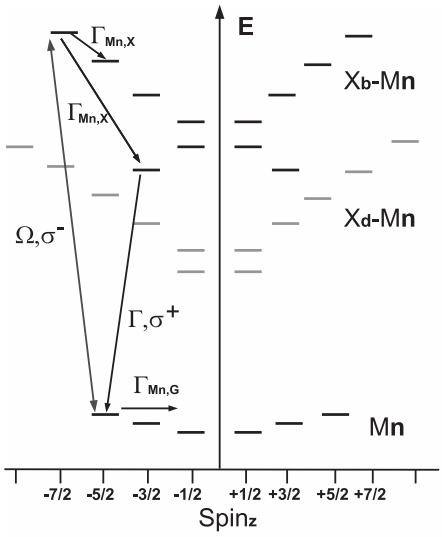

Figure 2.5: Energy levels of a Mn doped quantum dot involved in the optical pumping mechanism described in the text (Black: bright excitons (X_b)); grey: dark excitons (X_d)). The sates are displayed as a function of their total angular momentum M_z and energy E. For the resonant optical pumping, the quantum dot is resonantly driven on the state $M_z = -5/2$ with a $\sigma-$ laser pulse with a Rabi frequency Ω. The scattered photons obtained after a spin-flip of the exciton (rate $\Gamma_{X,Mn}$) are recorded in $\sigma+$ polarisation.

A coherent evolution can be neglected if the fine structure of the Mn atom is dominated by a magnetic anisotropy along the growth axis (10). Otherwise, processes such as the coherent evolution of the Mn spin in the hyperfine field of the Mn nucleus or in the tetragonal crystal field leads to a change of the Mn spin state between the injection of two excitons. In that case, no optical pumping can occur. In the following, we will use $\Gamma_{Mn,G}$ to describe the characteristic rate at which the Mn spin state changes due to coherent or incoherent processes, when the quantum dot is empty. This mechanism of Mn spin manipulation is similar to the pumping process used to prepare a single carrier spin in a quantum dot (57, 58). It involves an optically forbidden transition (*i.e.* spin flip of the Mn interacting with the exciton) and is based on the inequality $\Gamma_{Mn,X} > \Gamma_{Mn,G}$.

To demonstrate and test the efficiency of this optical pumping process, we developed a two wavelength pump-probe set-up allowing an optical initialization and read-out of the Mn spin (11). In this experiment, a resonant circularly polarized CW laser (*resonant pump*) tuned on a X-Mn level pumps the Mn spin. In the initial state at t=0, the Mn atom is in thermal equilibrium. The resonant creation of an exciton followed by a spin relaxation of the Mn in the exchange field of the exciton empties the spin-state under excitation. Then, a second laser train, linearly polarized and tuned on an excited state of the quantum dot (*quasi-resonant probe*), injects excitons independently of the Mn spin state M_z. A spin relaxation of the X-Mn complex under these conditions of excitation drives the Mn atom back to an equilibrium where all spin states are equally populated. Recording one of the six PL lines under this periodic sequence of excitation, we monitor the time evolution of the probability of occupation of a given Mn spin state.

The main features of this experiment are presented in Figure 2.6. In this example, $\sigma+$ PL signal is recorded on the low energy X-Mn line. The quantum dot is resonantly excited on the high energy state of the X-Mn complex with $\sigma-$ photons. This excitation can only create an exciton in the dot if the Mn spin state is M_z=-5/2. After this pumping sequence, the resonant pump laser is switched off and followed by a linearly polarized excitation on an excited state (*quasi-resonant probe*). The amplitude of this quasi-resonant PL depends on the population of M_z=-5/2 and, at the beginning of the probe pulse, is a probe of the resonant pumping efficiency reached at the end of the pump pulse.

This is illustrated in Figure 2.6(i) which presents the difference of the two PL signals produced by the probe when the resonant pump laser was OFF or ON in the pump-probe sequence presented underneath the curve 2.6(ii). The difference of the two PL signals reflects the population difference between a sequence with optical pumping and a sequence where $M_z = -5/2$ is evenly populated. The height of the difference signal at the beginning of the probe pulse, which reaches 75% gives a direct measurement of the efficiency of the spin optical pumping. The PL transients observed during the probe

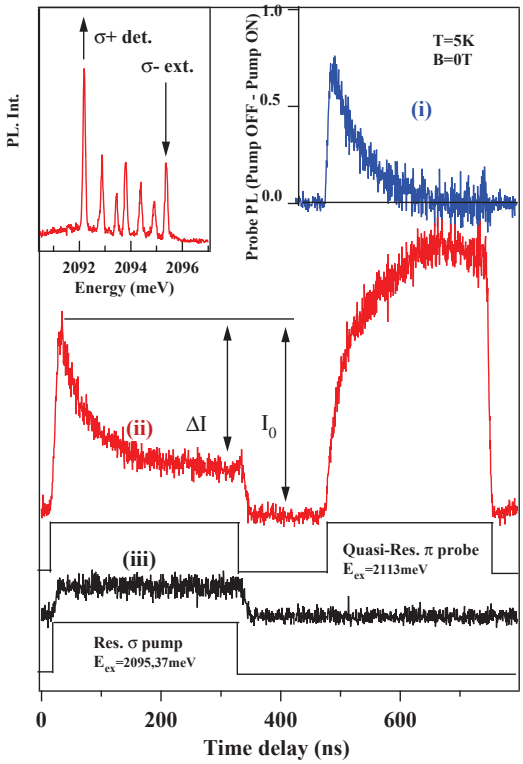

Figure 2.6: PL transients recorded on the low energy line of a Mn-doped quantum dot (quantum dot 1) under the quasi-resonant (quantum dot excited state: *probe*) and resonant (quantum dot ground state: *pump*) optical excitation sequence displayed at the bottom. The inset presents the quantum dot PL under non-resonant excitation and the configuration of the resonant excitation and detection. (i) Difference between the PL produced by the probe when the pump is OFF and when the pump is ON, (ii) PL from the pump and the probe and (iii) resonant PL produced by the pump alone. Because of the Mn spin memory in the absence of injected carriers, no signature of pumping is observed when the linearly non-resonant probe is OFF (iii). The optical pumping process is directly observed on the resonant fluorescence produced by the pump and latter on the PL from the probe laser. I_0 is the amplitude of the fluorescence at the beginning of the pump pulse and ΔI the amplitude of the transient. $\Delta I/I_0$ is the efficiency of the spin optical pumping.

pulse corresponds to the progressive destruction of the non-equilibrium distribution prepared by the pump. This reset process is produced by the injection of unpolarized excitons and its rapidity depends on the intensity of the probe laser.

A more direct way to probe the optical pumping process is to monitor the time evolution of the fluorescence signal observed during the resonant excitation. Excitation transfer can occur within the X-Mn complex during the lifetime of the exciton and gives rise to a weak PL on all the quantum dot's levels. Whatever the spin relaxation processes involved in this excitation transfer, this signal depends on the absorption of the pump laser which is controlled by the occupation of M_z=-5/2: it monitors the spin selective absorption of the quantum dot and is then a direct probe of the pumping efficiency of the Mn spin. The pumping efficiency is then given by $\Delta I/I_0 \approx 75\%$ (see Figure 2.6), in agreement with the pumping efficiency measured on the probe sequence.

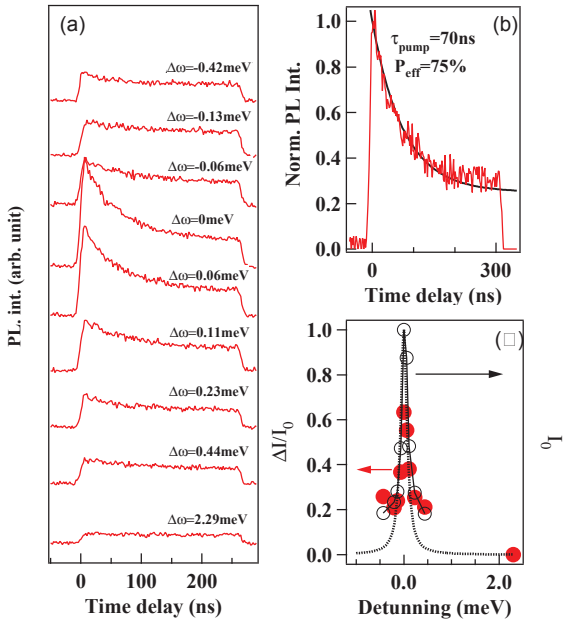

Figure 2.7: (a) Excitation energy dependence of the resonant fluorescence signal obtained on quantum dot 1 for cross circular excitation-detection on the high and low energy exciton line respectively (positive detuning corresponds to an excitation on the high energy side of the line). (b) Detail of the resonant fluorescence transient recorded during the optical pumping process. The exponential fit (black line) gives an optical pumping efficiency $P_{eff} \approx 75\%$ and a pump time of 70 ns. (c) Amplitude of the resonant fluorescence signal as the excitation is tuned around the high energy line of X-Mn. The Lorentzian fit give a full width at half maximum of $80\mu eV$.

The time evolution of the PL detected on the low energy state of X-Mn under a

resonant excitation on the high energy state is presented in Figure 2.6(ii) and 2.6(iii) for two different pump-probe sequences: probe ON and probe OFF respectively. When the probe laser is switched ON, an equilibrium distribution of the Mn spin is restored by the non-resonantly injected unpolarized excitons before each pumping pulse. The absorption, and then the amplitude of the resonant fluorescence signal is maximum at the beginning of the pump pulse and progressively decreases as the state M_z=-5/2 is emptied by the optical pumping process. When the probe laser is switched OFF in the pump-probe sequence, the resonant fluorescence transients during the pump pulse disappears and a weak constant PL is observed. This disappearance of the transient is a signature of the perfect conservation of the Mn spin distribution during the dark time between each pumping pulse. The steady state PL depends on the optical pumping efficiency which is controlled by the ratio of the relaxation rates for the Mn spin in the exchange field of the exciton and the relaxation and coherent evolution of the Mn spin in an empty dot (10, 56).

2.3 Time resolved resonant fluorescence of a Mn doped quantum dot.

The resonant fluorescence signal can be used to analyze the influence of the excitation power, wavelength and polarization on the efficiency of the Mn spin optical pumping (11). A detail of the time resolved resonant fluorescence signal obtained with the pump laser tuned strictly on resonance with the high energy level is presented in Figure 2.7(b). A decrease of about 75% of the resonant PL is observed during the optical pumping process with a characteristic time of τ_{pump}=70 ns. This exponential decay reflects the decrease of the absorption of the quantum dot induced by the decrease of the population of the state M_z=-5/2 and shows it takes a few tens of ns to initialize the Mn spin. Alternatively, one can say that the transition can be recycled for a few tens of ns before the laser induces a Mn spin-flip event. After a few tens of ns the PL reaches a steady state intensity.

Figure 2.7(a) and 2.7(b) present the amplitude and time evolution of the fluorescence signal detected on $|+1, M_z = -5/2\rangle$ for different *pump* wavelength around the high energy level $|-1, M_z = -5/2\rangle$. A clear resonant behavior is observed in the initial amplitude I_0 of the fluorescence signal (Figure 2.7(c)). This reflects the wavelength and excitation power dependence of the absorption of the quantum dot. The measured width of the resonance ($\sim 80\mu eV$) is a convolution of the width of the quantum dot's absorption in the non-linear regime and of the linewidth of the excitation laser ($\sim 60\mu eV$). The efficiency of the optical pumping $\Delta I/I_0$, presents a similar resonance demonstrating the strong excitation energy dependence of the spin optical pumping process.

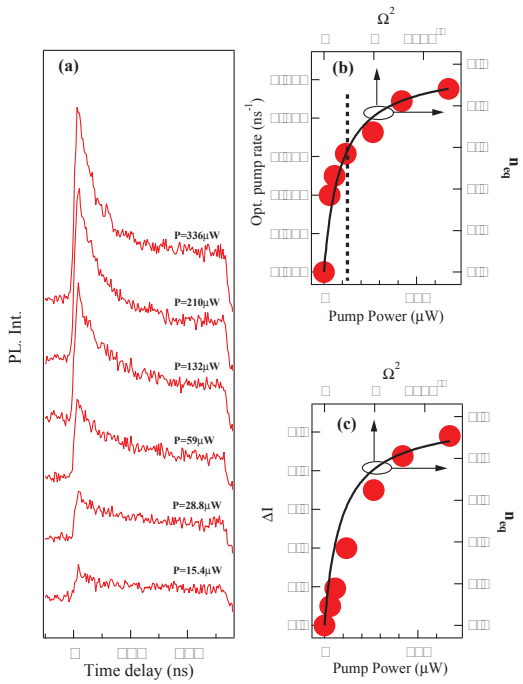

Figure 2.8: (a) Excitation power dependence of the resonant fluorescence signal of quantum dot 1. (b) Excitation power dependence of the optical pumping rate. The vertical dotted line shows the excitation power range used in the optical pumping wavelength dependence presented in Figure 3. (c) Excitation power dependence of the amplitude of the optical pumping signal. The solid lines in (b) and (c) represent the calculated evolution of the population of a resonantly excited two level system as a function of the square of the Rabi frequency which is proportional to excitation intensity. In this calculation, T_1=180ps, T_2=10ps and Ω^2 is adjusted to reproduce the observed saturation.

As displayed in Figure 2.8, the characteristic time and the amplitude of the optical pumping signal also depends on the excitation intensity. In the low excitation regime, as expected for a spin optical pumping process, the transient characteristic time (τ_{pump}) is inversely proportional to the pump laser intensity. A saturation behavior is clearly observed for the amplitude and the characteristic time of the resonant fluorescence transient. The saturation of the optical pumping process results from a saturation of the absorption of the resonantly excited excitonic level. Indeed, the population of a two level system driven by a resonant excitation laser is given by (59): $n_{eq} = \Omega^2(\frac{T_1}{T_2})/2(\Delta\omega^2 + \frac{1}{T_2^2} + \Omega^2\frac{T_1}{T_2})$, where Ω is the Rabi frequency, $\Delta\omega$ the detuning between the excitation laser and the excitonic transition, T_1 and T_2 the lifetime and the coherence time of the exciton respectively. The rate of the spin optical pumping process, which is proportional to n_{eq}, is expected to increase with the excitation Rabi frequency until it reaches a saturation value when the Rabi frequency is larger than the spontaneous emission rate ($\Omega \gg T_1^{-1}$). n_{eq} obtained with T_1=180ps, T_2=10ps (60) and $\Delta\omega$=0 is compared with the optical pumping signal in Figure 2.8(b) and 2.8(c). A good agreement with this simple model describing the population of a two level system resonantly excited by a CW laser is obtained.

In the saturation regime, if $M_z = -5/2$ the quantum dot is in the $|-1, M_z = -5/2\rangle$ state half of the time in average. Taking for granted that $\Gamma_{Mn,X} \gg \Gamma_{Mn,G}$, the rapidity of the optical pumping process is no longer controlled by the rate at which excitons are injected but depends only on the relaxation rate from the state $|-1, M_z = -5/2\rangle$ to other X-Mn levels with $M_z \neq -5/2$. Therefore, the pumping rate in the saturation regime gives an estimation of the spin-flip rate of the Mn in the exchange field of the exciton $\Gamma_{Mn,X}/2 \approx \Gamma_{pump}$ and a relaxation time $\tau_{Mn,X} \approx 20ns$ in agreement with the value deduced from photon correlation measurements (53).

2.4 Rate equations for X+Mn system

Here we provide a heuristic non-equilibrium model for the Mn spin dynamics driven by laser pumping. We propose a master equation for the occupation of the eigenstates of a simplified single Mn-doped Hamiltonian quantum dot that features the projection along the z axis of the spin 1/2 electron, the pseudo spin $J = 3/2, J_z = \pm 3/2$ of the heavy hole and the spin 5/2 of the Mn:

$$\mathcal{H} = j_h \hat{J}_z \hat{M}_z + j_{eh} \hat{S}_z \hat{J}_z + j_e \hat{S}_z \hat{M}_z + D_0 \hat{M}_z^2 \tag{2.1}$$

The first term corresponds to the hole Mn coupling, which is antiferromagnetic ($j_h > 0$). The second to the electron-hole exchange, which is ferromagnetic , so that the dark ± 2 excitons lie below the bright ± 1 exciton doublet. The third term is the electron-Mn exchange. The fourth term is the single ion anisotropy adequate for a

strained thin layer (61). The spin-flip contributions, which certainly present in the carrier-Mn coupling, have been studied in detail elsewhere (17). In first approximation, they can be neglected. A complete analysis of their effect will be discussed elsewere (13). Hamiltonian (2.1) commutes with M_z, S_z and J_z so that the eigenvalues are $E(M_z, S_z, J_z) = E_X + j_h J_z M_z + j_{eh} S_z J_z + j_e S_z M_z$ where $E_X \simeq 2eV$ is the bare exciton energy. To reproduce the experimental spectrum we take $j_e = -0.05meV$, $j_h = 0.2meV$ and $j_{eh} = -0.75meV$ (5). As shown in figure 1, this spectrum is made of 6 doublets for the bright exciton above the 6 doublets for the dark excitons. The ground state spectrum is given by $D_0 M_z^2$, with $D_0 = 0.007$meV (61).

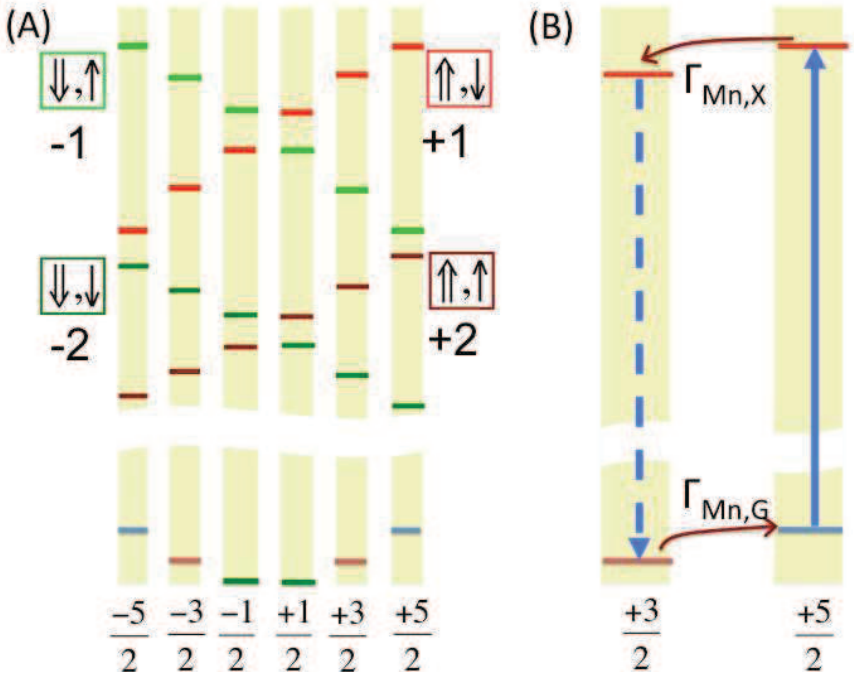

Figure 2.9: (A) Diagram of the 24 exciton-Mn levels and the 6 Mn levels involved in the optical pumping process. (B) Scheme of the optical pumping.

The master equation model that we use here is an extension of the simple model by Govorov and Kalameitsev (hereafter GK) (12) in their proposal of optical spin pumping of a single Mn in a quantum dot. In GK, a unique rate is assigned to transitions between the 24 exciton levels, complying with principle of detailed balance but neglecting the dependence of the rates on energy and spin change. Whereas a detailed microscopic model will be presented elsewhere (13), here we propose a model for the rates in which transitions are only permitted between states that are connected via the flip of a single spin (the one of either the Mn, the electron or the hole). This rule is certainly present in most of spin relaxation mechanisms and restricts significantly the relaxation pathways.

However, we still neglect the dependence of the rates on the energy difference, except for the fact that we use the principle of detailed balance. Thus, our model has 4 elementary rates Γ_e, Γ_h, $\Gamma_{Mn,X}$ and $\Gamma_{Mn,G}$ for the relaxation of the spin of the electron, hole, Mn in the presence of the exciton and Mn in the dark. In addition, M_z conserving transitions between the six ground states and the 12 bright exciton transitions are described with a laser pumping function $g(M_z, X)$ where $X = \pm 1, \pm 2$ labels the excitons. We take $g(M_z, X = \pm 2) = 0$. Mn spin conserving spontaneous emission from bright Γ_B and dark Γ_D are also included.

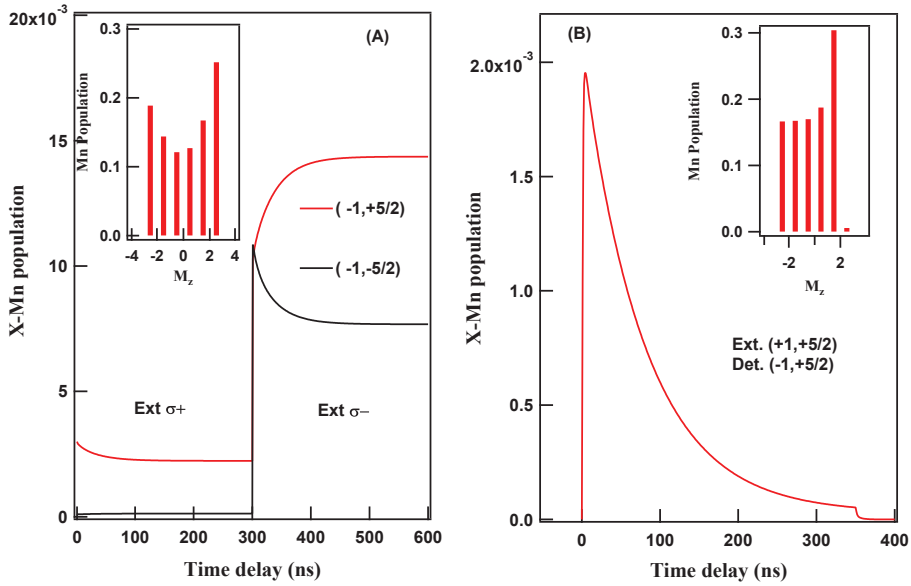

Figure 2.10: (A) Calculated photoluminescence transients obtained in $\sigma-$ polarization on the high (M_z=-5/2) and low (M_z=+5/2) energy line under alternate injection of $\sigma-$ and $\sigma+$ excitons. The inset shows the Mn spin population at the end of the $\sigma-$ pumping sequence. (B) Calculated photoluminescence of $|-1, +5/2\rangle$ under excitation on $|+1, +5/2\rangle$. As shown in the inset, the resonant laser excitation empty the state M_z=+5/2.

The master equation reads:

$$\frac{dp_N}{dt} = \sum_{N'} \Gamma_{N \leftarrow N'} p_{N'} - \sum_{N'} \Gamma_{N \leftarrow N'} p_{N'} \tag{2.2}$$

The model permits to consider three excitation modes: (i) resonant, for which $\Gamma(M_z, X)$ is non-zero for only one of the 12 bright excitons states, (ii) unpolarized and non-resonant (or quasi-resonant, using the jargon of the experimental paper (10)) for which $\Gamma(M_z, X)$ is non-zero for all the 12 bright states, and (iii) polarized non-resonant, for which $\Gamma(M_z, X)$ is non zero for the six states of a given bright exciton.

In Figure 2.10 we show the results of the simulation of the optical pumping processed

reported by Le Gall *et al.* (10). We take Γ_e=$\Gamma_h = 1ns^{-1}$, $\Gamma_B = 4ns^{-1}$, $\Gamma_D = 0.1ns^{-1}$, $\Gamma_{Mn,X} = 0.1ns^{-1}$ and $\Gamma_{Mn,G} = 0.0001ns^{-1}$. Γ_B, Γ_D and $\Gamma_{Mn,X}$ have been measured using time resolved and photon correlation measurements on single Mn doped quantum dots (9). A $\Gamma_{Mn,G}$ larger than a few micro-seconds has been deduced from recent optical pumping experiments (10). Γ_e=Γ_h=Γ_X in the ns range are typical values of spin relaxation for an exciton under magnetic field (62)(the exchange interaction with the Mn act on the exciton as an effective magnetic field of a few Teslas).

In the work of Le Gall (10) a quantum dot excited state level is pumped with circularly polarized light. This process has some degree of Mn spin selectivity which results in the depletion of the pumped Mn spin transition. The latter is traced by the time evolution of the PL intensity in the low energy peak which corresponds to the Mn spin $+5/2$ and $-5/2$ depending on the polarization of the detected photon. The main result observed experimentally is that the optically pumped Mn spin ground level is depleted. The solution of the master equation (2.2) with the restricted relaxation rules proposed here is able to account for the observed experimental optical pumping mechanism (Figure 2.10). As proposed by Govorov (63), this still can be understood within our model if the Mn spin relaxation is more efficient in the presence of the exciton than in the ground state ($\Gamma_{Mn,X} >> \Gamma_{Mn,G}$).

A more efficient pumping efficiency could be obtained under resonant excitation on the ground state of the quantum dot. Such process is illustrated in Figure 2.10. The high energy state $+5/2$ is resonantly driven by a $\sigma+$ laser. The initialization of the Mn spin is probed in the resonance fluorescence signal of the low energy state in $\sigma-$ polarization. The intensity of this signal probe the population of the state $+5/2$ and appears after a spin flip of the created exciton without any change in the Mn spin projection. With the same parameters used for the modelling of the non-resonant pumping experiment, we predict a pumping efficiency larger than 95% in a few tens of ns.

In summary, we have presented here preliminary simulations to account of Mn spin optical pumping using a model with realistic spin relaxation rules. The results are in good agreement with the reported experiments of optical orientation under quasi-resonant excitation reported in this chapter previously. The model suggest an efficient optical pumping in a tens of ns range for a resonantly driven Mn-doped quantum dot. This process suggest a very efficient exciton Mn spin relaxation. We will analyze these relaxation process in the following chapters.

2.5 Conclusion.

The results presented in this chapter demonstrate an efficient optical spin orientation of a single magnetic atom in a semiconductor host. Quasi-resonant or fully-resonant opti-

cal excitation of an individual Mn-doped quantum dot with circularly polarized photons can be used to prepare a non-equilibrium distribution of the Mn spin without any applied magnetic field. This distribution is fully conserved during a few microseconds. The spin-flip scattered photons can be used to probe the dynamics of the initialization of the Mn spin during the resonant optical pumping process.

These optical pumping experiments requires an efficient Mn spin relaxation in the presence of an exciton in the quantum dot which is in agreement with the simulation results of the heuristic model. They also suggest a strong influence of the Mn fine and hyperfine structure of the Mn on the pumping process. We will analyze in the following chapters some possible origin of this fast carrier-Mn spin dynamics in order to model these optical pumping experiments. We will also propose and model experiments to probe the fine and hyperfine structure of the Mn spin and its influence on the coherent dynamics of the Mn spin.

3

Quantum dot model

Contents

In the first part of this chapter, we first derive the Hamiltonian for the hole-Mn coupling, starting from Kohn-Luttinger Hamiltonian and Bir-Pikus Hamiltonian in a hard wall potential quantum dot. Then we give the Hamiltonian for the exciton-Mn system and discuss the influence of the Heisenberg term of hole-Mn coupling using a pseudo spin approach for holes. In the second part of this chapter, we introduce a spin-effective Hamiltonian for Mn-exciton complex to study the influence of the coupling between electronic and nuclear spins of the Mn on the spectra of a neutral quantum dot. We will then present an model the emission of quantum dots containing two Mn atoms.

3.1 Exciton-Mn Hamiltonian

In this section we describe a minimal quantum dot model and Hamiltonian that can accounts for the PL spectra of single Mn doped CdTe quantum dots. We will use it as a starting point of the modeling of the spin dynamics. For that matter we need to consider both the Mn spin in the unexcited crystal and the Mn spin interacting with a quantum dot exciton. The peaks in the PL spectra are associated to the energy differences between the states of the dot with and without the exciton.

3.1.1 Mn spin Hamiltonian

As we have seen, the Mn is a substitutional impurity in the Cd site of CdTe. Thus, it has an oxidation state of 2+, so that the 5 d electrons have spin $S = \frac{5}{2}$, resulting in a sextuplet(27) whose degeneracy is lifted by the interplay of spin orbit and the crystal field. In an unstrained CdTe, the crystal field has cubic symmetry which should result in a magnetic anisotropy Hamiltonian without quadratic terms. Electron paramagnetic resonance (EPR) in CdTe strained epilayers(61) show that Mn has a dominant uniaxial term in the spin Hamiltonian. In a quantum dot there could be some in-plane anisotropy as well, which lead us to consider the following minimal Hamiltonian:

$$\mathcal{H}_0 = \sum_{ij} D_{ij} M_i M_j + g\mu_B \vec{B} \cdot \vec{M} \tag{3.1}$$

where M_i are the $S = \frac{5}{2}$ spin operators of the electronic spin of the Mn. D_{ij} is a diagonal matrix with $D_{xx} = E$, $D_{yy} = -E$, and $D_{zz} = D_0$. Notice that D_{ij} describes the magnetic anisotropy that comes from the spin-orbit interaction of the electrons in the d orbits and the effect of neighbour atoms (crystal field) which split the 5 d levels into a doublet (e) and a triplet (d) (shown in Figure 1.3). The crystal field surrounding the magnetic atom interacts with the orbital momentum of the ion and then in turn interacts with the spin via spin-orbit coupling. So, we can write D_{ij} as a function of the Mn-Te distances $D_{ij}(R_{Mn} - R_{Te})$, and $R_{Mn} - R_{Te} = a_0 + u_{Mn} - u_{Te}$, where a_0 is the equilibrium distance determined by the lattice, u_{Mn} and u_{Te} are the displacements introduced by the strain or phonon. These displacements caused by phonon can introduce a spin relaxation which we will discuss in chapter 4.

The eigenstates of the Hamiltonian (Equation 3.1) are denoted by ϕ_m

$$\mathcal{H}_0|\phi_m\rangle = E_m|\phi_m\rangle = E_m \sum_{M_z} \phi_m(M_z)|M_z\rangle \tag{3.2}$$

where $|M_z\rangle$ are the eigenstates of M_z. In this section we neglect the hyperfine coupling to the $I = \frac{5}{2}$ nuclear spin and the tetragonal term of the fine structure splitting, which could affect the decay of the electronic spin coherence (10). Their effect will be discussed

in detail in chapter 6 where the coherent dynamics of the Mn is analyzed. The magnetic anisotropy parameters, E and D_0 can not be easily inferred from PL experiments, which are only sensitive to the Mn-exciton coupling. EPR experiments(61) in strained layer could be fit with $D_0 = 12\mu$eV, $E = 0$ and $g = 2.0$. Thus, the ground state should have $M_z = \pm\frac{1}{2}$, split from the first excited state by $2D_0$. At 4 Kelvin and zero magnetic field, we expect all the six spin levels to be almost equally populated. We refer to these six states as the ground state manifold, in contrast to the excited state manifold, which we describe with 24 states corresponding to 4 possible quantum dot exciton states and the 6 Mn spin states.

3.1.2 Single particle states of the quantum dot

We describe the confined states of the quantum dot with a simple effective mass model. In the case of the conduction band electrons, we neglect spin orbit coupling and we only consider the lowest energy orbital, with wave function $\psi_0(\vec{r})$, which can accommodate 1 electron with two spin orientations.

In the case of holes, spin orbit coupling lifts the sixfold degeneracy of the top of the valence band into a $J = \frac{3}{2}$ quartet and a $J = \frac{1}{2}$ doublet which, in CdTe, is more than 0.8eV below in energy. Confinement and strain lift the fourfold degeneracy of the $J = \frac{3}{2}$ hole states, giving rise to a mostly $J_z = \pm\frac{3}{2}$ heavy hole doublet and a almost $J_z = \pm\frac{1}{2}$ light hole doublet. Importantly, it is crucial to include LH-HH mixing to describe the experimental observation.

3.1.2.1 Effect of confinement

The top of the valence band states are described in the kp approximation with the so called Kohn-Luttinger Hamiltonian (64, 65, 66). For that matter, the crystal Hamiltonian is represented in the basis of the 4 topmost $J = \frac{3}{2}$ valence states of the Γ point. We label them by $J = \frac{3}{2}, J_z$. The resulting kp Hamiltonian can be written as $\mathcal{H}_{\text{holes}} = \mathcal{H}_{\text{KL}}$

$$\mathcal{H}_{\text{KL}} = \sum_{i,j=x,y,z} V_{ij}^{\text{KL}}(\vec{k}) J_i J_j + \kappa\mu_B J_z B \tag{3.3}$$

where $\vec{k}$ is the Bloch wave vector, J_i are the spin $\frac{3}{2}$ matrices, and V_{ij}^{KL} are coefficients given in the appendix A which are quadratic in the components of $\vec{k}$. The last term accounts for the Zeeman coupling to an external field along the growth direction.

The kp Hamiltonian for states in the presence of a quantum dot confinement potential that breaks translational invariance reads, for zero applied field:

$$\mathcal{H}_{\text{kp}} = -\hbar^2 \sum_{i,j=x,y,z} V_{ij}^{\text{KL}}(\partial_a \partial_b) J_i J_j + V(\vec{r})\delta_{j_z,j_z'} \tag{3.4}$$

where the matrix elements of $V_{ij}^{\mathrm{KL}}(\partial_a\partial_b)$ are a second order differential operators and $a,b = x,y,z$. In general, the numerical solution of equation (3.4) can be very complicated. Following previous work(17, 67), we make two approximations that permit to obtain analytical solutions. First, we model the quantum dot with a hard-wall box-shape potential. The dimensions of the box are L_x, L_y and L_z. This permits to write the wave function as a linear combination of $|J=\frac{3}{2},J_z\rangle$ states multiplied by the confined waves

$$\psi_{\vec{n}}(\vec{r}) = \sqrt{\frac{8}{V}} Sin\left(\frac{n_x\pi x}{L_x}\right) Sin\left(\frac{n_y\pi y}{L_y}\right) Sin\left(\frac{n_z\pi z}{L_z}\right) \tag{3.5}$$

Our second approximation is to restrict the basis set to the fundamental mode only, $n_x = n_y = n_z = 1$. As a result, the quantum dot Hamiltonian reads

$$\mathcal{H}_{\mathrm{kp}} = -\hbar^2 \sum_{i,j=x,y,z} V_{ij}^{\mathrm{KL}}(\langle\partial_a\partial_b\rangle) J_i J_j \tag{3.6}$$

where

$$\langle\partial_a\partial_b\rangle = \int \psi_{1,1,1}(\vec{r})\partial_a\partial_b\psi_{1,1,1}(\vec{r}) = \delta_{ab}\left(\frac{2\pi}{L_a}\right)^2 \tag{3.7}$$

Thus, within this approximation, the quantum dot hole states are described by a 4*4 Kohn Luttinger Hamiltonian where the terms linear in k_i vanish and the k_i^2 terms are replaced by $\left(\frac{2\pi}{L_i}\right)^2$. The resulting matrix $\mathcal{H}_{\mathrm{conf}}$ has two decoupled sectors denoted by $+$ ($J_z=+\frac{3}{2}$,$J_z=-\frac{1}{2}$) and $-$ ($J_z=-\frac{3}{2}$,$J_z=+\frac{1}{2}$). In the $(+\frac{3}{2},-\frac{1}{2},+\frac{1}{2},-\frac{3}{2})$ basis we have:

$$\mathcal{H}_{\mathrm{conf}} = \begin{pmatrix} \mathcal{H}_+ & 0 \\ 0 & \mathcal{H}_- \end{pmatrix} \tag{3.8}$$

with

$$\mathcal{H}_+ = \begin{pmatrix} \overline{P}+\overline{Q}-\frac{3b}{2} & \overline{R} \\ \overline{R} & \overline{P}-\overline{Q}+\frac{b}{2} \end{pmatrix} \tag{3.9}$$

and

$$\mathcal{H}_- = \begin{pmatrix} \overline{P}-\overline{Q}-\frac{b}{2} & \overline{R} \\ \overline{R} & \overline{P}+\overline{Q}+\frac{3b}{2} \end{pmatrix} \tag{3.10}$$

where $b \equiv \kappa\nu_B B$ and $\overline{P}$, $\overline{Q}$ and $\overline{R}$ are given in the appendix A. In order to find the corresponding energies and wavefunctions it is convenient to write these matrices as: $\mathcal{H}_\pm = a_\pm + \vec{h}_\pm\cdot\vec{\sigma}$ where $\vec{\sigma}$ are the Pauli matrices acting on the pseudo spin $\frac{1}{2}$ space of the $+$ and $-$ spaces, $a_\pm = P \mp b/2$ and

$$\vec{h}_\pm = \left(\overline{R}, 0, \overline{Q} \mp b\right) = |\vec{h}_\pm|\left(Sin\theta_\pm, 0, Cos\theta_\pm\right) \tag{3.11}$$

We keep only the two ground states (heavy-hole like), denoted by $|\Uparrow\rangle$ and $|\Downarrow\rangle$, which are several meV away from the light-hole like states. The ground state doublet for the quantum dot holes states so obtained, neglecting strain, can be written as

$$\begin{aligned} |\Uparrow\rangle &= cos\frac{\theta_+}{2}|+\frac{3}{2}\rangle + sin\frac{\theta_+}{2}|-\frac{1}{2}\rangle \\ |\Downarrow\rangle &= cos\frac{\theta_-}{2}|+\frac{-3}{2}\rangle + sin\frac{\theta_-}{2}|+\frac{1}{2}\rangle \end{aligned} \tag{3.12}$$

Thus, the LH-HH mixing parameters, $\theta_\pm$ depend on the dot dimension, L_i, on the Kohn Luttinger parameters, γ_i and on the applied magnetic field B.

In most cases the elimination of the 2 higher energy eigenstates of the hole Hamiltonian is a good approximation. Let us consider the single-hole states in eq. (3.12) at finite field and expand them in terms of the zero field ($b = 0$, $\theta_+ = \theta_-$) basis. It is apparent that the effect of the magnetic field is to mix the low and high energy sectors (as defined at zero field). In addition, this mixing is different for the two sectors denoted by $\pm$. As we show in the next chapter, hole-spin relaxation is possible at finite magnetic field exactly because of this channel dependent mixing. At zero magnetic field exchange coupling of the hole to Mn and electrons has the same effect, but, by keeping only the low energy states (3.12) in the zero field basis, the effect is not captured.

3.1.2.2 Effect of homogeneous strain

We now consider the effect of the strain that arises from the lattice mismatch between the CdTe quantum dot and the ZnTe substrate on the $J = \frac{3}{2}$ states of the valence band. It has a similar effect than the confinement, resulting in a splitting of the $J = \frac{3}{2}$ manifold and a mixing of the LH and HH states. The Hamiltonian that describes the effect of strain, as described by the strain tensor ϵ_{ij}, on the top of the valence band states in zinc-blende semiconductors was proposed by Bir and Pikus (for details, see appendix B). We can write the Bir-Pikus Hamiltonian as (68) :

$$\begin{aligned} \mathcal{H}_{\mathrm{BP}} &= \left(a - \frac{3b}{4}\right)(e_{xx} + e_{yy} + e_{zz}) + \\ &+ b \sum_{i=x,y,z} J_i^2 e_{ii} + \frac{d}{\sqrt{3}}\left(\left(J_x J_y + J_y J_x\right) e_{xy} + \text{c.p.}\right) \end{aligned} \tag{3.13}$$

where c.p. stands for cyclic permutation, and $a = -0.91$eV, $b = -1.2$eV, $d = -5.4$eV for CdTe(68).

For CdTe quantum dots grown in ZnTe, we mainly consider the effects of strain anisotropy in the growth plane(69) and describe the strain by the average values of e_{xy} and $e_{xx} - e_{yy}$. In this approximation the Bir-Pikus Hamiltonian is reduced to a block

diagonal matrix in the $(+\frac{3}{2}, -\frac{1}{2}, +\frac{1}{2}, -\frac{3}{2})$ basis:

$$\mathcal{H}_{BP} = \begin{pmatrix} \mathcal{H}_{BP+} & 0 \\ 0 & \mathcal{H}_{BP-} \end{pmatrix} \tag{3.14}$$

where

$$\mathcal{H}_{BP+} = \begin{pmatrix} 0 & \rho_s e^{-2i\varphi_s} \\ \rho_s e^{2i\varphi_s} & \Delta_{lh-hh} \end{pmatrix} \tag{3.15}$$

$$\mathcal{H}_{BP-} = \begin{pmatrix} \Delta_{lh-hh} & \rho_s e^{-2i\varphi_s} \\ \rho_s e^{2i\varphi_s} & 0 \end{pmatrix} \tag{3.16}$$

where $\Delta_{lh-hh} = b(e_{xx} + e_{yy})$ is the strain-induced HH-LH splitting, ρ_s is the strained induced amplitude of the HH-LH mixing and ϕ_s the angle between the strained induced anisotropy axis in the quantum dot plane and the x (100) axis and they are defined by:

$$\rho_s e^{-2i\varphi_s} = \frac{\sqrt{3}}{2} b \left(e_{xx} - e_{yy}\right) - i d e_{xy} \tag{3.17}$$

Importantly, the effect of confinement and the effect of strain have a very similar mathematical structure. They both split and mix the LH and HH levels. The main difference lies in the mixing term, which is real for the confinement Hamiltonian controlled by the shape of the quantum dot and in general complex for the Bir-Pikus Hamiltonian depending on the strain distribution in the quantum dot plane.

3.1.2.3 Combined effect of confinement and strain

We finally consider the combined action of confinement and strain described by $\mathcal{H}_{\text{holes}} = \mathcal{H}_{\text{conf}} + \mathcal{H}_{BP}$. Summing the Hamiltonians of equations (3.8) and (B.6) to obtain two decoupled matrices for the + and − subspaces. They can be written as

$$\mathcal{H}_{\text{tot},\pm} = A_{\pm} + \vec{H}_{\pm} \cdot \vec{\sigma} \tag{3.18}$$

where $A_{\pm} = \overline{P} \mp \frac{b}{2} + \frac{\Delta_{lh-hh}}{2}$ and

$$\vec{H}_{\pm} = \left(\overline{R} + \rho_s cos(2\varphi_s), \pm\rho_s sin(2\varphi_s), \overline{Q} \mp b - \frac{\Delta_{lh-hh}}{2}\right) \tag{3.19}$$

It is convenient to express the ground state doublet associated to $\mathcal{H}_{\text{holes}}$ in terms of the spherical coordinates of the vectors $\vec{H}_{\pm}$, $|\vec{H}_{\pm}|$, $\theta_{\pm}$ and $\phi_{\pm}$:

$$\begin{aligned} |\Uparrow\rangle &= Cos\frac{\theta_+}{2}|\frac{+3}{2}\rangle - Sin\frac{\theta_+}{2}e^{i\phi_+}|\frac{-1}{2}\rangle \\ |\Downarrow\rangle &= Cos\frac{\theta_-}{2}|\frac{-3}{2}\rangle - Sin\frac{\theta_-}{2}e^{i\phi_-}|\frac{+1}{2}\rangle \end{aligned} \tag{3.20}$$

where

$$e^{i\phi_{\pm}} = \frac{\overline{R} + \rho_s e^{\pm 2i\varphi_s}}{|\overline{R} + \rho_s e^{\pm 2i\varphi_s}|} \tag{3.21}$$

Expectedly, this expression is formally very similar to that of equation (3.12).

Formally, we express eq. (3.20) as

$$|\sigma_h\rangle = \sum_{j_z} C_h(j_z)|j_z\rangle \tag{3.22}$$

Both in equations (3.12) and (3.20) the $(+\frac{3}{2}, -\frac{1}{2})$ sector is decoupled from the $(-\frac{3}{2}, +\frac{1}{2})$. Whereas, this is not true in general, it is sufficient to account for the correct symmetry of a variety of exchange couplings between the hole spin and both the Mn and the electron spins.

3.1.3 Effective Mn-carrier exchange Hamiltonian

3.1.3.1 Hole-Mn Hamiltonian

We now consider the exchange coupling of hole spin ($\vec{J}$) and the Mn spin ($\vec{M}$). The leading term in the exchange interaction is the Heisenberg operator(27, 70):

$$\mathcal{V}_{\text{exch}} = \frac{1}{3}\beta\delta(\vec{r}_h - \vec{r}_M)\vec{J}\cdot\vec{M} \tag{3.23}$$

where β is the hole-Mn exchange coupling constant. For Mn in CdTe we have βN_0 =0.88 eV, where N_0 is the volume of the CdTe unit cell(27). The exchange interaction is taken as short ranged, the Mn atom is located at $\vec{r}_{Mn}$ and $\vec{J}$ are the spin $\frac{3}{2}$ angular momentum matrices. We represent the operator (3.23) in the product basis $|M\rangle \times \sigma_h$. Thus, the exchange operator in the product basis reads:

$$\langle M|\langle\sigma_h|\mathcal{V}_{\text{exch}}|M'\rangle|\sigma_h'\rangle = \beta|\psi_0(\vec{r}_{Mn})|^2 \sum_a \langle M|M_a|M'\rangle|\langle\sigma_h|J_a|\sigma_h'\rangle \tag{3.24}$$

where $\psi_0(\vec{r})$ is the envelope part of the heavy hole wave function, eq. (3.5), and $j_h \equiv \frac{1}{3}\beta|\psi_0(\vec{r}_{Mn})|^2$ is the hole-Mn coupling constant, which depends both on a material dependent constant β and on a quantum dot dependent property, the probability of finding the hole at the Mn location.

Now we define the two by two matrix:

$$V_i(h,h') = \langle\sigma_h|J_i|\sigma_h'\rangle = \sum_{j_z,j_z'} C_h(j_z)^* C_{h'}(j_z')\langle j_z|J_i|j_z'\rangle \tag{3.25}$$

where $C_h(j_z)$ and $C_{h'}(j_z')$ are cofficients of hole wave function considering the effect of confinement in equation 3.12. Importantly, since every 2 by 2 matrix can be written as a linear combination of the unit matrix and the Pauli matrices we shall have:

$$V_i = a_i 1 + \vec{b}_i\cdot\vec{\sigma}_h \tag{3.26}$$

after some algebra (see detailed calculation in Appendix D), we get:

$$V_z = a_z 1 + b_z \sigma_z \tag{3.27}$$

with

$$a_z = \frac{1}{2}\left[\frac{3}{2}\left(Cos^2(\theta_+/2) - Cos^2(\theta_+/2)\right) - \frac{1}{2}\left(Sin^2(\theta_+/2) - Sin^2(\theta_-/2)\right)\right] \tag{3.28}$$

and

$$b_z = \frac{1}{2}\left[\frac{3}{2}\left(Cos^2(\theta_+/2) + Cos^2(\theta_-/2)\right) - \frac{1}{2}\left(Sin^2(\theta_+/2) + Sin^2(\theta_-/2)\right)\right] \tag{3.29}$$

At zero field we have $\theta_+ = \theta_-$ so that $a_z = 0$ and

$$b_z(b=0) = \frac{1}{2}\left[3Cos^2(\theta/2) - Sin^2(\theta/2)\right] = 2Cos^2(\theta/2) - \frac{1}{2} \tag{3.30}$$

If there is no LH-HH mixing then $b_z = \frac{3}{2}$, $V_x = V_y = 0$ and the effective spin exchange Hamiltonian would read:

$$V_{\text{Ising}} = \frac{3}{2} j_h \sigma_z M_z \tag{3.31}$$

with

$$j_h \equiv \frac{\beta}{3}|\psi_0(\vec{r}_{Mn})|^2 \tag{3.32}$$

and

$$\sigma_z = \begin{pmatrix} 1 & 0 \\ 0 & -1 \end{pmatrix} \tag{3.33}$$

similarly to V^z, we can also get V^+ and V^-:

$$V^+(h,h') = \begin{pmatrix} 0 & \sqrt{3}Sin\left(\frac{\theta_+ + \theta_-}{2}\right) \\ 2Sin(\theta_+/2)Sin(\theta_-/2) & 0 \end{pmatrix} \tag{3.34}$$

If $b = 0$ we have $\theta_+ = \theta_- \equiv \theta$ and

$$V^+(h,h') = \begin{pmatrix} 0 & \sqrt{3}Sin\theta \\ 1 - Cos(\theta) & 0 \end{pmatrix} = \frac{\sqrt{3}}{2} Sin\theta \sigma^+ + \frac{1 - Cos(\theta)}{2}\sigma^- \tag{3.35}$$

In the small θ limit we have:

$$V^+(h,h') \simeq \theta \begin{pmatrix} 0 & \sqrt{3} \\ \frac{\theta}{2} & 0 \end{pmatrix} \tag{3.36}$$

Notice how the spin-flip Mn-hole coupling vanishes if there is no LH-HH mixing.

$$V^-(h,h') = \begin{pmatrix} 0 & 2Sin(\theta_+/2)Sin(\theta_-/2) \\ \sqrt{3}Sin\left(\frac{\theta_+ + \theta_-}{2}\right) & 0 \end{pmatrix} \tag{3.37}$$

If $b = 0$ we have $\theta_+ = \theta_- \equiv \theta$ and

$$V^-(h,h') = \begin{pmatrix} 0 & 1 - Cos(\theta) \\ \sqrt{3}Sin\theta & 0 \end{pmatrix} = \frac{\sqrt{3}}{2}Sin\theta\sigma^- + \frac{1 - Cos(\theta)}{2}\sigma^+ \tag{3.38}$$

In summary, the effective Mn-hole coupling spin model working in the space (M, σ_h) of dimension 12 reads:

$$\begin{aligned} \mathcal{V}_{h-Mn} &= j_h[\sigma_z M_z(2Cos^2(\theta/2) - \frac{1}{2}) + \frac{\sqrt{3}}{4}Sin\theta\left(\sigma^+M^- + \sigma^-M^+\right) \\ &+ \frac{1 - Cos\theta}{4}\left(\sigma^+M^+ + \sigma^-M^-\right)] \end{aligned} \tag{3.39}$$

If we define

$$j_z(\theta) = j_h(2Cos^2(\theta/2) - \frac{1}{2}) \tag{3.40}$$

$$\epsilon_1(\theta) = \frac{\frac{\sqrt{3}}{2}Sin\theta}{2Cos^2(\theta/2) - \frac{1}{2}} \tag{3.41}$$

and

$$\epsilon_2(\theta) = \frac{\frac{1-Cos\theta}{2}}{2Cos^2(\theta/2) - \frac{1}{2}} \tag{3.42}$$

we can write the exchange coupling as:

$$\mathcal{V}_{h-Mn} = j_z(\theta)\left[\sigma_z M_z + \frac{\epsilon_1}{2}\left(\sigma^+M^- + \sigma^-M^+\right) + \frac{\epsilon_2}{2}\left(\sigma^+M^+ + \sigma^-M^-\right)\right] \tag{3.43}$$

The functions $j_z(\theta)$, $\epsilon_1(\theta)$ and $\epsilon_2(\theta)$ are shown in the Figure 3.1. For $\theta = 0.6$ the LH-HH mixing is 9 percent ($Sin(0.6/2)^2 = 0.08$ and we have $\epsilon_1(0.6) = 0.37$ and $\epsilon_2(0.6) = 0.06$). For moderate mixing it is a good approximation to neglect ϵ_2.

We now write the model using the cartesian operators, rather than the ladder operators. The first term is the dominant Ising coupling, the second term is the standard or conserving spin-flip Mn hole coupling that couples states M, σ_h to $M \pm 1, \sigma_h \mp 1$:

$$\frac{1}{2}\left(\sigma^+M^- + \sigma^-M^+\right) = M_x\sigma_x + M_y\sigma_y \tag{3.44}$$

The third term is the anomalous or non-conserving spin flip term, which couples M, σ_h to $M \pm 1, \sigma_h \pm 1$. In cartesian coordinates it reads:

$$\frac{1}{2}\left(\sigma^+M^+ + \sigma^-M^-\right) = M_x\sigma_x - M_y\sigma_y \tag{3.45}$$

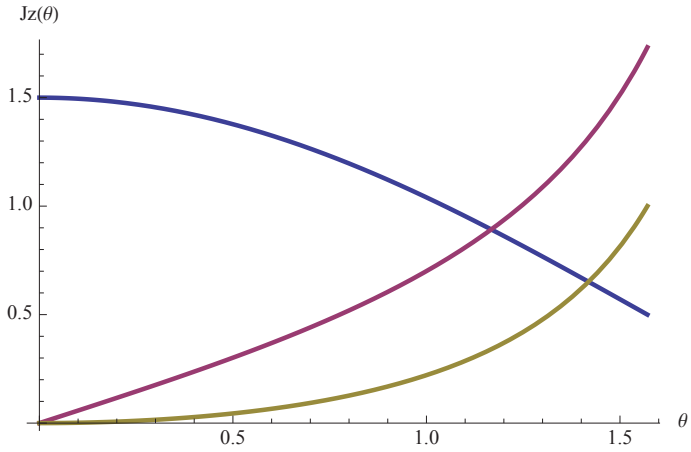

Figure 3.1: Functions $j_z(\theta)$ (blue), ϵ_1 (magnenta) and ϵ_2 (green) defined in the text.

As a result, the effective spin exchange is different for the x, y and z coordinates:

$$\mathcal{V}_{h-Mn} = j_{hx} M_x \sigma_x + j_{hy} M_y \sigma_y + j_{hz} M_z \sigma_z \tag{3.46}$$

where

$$\begin{aligned} j_{hx} &= j_h \left(\frac{\sqrt{3}}{2} Sin\theta + \frac{1 - Cos\theta}{2} \right) \\ j_{hy} &= j_h \left(\frac{\sqrt{3}}{2} Sin\theta - \frac{1 - Cos\theta}{2} \right) \\ j_{hz} &= j_h (2Cos^2(\theta/2) - \frac{1}{2}) \end{aligned} \tag{3.47}$$

Thus, the Mn-hole coupling is a so called XYZ model. Notice that for $\theta = 0$ there is no LH-HH mixing and we have $j_{hx} = j_{hy} = 0$ and $j_{hz} = \frac{3}{2} j_h$. In this extreme case the Mn-hole coupling is Ising like and M_z and σ_z are conserved. This limit is a good starting point to model hole-Mn coupling in CdTe quantum dots(17, 71)

Now we expand this expression for the relevant case of small LH-HH mixing, ie, small θ:

$$\mathcal{V}_{h-Mn} = j_h \left[\sigma_z M_z (\frac{3}{2} - \frac{\theta^2}{2}) + \frac{\sqrt{3}}{2} \theta \frac{1}{2} \left(\sigma^+ M^- + \sigma^- M^+ \right) + \frac{\theta^2}{4} \frac{1}{2} \left(\sigma^+ M^+ + \sigma^- M^- \right) \right] \tag{3.48}$$

equation 3.48 describe the hole-Mn interaction Hamiltonian, it can be divided in to three terms, the first term is the spin interaction in the z axis, it is an Ising type interaction, the second term describes the xx and yy spin interaction, is it an Heisenberg type interaction, the third term is in the second order of theta. Since θ is a small angle, the third term can be neglected safely. In the following part of the thesis, we use this approximation unless specified.

3.1.3.2 Influence of strain on the effective hole-Mn Hamiltonian

In 3.1.3.1 we derived the effective spin model for hole-Mn coupling from Kohn-Luttinger Hamiltonian, and equation (3.48) is a good enough approximation in most cases. However, in this section, we investigate how the hole-Mn interaction Hamiltonian in a self assembled quantum dot is effected by strain in detail. In this section, we derive the effective spin Hamiltonian using both Kohn-Luttinger and Bir-Pikkus Hamiltonian, illustrate the influence of Bir-Pikus Hamiltonian, the finally results suggests that the influence of Bir-Pikus is small.

From section 3.1.2.3, we know the strain has an influence on the wave function of holes (equation 3.20) compared to the wave function without strain (equation 3.12), we employ the similar procedure as in section 3.1.3.1, after a straightforward calculation, we get the effective hole-Mn coupling Hamiltonian:

$$\mathcal{V}_{h-Mn} = \frac{j_h}{2}\left[j_{xx}M_x\sigma_x + j_{xy}M_x\sigma_y + j_{yx}M_y\sigma_x + j_{yy}M_y\sigma_y + j_{zz}M_z\sigma_z\right] \tag{3.49}$$

with:

$$\begin{aligned}
j_{xx} &= (1-Cos\theta)Cos(2\phi_-) - Sin\theta Cos\phi_- && (3.50)\\
j_{xy} &= Sin\theta Sin\phi_- + (1-Cos\theta)Sin(-2\phi_-) && (3.51)\\
j_{yx} &= -Sin\theta Sin\phi_- + (1-Cos\theta)Sin(-2\phi_-) && (3.52)\\
j_{yy} &= -(1-Cos\theta)Cos(2\phi_-) - Sin\theta Cos\phi_- && (3.53)\\
j_{zz} &= 3Cos^2\frac{\theta}{2} - Sin^2\frac{\theta}{2} = 1 + 2Cos\theta && (3.54)
\end{aligned}$$

If we neglect valence band mixing, which means θ is small enough, for the first approximation, we can let $Sin\theta = 0$, the hole-Mn Hamiltonian has the Ising type: $\mathcal{V}_{h-Mn} = \frac{j_h}{2} j_{zz} M_z \sigma_z$. In our calculation, we need to calculate the influence of the valence band mixing wich means we do not have the approximation $Sin\theta = 0$. For simplicity, we can let $Sin(-2\phi_-) = 0$, then get the Heisenberg type Hamiltonian: $\mathcal{V}_{h-Mn} = \frac{j_h}{2}\left[j_{xx}M_x\sigma_x + j_{yy}M_y\sigma_y + j_{zz}M_z\sigma_z\right]$, which is the same as the equation we get in the previous section. Heisenberg type Hamiltonian is a good enough approximation for our calculation. If the strain effect on the effective hole-Mn coupling is not negligible, we have to consider all the terms coming from ϕ_-.

3.1.3.3 Electron-Mn Hamiltonian

In analogy to the hole-Mn bare coupling, the electron-Mn coupling reads:

$$\mathcal{V}_{\text{e-Mn}} = \alpha\delta(\vec{r}_e - \vec{r}_M)\vec{S}\cdot\vec{M} \tag{3.55}$$

where $\vec{S}$ is the spin of the electron. Since the spin orbit coupling has a very small effect on the s like conduction band, the effective exchange for the quantum dot electron and

the Mn is also a Heisenberg term given by

$$\mathcal{V}_{\text{e-Mn}} = j_e \vec{S} \cdot \vec{M} = j_e \left(S_x M_z + S_y M_y + S_z M_z \right) \tag{3.56}$$

where $j_e \equiv \alpha |\psi_0(\vec{r}_{Mn})|^2$ is the electron-Mn coupling constant, which depends both on a material dependent constant α and on a quantum dot dependent property, the probability of finding the electron at the Mn location. In the hard-wall model the orbital wave function for the confined electron and hole is the same, so that the ratio should be $j_h/j_e \simeq \frac{\beta}{3\alpha}$ for CdTe. However, in experiments the ratio is bigger than that(5). In the following we take j_e and j_h as adjustable parameters.

3.1.4 Exciton-Mn wavefunctions and energy levels

Let's now evaluate the wave functions and energy levels obtained for Mn doped quantum dots with this minimal Hamiltonian.

3.1.4.1 Hamiltonian

The effective Hamiltonian for the exciton in a single Mn doped CdTe quantum dot is the sum of the single ion magnetic anisotropy Hamiltonian, the Mn-electron and Mn-hole exchange coupling and the electron-hole exchange coupling

$$\mathcal{H} = \mathcal{H}_0 + \mathcal{V}_{e-Mn} + \mathcal{V}_{h-Mn} + \mathcal{V}_{e-h} \tag{3.57}$$

where

$$\mathcal{V}_{e-h} = j_{eh} S_z \sigma_h \tag{3.58}$$

is the electron hole exchange coupling, neglecting transverse components. Electron hole exchange is ferromagnetic ($j_{eh} < 0$) and splits the 4 exciton levels into two doublets, the low energy dark doublet ($\Uparrow\uparrow, \Downarrow\downarrow$), denoted by $X = \pm 2$ and the high energy bright doublet ($\Uparrow\downarrow, \Downarrow\uparrow$) ($X = \pm 1$).

Since we consider two electron states ($S_z = \uparrow, \downarrow$), two hole states ($\sigma_h = \Uparrow, \Downarrow$), and six Mn states $M_z = \pm\frac{5}{2}, \pm\frac{3}{2}, \pm\frac{1}{2}$, the Hilbert space for the Mn-exciton system has dimension 24. Whereas we do obtain the exact eigenstates of Hamiltonian (3.57) by numerical diagonalization, it is convenient for the discussion to relate them to eigenstate of the Ising, or spin conserving part, of the Hamiltonian:

$$\mathcal{H} = \mathcal{H}_{\text{Ising}} + \mathcal{H}_{\text{flip}} \tag{3.59}$$

where

$$\mathcal{H}_{\text{Ising}} = D_0 M_z^2 + j_{eh} S_z \sigma_h + j_e S_z M_z + j_h M_z \sigma_h \tag{3.60}$$

and

$$\mathcal{H}_{\text{flip}} = E(M_x^2 - M_y^2) + j_e\,(S_x M_x + S_y M_y) + \\ + (j_{hx}\sigma_x M_x + j_{hy}\sigma_y M_y) \tag{3.61}$$

If we expand j_{hx} and j_{hy} in the series of LH-HH mixing parameter θ, they are the same in the first order of θ. For simplicity, we take

$$j_{h\perp} \equiv j_{hx} = j_{hy} = j_h \frac{\theta}{2\sqrt{3}} \tag{3.62}$$

in the following calculation. In the case of a LH-HH mixing induced by the anisotropy of the confinement described by a hard-wall box shape potential, we get from the Kohn-Luttinger Hamiltonian:

$$\theta = \frac{\pi^2\sqrt{3}\gamma_2|\frac{1}{L_x^2} - \frac{1}{L_y^2}|}{\sqrt{3\pi^4\gamma_2^2\left(\frac{1}{L_x^2} - \frac{1}{L_y^2}\right)^2 + \gamma_1^2\left(\frac{-2}{L_z^2} + \frac{1}{L_x^2} + \frac{1}{L_y^2}\right)^2}} \tag{3.63}$$

The eigenstates of $\mathcal{H}_{\text{Ising}}$ are trivially given by the product basis

$$|P\rangle \equiv |M_z\rangle|S_z\rangle|\sigma_h\rangle \tag{3.64}$$

with eigenenergies:

$$E_P = D_0 M_z^2 + j_{eh} S_z \sigma_h + j_e S_z M_z + j_h M_z \sigma_h \tag{3.65}$$

Since the magnetic anisotropy term $D_0 M_z^2$ is present both in the ground state and exciton state manifolds, it does not affect the PL spectra of the bright excitons. Within this picture, for each of the 6 possible values of M_z, there are 4 exciton states. We use a short-hand notation to refer to the Ising states $P_X(M_z)$ where $X = \pm 1, \pm 2$ labels the spin of the exciton, $X = S_z + \sigma_z$. An energy diagram for the exciton levels, within the Ising approximation, is shown in figure (3.2).

The PL spectra of a single Mn doped quantum dot predicted by the model of Ising excitons, ie, neglecting the spin flip transitions, features 6 peaks corresponding to transitions conserving M_z. For the recombination of σ^+ excitons ($S_z = -\frac{1}{2}, \sigma_h = \Uparrow$) the high energy peak corresponds to $M_z = +\frac{5}{2}$ and the low energy peak to $M_z = -\frac{5}{2}$ on account of the antiferromagnetic coupling between the hole and the Mn. In the case of σ^- excitons the roles are reversed, but the PL spectrum is identical at zero magnetic field.

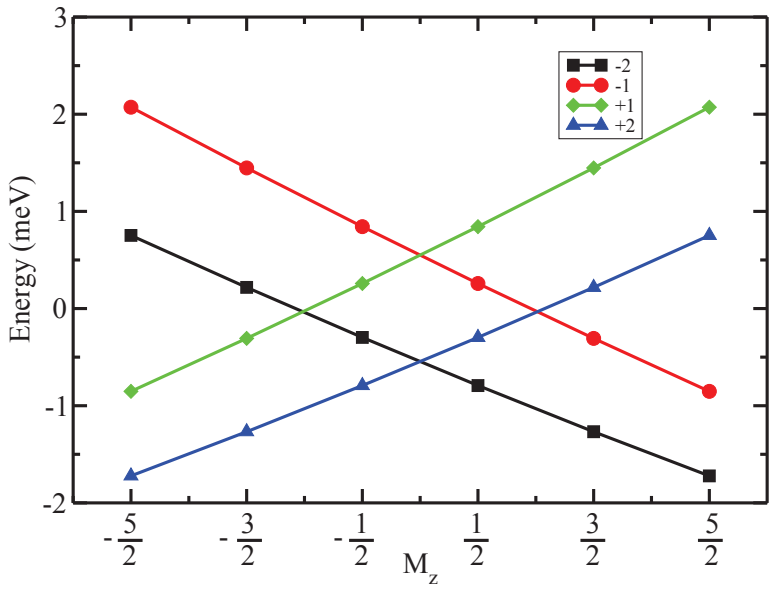

Figure 3.2: Scheme of the energy levels of the quantum dot exciton interacting with 1 Mn when spin-flip terms are neglected.

3.1.4.2 Wave functions

When spin-flip terms are restored in the Hamiltonian, the P states are no longer eigenstates, but they form a very convenient basis to expand the actual eigenstates of $\mathcal{H}$, denoted by $|\Psi_n\rangle$:

$$|\Psi_n\rangle = \sum_P \Psi_n(P)|P\rangle = \sum_{X,M_z} \Psi_n(X,M_z)|X,M_z\rangle \tag{3.66}$$

In most cases, there is a strong overlap between Ψ_n and a single state $|P\rangle$. This is expected for several reasons. First, the single ion in plane anisotropy is probably much smaller than the uniaxial anisotropy, $D_0 \gg E$. Second, the electron-hole exchange, which is the exchange energy in the system, splits the dark and bright levels. Thus, both electron and hole spin flip due to the exchange with the Mn spin is inhibited because they involve coupling between energy split bright and dark excitons. In addition, the electron Mn exchange is smaller than the hole Mn exchange, whose spin-flip part is proportional to the LH-HH mixing and approximately 10 times smaller than the Ising part. In order to quantify the degree of spin mixing of an exact exciton state Ψ_n, we

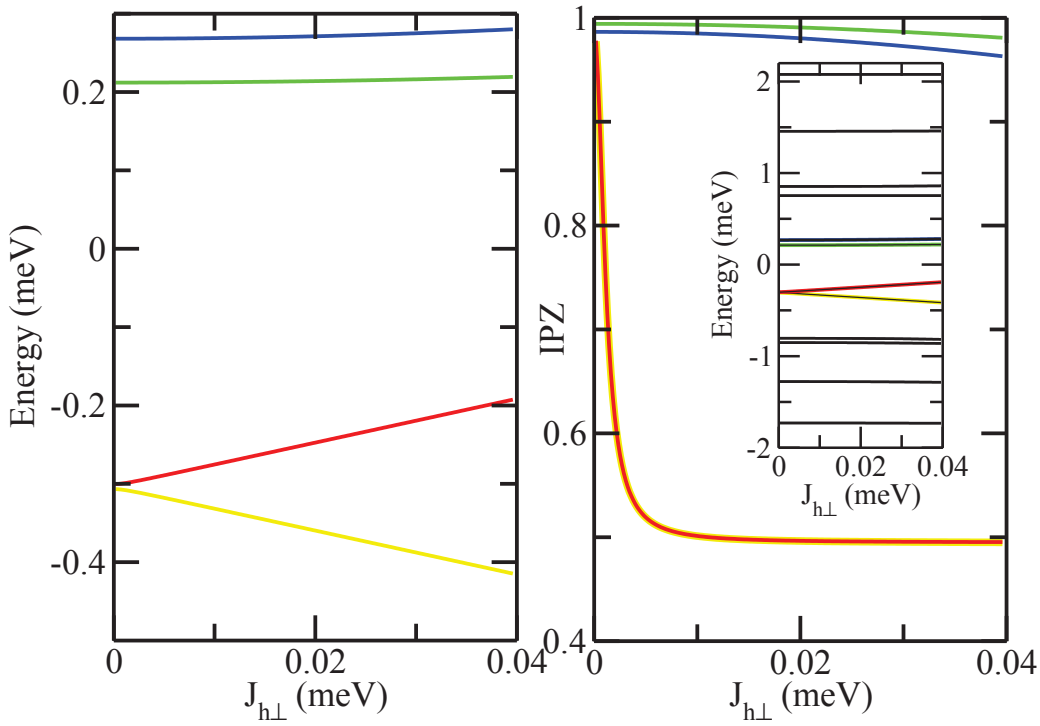

Figure 3.3: Left panel: Evolution of the exciton levels as a function of the LH-HH mixing parameter $J_{h\perp}$. Right panel: Evolution of the IPZ as a function of the LH-HH mixing parameter. The inset presents the evolution of the energy for all the 24 exciton levels.

define the inverse participation ratio:

$$IPZ_n \equiv \sum_P |\Psi_n(P)|^4 \tag{3.67}$$

This quantity gives a measure of the delocalization of the state Ψ_n on the space of product states of eq. (3.64). In the absence of mixing of different P states, we have $IPZ_n = 1$. In the case of a state equally delocalized in the 24 states of the P space, we would have $\Psi_n(P) = \frac{1}{\sqrt{24}}$ and $IPZ_n = \frac{1}{24}$.

In figure (3.3) we plot the evolution of both the energy (left panel) and the IPZ (right panel) as a function of $J_{h\perp}$, the LH-HH mixing parameter, of four states denoted by their dominant component at $J_{h\perp} = 0$. For our choice of exchange constants, two of them $|+1, -\frac{3}{2}\rangle$ and $|-2, -\frac{1}{2}\rangle$ are almost degenerate at $J_{h\perp} = 0$, which means that the hole-Mn exchange compensates the dark-bright splitting, and couple these states

via a hole-Mn spin flip. As a result, their energy levels split linearly as a function of $J_{h\perp}$ and the wave-functions have a large weight on the two product states for finite $J_{h\perp}$. In contrast, the other two levels shown in figure (3.3), $|+1,-\frac{1}{2}\rangle$ and $|-2,-\frac{3}{2}\rangle$ are not coupled via hole-Mn spin flip. As a result, their energies shift as a function of $J_{h\perp}$ due to coupling to other states, and their IPZ undergoes a minor change, reflecting moderate mixing.

3.1.4.3 Exchange induced dark-bright mixing

The most conspicuous experimentally observable consequence of the exchange induced mixing, is the transfer of optical weight from the bright to the dark exciton, which results in the observation of more than 6 peaks in the PL. This can be understood as follows. The spin-flip part of the hole-Mn interaction couples the bright exciton $|+1,M_z\rangle$ to the dark exciton $|-2,M_z+1\rangle$. Thus, a state with dominantly dark character $|-2,M_z+1\rangle$ and energy given, to first order, by that of the dark exciton, has a small but finite probability of emitting a photon through its bright component, via a Mn-hole coherent spin-flip. Thus, PL is seen at transition energy of the dark exciton. Reversely, nominally bright excitons loose optical weight due to their coupling to the dark sector. Importantly, the emission of a photon from a dark exciton with dominant Mn spin component M_z, entails carrier-Mn spin exchange, so that the ground state has $M_z \pm 1$.

Transitions from the optical excited states to the optical ground states happens via spontaneous emission of a photon with energy $\hbar\omega$ and circular polarization. We consider circularly polarized photons only. The rate of spontaneous emission of a photon with energy $\hbar\omega = E_X - E_G$ from the state $|X>$ to the state $|G>$ can be given by the Weisskopf-Wigner expression(see the reference: (17)): $\Gamma_{GX} = 4\omega^3/4\pi\epsilon\hbar c^3| < G|P^{\pm}|X > |^2$, where:

$$P^{\pm} = \sum_{\nu,n,\sigma} < \nu|e(x+iy)|n\sigma > d^{\dagger}_{\nu} c^{\dagger}_{n,\sigma} + H.c. \tag{3.68}$$

is the second quantization representation of the interband electric dipole operator that yields the standard optical selection rules, where $c_{n,\sigma}$ stands for the CB electron creation operator and d_ν stands for the creation operator for a hole. Standard optical selection rules forbid photon emission from $|\pm 2>_X$ states. Since the electric dipole operator does not affect the Mn d electrons, the Mn spin part of the collective wave function does not change during the recombination process. As a result, the rate for the emission of a circularly polarized photon from the exciton state Ψ_n to the ground state ϕ_m reads:

$$\Gamma^{\pm}_{n,m} = \Gamma_0 \left| \sum_{M_z} \phi_m(M_z) \Psi^*_n(M_z, X = \pm 1) \right|^2 \tag{3.69}$$

where

$$\Gamma_0 \equiv \frac{3\omega^3 d_{cv}^2}{4\pi\epsilon\hbar c^3} \tag{3.70}$$

is the recombination rate of the bare exciton, ω is the frequency associated to the energy difference between the exciton state n and the ground state m, c is the speed of light, ϵ is the dielectric constant of the material, d_{cv} is the dipole matrix element. From the experiments, we infer Γ_0 =5 ns^{-1}

In the absence of spin-flip terms, the matrix $\Gamma^{\pm}_{n,m}$ would have only non-zero elements for $n = |X = \pm 1, M_z\rangle$ states connected to $m = M_z$ states. The presence of spin-flip terms in the Hamiltonian enables the recombination from exciton states with dominant dark component. In figure (3.4) we represent the matrix elements $\Gamma^{\pm}_{n,m}/\Gamma_0$ for $j_{eh} = -0.73meV$, $j_h = 0.36meV$, $j_e = -0.09meV$, $j_{h\perp} = 0.036meV$, $D_0 = 0.01meV$ and $E = 0meV$. It is apparent that the recombination rates from the dark states are, at least, 2 times smaller (a and b) than those of the bright states. For Γ_0= 4 ns^{-1}, the lifetime of the dark excitons (a and b) are in the range of 1 ns. Thus, this provides a quite efficient Mn spin relaxation mechanism, provided that a dark exciton is present in the quantum dot.

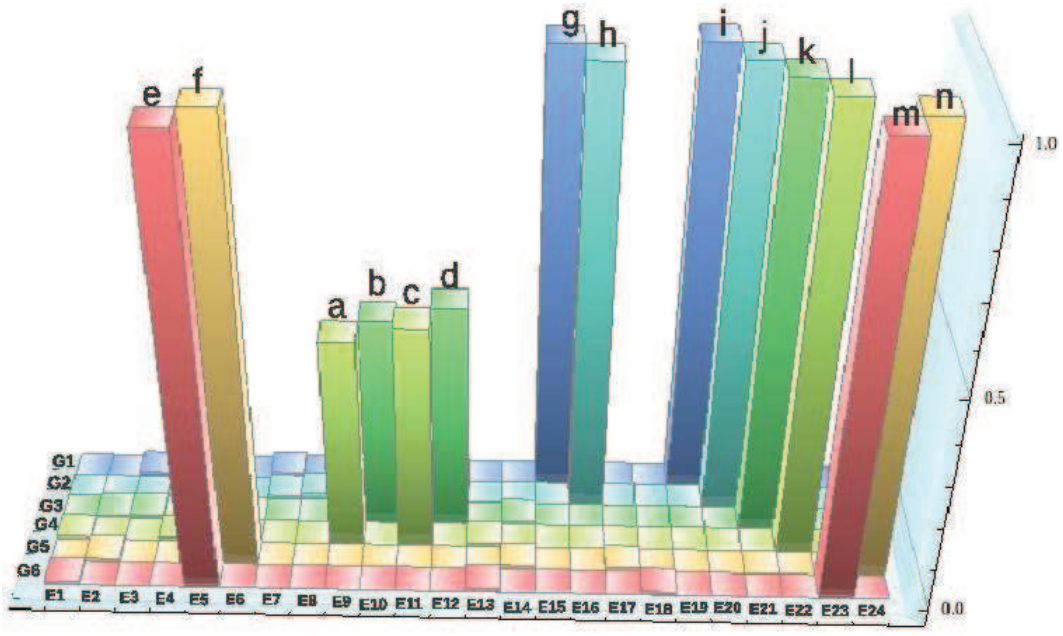

Figure 3.4: Recombination rates of the excitons levels in a Mn doped quantum dot Γ_i/Γ_0: $a : |+2, +\frac{1}{2}> \rightarrow |+\frac{3}{2}>$, $b : |-2, -\frac{1}{2}> \rightarrow |-\frac{3}{2}>$, $c : |-1, +\frac{3}{2}> \rightarrow |+\frac{3}{2}>$, $d : |+1, -\frac{3}{2}> \rightarrow |-\frac{3}{2}>$, states from e to n are bright excitons. Other states are mainly dark excitons with a small bright component.

The recombination rate matrix, together with the non-equilibrium occupation of the exciton states, P_n, determines the PL spectrum(17) for $\pm$ circular polarization:

$$\mathcal{I}^{\pm}_{\mathrm{PL}}(\omega) = \sum_{n,m,} P_n \Gamma^{\pm}_{n,m} \delta\left(\hbar\omega - E_n - E_m\right) \tag{3.71}$$

In a typical PL spectrum(11), the dark peaks are, at most, 2 times smaller than the bright peaks. Since $\Gamma^{\pm}_{n,m}$ is at least 2 times smaller for dark states, this implies a larger occupation of the dark states. Thus, we can infer a transfer from the optical ground state to the dark exciton states, via the bright exciton states. This transfer requires an incoherent spin flip of either the electron or hole. Below we show that phonon induced hole-spin relaxation provides the most efficient channel for this bright to dark conversion.

3.2 Detailed optical spectra of a Mn doped quantum dot

In this section, to get more detailed information of the Mn-exciton spectrum, we use the full basis for holes (-3/2, -1/2, +1/2, +3/2), instead of the pseudo spin approach used in section 3.1. We want first to estimate the influence of the Mn fine and hyperfine structure on the optical spectra of a singly Mn doped quantum dot. This would give an optical mean to measure the spin structure of an individual Mn atom in its solid state environment and eventually gives a technique to optically probe and control an individual nuclear spin. We will first analyze with a spin effective Hamiltonian the optical spectrum of a singly Mn doped quantum dot taking into account heavy hole and light hole and possible shape and strain anisotropy of the quantum dot. We will then introduce the coupling between electronic and nuclear spins of the Mn and see in which condition it can be detected in the optical spectrum of a neutral individual quantum dot. In the last part we will present and model the emission spectrum of quantum dots containing two Mn atoms. All this description is based on a spin effective Hamiltonian where the parameters are chosen to reproduce standard Mn doped quantum dots.

3.2.1 Detailed spin effective Hamiltonian of a Mn doped quantum dot.

Here we introduce the fine structure Hamiltonian for the exciton-Mn complex. Parameters of the effective Hamiltonian are chosen to reproduce the spectrum of a self assembled Mn doped II-VI quantum dots. For a sufficiently small number of Mn atoms (1 or 2 in this work, including electronic and nuclear spins) the size of the Hilbert space permits the exact numerical diagonalization of the Hamiltonian. The spectra are obtained from the exact eigenstates of the Hamiltonian.

The exciton-Mn complex Hamiltonian consist of six parts:

$$\mathcal{H}_{fine} = \mathcal{V}_{e-Mn} + \mathcal{H}_{h-Mn} + \mathcal{H}_{e-h} + \mathcal{H}_{mag} + \mathcal{H}_s + \mathcal{H}_X \tag{3.72}$$

which

$$\mathcal{H}_{h-Mn} = j_h \vec{M} \cdot \vec{J} \tag{3.73}$$

and

$$\mathcal{H}_s = A\vec{I} \cdot \vec{M} + D_0 M_z^2 + \frac{1}{6} a[M_x^4 + M_y^4 + M_z^4]$$

Comparing to $\mathcal{H}_0$ in equation 3.1, we assume the dot is isotropic in X-Y plane (E=0). The additional terms A and a are the hyperfine coupling and the tetragonal crystal field respectively.

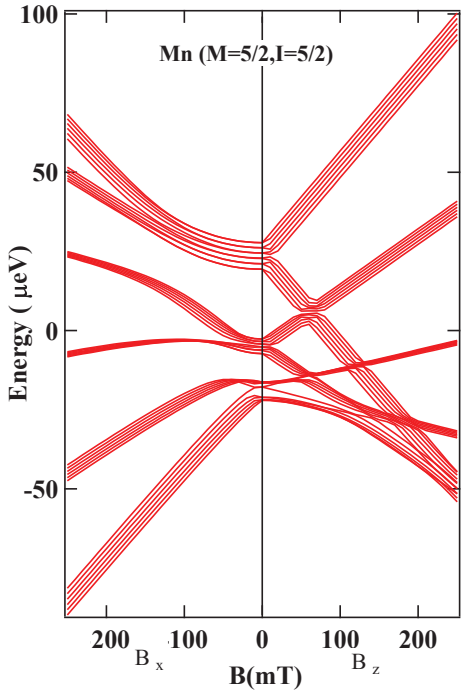

Figure 3.5: Magnetic field dependence of the fine structure of the Mn spin with out-of-plane (right) and in-plane (left) field, calculated with $A = 0.68$ μeV, $D_0 = 7$ μeV and a crystal field parameter $a = 0.32$ μeV.

An external magnetic field couples via the standard Zeeman term to both the Mn spin and carriers spins and a diamagnetic shift is also included:

$$\mathcal{H}_{mag} = g_{Mn}\mu_B \vec{B} \cdot \vec{M} + g_e \mu_B \vec{B} \cdot \vec{S} + g_h \mu_B \vec{B} \cdot \vec{J} + \gamma B^2 \tag{3.74}$$

The electron-hole exchange interaction $\mathcal{H}_{e-h}$ contains two parts. The short range part can be describe by the Hamiltonian:

$$\mathcal{H}_{e-h,sr} = j_{eh}\vec{S}\cdot\vec{J} + \sum_i b_i S_i J_i^3 \tag{3.75}$$

The first term already exists in spherical symmetry whereas the second term takes into account the reduction of the symmetry in a cubic crystal. The long range part mixes bright excitons confined in an anisotropic potential and can be represented in the heavy-hole exciton subspace ($J_z + S_z = +2, +1, -1, -2$) by:

$$\mathcal{H}_{exc,lr} = \begin{pmatrix} 0 & 0 & 0 & 0 \\ 0 & 0 & \frac{1}{2}\delta_2 e^{-2i\phi_2} & 0 \\ 0 & \frac{1}{2}\delta_2 e^{2i\phi_2} & 0 & 0 \\ 0 & 0 & 0 & 0 \end{pmatrix} \tag{3.76}$$

where δ_2 is the splitting of the bright exciton.

The exciton Hamiltonian $\mathcal{H}_X$ stand for the energy of the electron E_c, and the energy of the heavy-hole and light-hole. It has to take into account a possible valence band mixing that can be induced by an anisotropy of the potential confinement or an anisotropy of the strain distribution. In the case of a valence band mixing induced by the strain, the hole part of this Hamiltonian can be written, in the basis $(|\frac{3}{2},+\frac{3}{2}\rangle, |\frac{3}{2},+\frac{1}{2}\rangle, |\frac{3}{2},-\frac{1}{2}\rangle, |\frac{3}{2},-\frac{3}{2}\rangle)$ as (69):

$$\mathcal{H}_{vbm} = \begin{pmatrix} 0 & -S & R & 0 \\ -S^* & \Delta_{hh-lh} & 0 & R \\ R^* & 0 & \Delta_{hh-lh} & S \\ 0 & R^* & S^* & 0 \end{pmatrix} \tag{3.77}$$

with

$$\begin{aligned} S &= \delta_{xz} - i\delta_{yz} \\ R &= \delta_{xx,yy} - i\delta_{xy} \end{aligned} \tag{3.78}$$

R describe the mixing induced by an anisotropy in the quantum dot plane xy and S take into account an asymmetry in the plane containing the quantum dot growth axis. As we have discussed in the previous section, in the case of a valence band mixing induced by the strain, the δ_i can be linked to the deformation of the crystal by the Bir and Pikus Hamiltonian. Δ_{hh-lh} is the splitting between light holes and heavy holes controlled by the in-plane strain and the confinement. An Hamiltonian with the same symmetry can be used to describe the influence of an anisotropic confinement potential.

The Hamiltonian of the coupled electronic and nuclear Mn spins in the ground state reads (55):

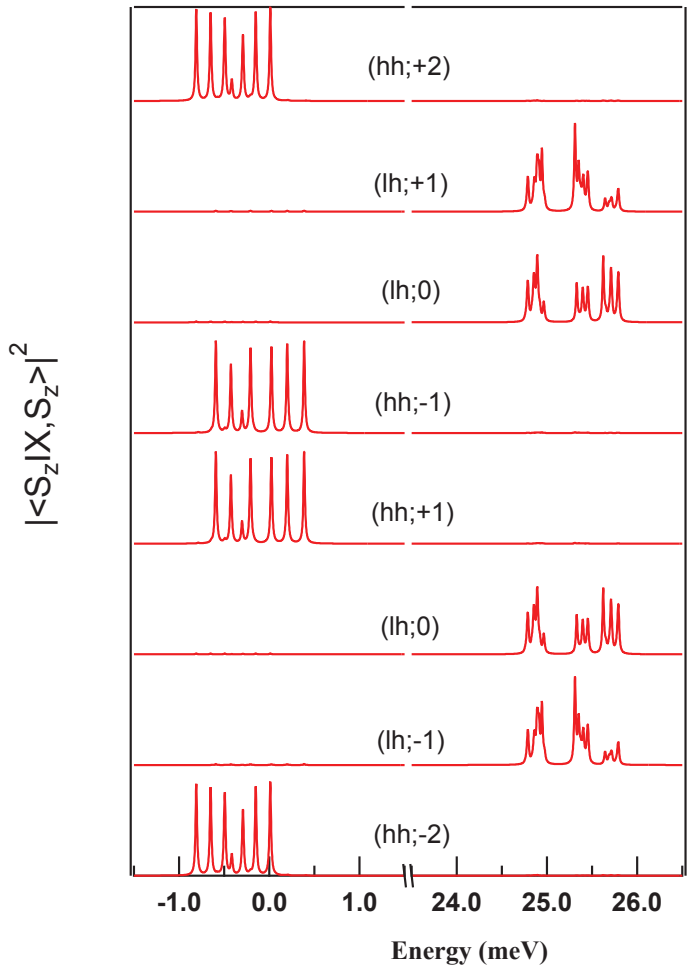

Figure 3.6: Calculated energy levels in a Mn doped quantum dot. The parameters used in the calculation are: $A = 0.68$ μeV, $D_0 = 7$ μeV, $a = 0.32$ μeV, $j_{eh} = -200$ μeV, $j_e = -30$ μeV, $j_h = 120$ μeV, Δ_{hh-lh}=25 meV, δ_{xz}=δ_{yz}=0, δ_{xy}=0, $\delta_{xx,yy}$=2.5 meV, $\delta_2 = 50$ μeV, ϕ_2=0, b_x=b_y=b_z=0.

$$\mathcal{H}_{Mn} = g\mu_B \vec{B} \cdot \vec{M} + \mathcal{H}_s \tag{3.79}$$

The resulting fine structure of the Mn under a magnetic field applied in-plane or out-of-plane is shown in Figure 3.5. At zero field, the Mn electronic spin is quantized along the growth axis and the different electronic spin doublets are separated by an energy proportional to D_0. Each level is further split into six lines by the hyperfine coupling.

Using the Hamiltonian of the excited state $\mathcal{H}_{X-Mn}$ (288 x 288 matrix) and the Hamiltonian of the ground state $\mathcal{H}_{Mn}$ (36 x 36 matrix), we can compute the spectrum of a neutral quantum dot containing a Mn atom. They are obtained calculating the matrix elements $|\langle M_z|X, M_z\rangle|^2$ where X stands for the 8 possible exciton states.

An example of calculated spectrum of a Mn doped quantum dot is presented in Figure 3.6. The parameters used for this calculation are listed in the caption of the figure. They are determined to reproduce the emission spectrum of typical II-VI Mn doped quantum dots. The appearance of a seventh line in the spectrum of the bright heavy hole levels is characteristic of the presence of hole-Mn spins flips. These spin flips are allowed by a mixing with light holes produced by an anisotropy in the quantum dot plane ($\delta_{xx,yy} \neq 0$ for instance). We will in the following particularly analyze the influence the fine and hyperfine structure of the Mn spin controlled by the parameters D_0 and A on the spectrum of the ground state heavy-hole neutral exciton.

3.2.2 Influence of A and D_0 on the optical spectrum of a neutral quantum dot

In the case of a neutral quantum dot, as the Mn spin M_z is conserved during the optical transition, one expect no signature of D_0 in the optical spectra of the bright excitons. On the other hand, the hyperfine coupling A mixes the different spin sate of the Mn. This isotropic coupling is partially blocked by the magnetic anisotropy D_0 except for the states M_z=$\pm$1/2 where flip-flop with the nuclear spin are completely allowed. Depending on the relative value of D_0 and A, an influence of the Mn fine and hyperfine structure on the exciton-Mn emission is expected. This is illustrated in Figure 3.7. In the absence of valence band mixing, a clear influence of A is obtained in the intensity distribution of the calculated spectrum: a decrease of the intensity of the center lines corresponding to M_z=$\pm$1/2 is observed. Such decrease could also be observed in the presence of a significant valence band mixing but in this case, the intensity distribution is mainly controlled by the coupling with light holes.

One way to tune the influence of the hyperfine coupling is to apply a magnetic field in the Faraday configuration. When the Zeeman energy of the Mn dominates the hyperfine energy, a quantization axis along z is restored for the Mn alone. The

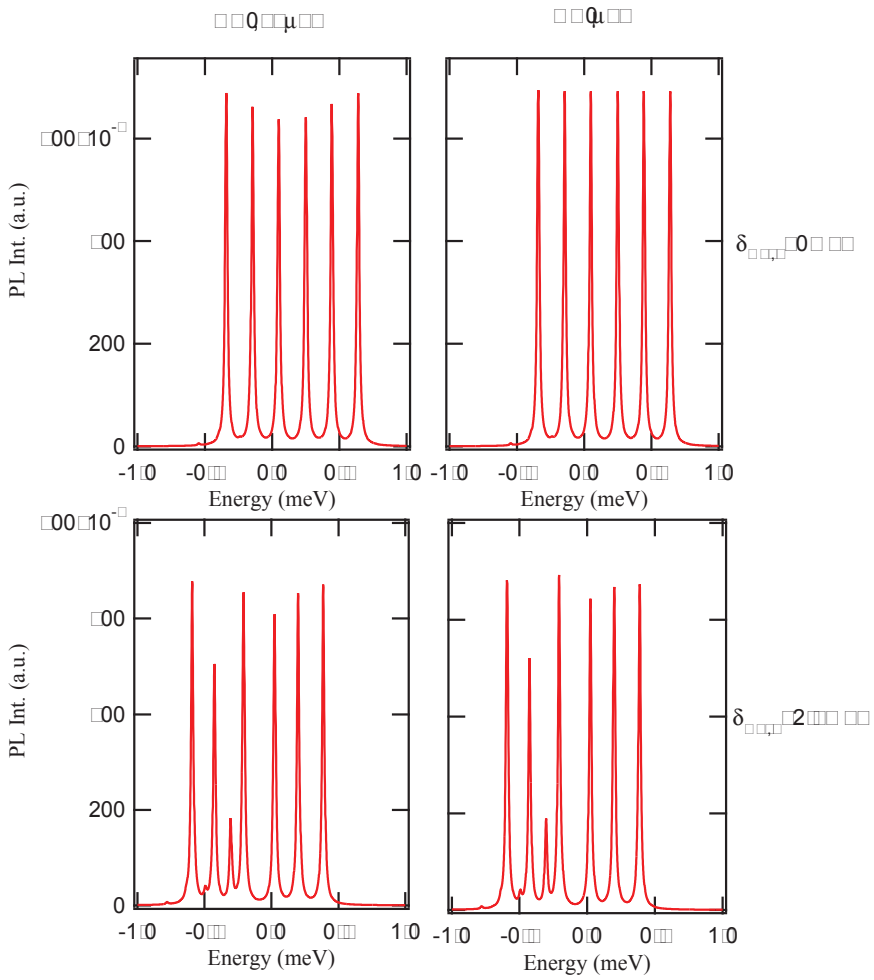

Figure 3.7: Calculated spectrum of the ground state of a Mn doped quantum dot in circular polarisation with (lower panels) and without (upper panels) valence band mixing for A=0.68μeV (left panels) and A=0μeV (right panels). The other parameters are the same as in Figure 3.6.

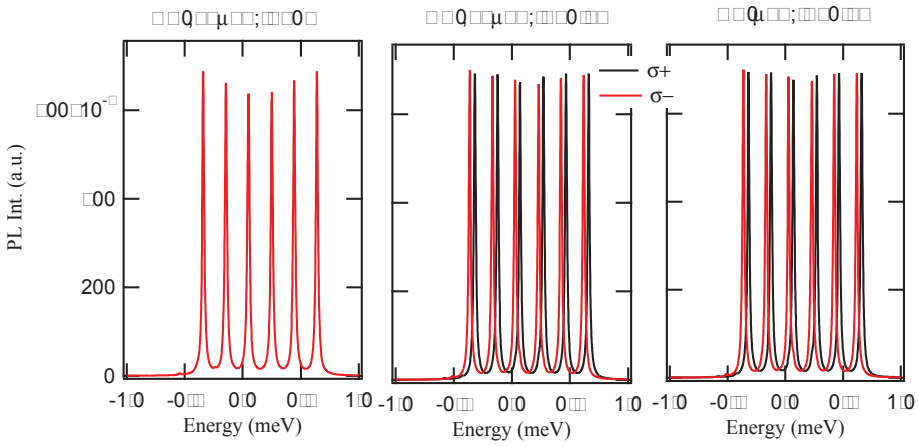

Figure 3.8: Calculated spectrum of the ground state of a Mn doped quantum dot in circular polarization under magnetic field in Faraday configuration (two right panels) compared with the spectrum at zero field (left panel). The other parameters are the same as in Figure 3.6.

influence of A on the emission spectrum vanishes. The influence of a magnetic field in the Faraday configuration is illustrated in Figure 3.8. Under a field B_z=0.4T no significant influence of A is observed in the circularly polarized PL spectrum.

As presented in Figure 3.9, D_0 also influence the position of the dark exciton state as there emission is coming from a hole Mn flip-flop . A more direct way to observe the effect of D_0 is to analyze the spectrum of charged quantum dot.

3.3 Spectrum of quantum dots containing two Mn atoms: experiment and model.

Here we analyze how the optical spectra of the quantum dot evolves as the number of Mn atoms increases. We consider the case of quantum dots containing a pair of Mn atoms that we recently identified in experimental spectrum. A photoluminescence spectrum of such quantum dot is presented in Figure 3.10. As in non-magnetic or singly Mn-doped quantum dots, the emission of the neutral exciton, negatively charged exciton and biexciton are simultaneously observed. For each excitonic complexe, a fine structure coming for the exchange interaction with the two Mn spins is observed. To understand the detail of this quantum dot emission, a modeling of these two Mn quantum dots has to be performed.

To compute the quantum dot spectrum, two Mn atoms with coupling ($j_{e,1}$,$j_{h,1}$) and ($j_{e,2}$,$j_{h,2}$) are introduced in the spin effective Hamiltonian presented previously.

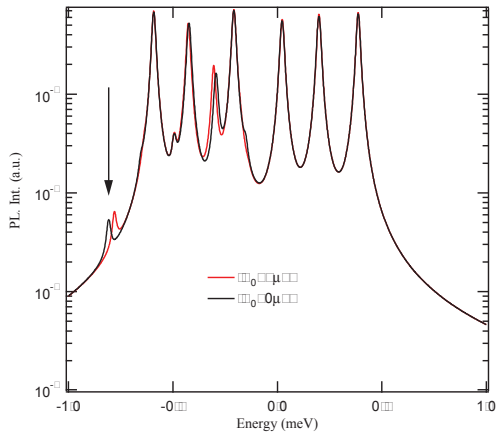

Figure 3.9: Calculated spectrum of the ground state of a Mn doped quantum dot in circular polarization with $D_0 = 0$ and D_0=7μeV. The other parameters are the same as in Figure 3.6.

We will, in a first approximation, neglect the anti-ferromagnetic Mn-Mn interaction which strongly decrease with the distance between the two Mn spins (72). A valence band mixing induced by the anisotropy of the quantum dot can be included. For this particular calculation, we consider a weak valence band mixing and use a development of the ladder operators $\tilde{J}^+$ and $\tilde{J}^-$ in $\mathcal{H}_{h-Mn}$ in the heavy hole subspace:

$$\tilde{J}^+ = \frac{\rho}{\Delta_{lh-hh}} \begin{pmatrix} 0 & -2\sqrt{3}e^{-2i\theta} \\ 0 & 0 \end{pmatrix}; \tilde{J}^- = \frac{\rho}{\Delta_{lh-hh}} \begin{pmatrix} 0 & 0 \\ -2\sqrt{3}e^{2i\theta} & 0 \end{pmatrix}$$

$$\tilde{J}_z = \begin{pmatrix} 3/2 & 0 \\ 0 & -3/2 \end{pmatrix}$$

where ρ describes the coupling energy between heavy-holes and light-holes split by Δ_{lh-hh}. The sample growth direction is $z(001)$ axis. θ is the strain induced anisotropy respect to the $x(100)$ axis, in our particular case, $\theta = 0$. The carrier-Mn coupling in a quantum dots containing two Mn can be written:

$$\mathcal{H}_{carrier-Mn} = \mathcal{H}_{h-Mn} + \mathcal{H}_{e-Mn} \tag{3.80}$$

$$\tag{3.81}$$

where

$$\begin{aligned} \mathcal{H}_{h-Mn} &= j_{h,1}\vec{M}\cdot\vec{J} + j_{h,2}\vec{M}\cdot\vec{J} \\ &= j_{h,1}M_z\tilde{J}_z + \frac{j_{h,1}}{2}(M^+\tilde{J}^- + M^-\tilde{J}^+) \\ &\quad + j_{h,2}M_z\tilde{J}_z + \frac{j_{h,2}}{2}(M^+\tilde{J}^- + M^-\tilde{J}^+) \end{aligned} \tag{3.82}$$

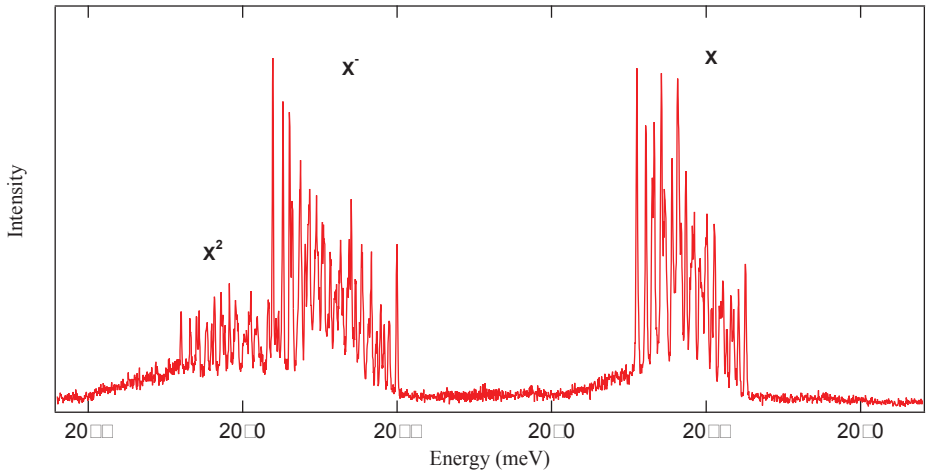

Figure 3.10: Low temperature (T=5K) emission of a CdTe/ZnMgTe quantum dot containing two Mn atoms. Three groups of lines are observed corresponding to the emission of the exciton, of the negatively charged exciton and biexciton.

and

$$\begin{aligned}\mathcal{H}_{e-Mn} &= j_{e,1}\vec{M}\cdot\vec{S} + j_{e,2}\vec{M}\cdot\vec{S} \\ &= j_{e,1}M_zS_z + \frac{j_{e,1}}{2}(M^+S^- + M^-S^+) \\ &\quad + j_{e,2}M_zS_z + \frac{j_{e,2}}{2}(M^+S^- + M^-S^+)\end{aligned} \tag{3.83}$$

The symmetric case where the two Mn atoms are identically coupled to the carriers shows a spectrum with 11 lines corresponding to quantum states with the 2M +1 possible orientations of the collective M_z of the two Mn atoms (M=5) (17). For different coupling of the two atoms, a much more complicated spectrum appears. This is the situation which is observed experimentally.

Using a similar spin effective Hamiltonian, the emission spectrum of the negatively charged exciton can be computed. It corresponds to the transitions between an initial state where the 2 Mn interact with a hole spin and two paired electron spins and a final state where the remaining electron is exchanged coupled with the two Mn spins. We will neglect in a first approximation the energy correction produced by the Mn-Mn interaction mediated by the presence of the two electrons in the initial state (72). We then consider the optical transitions between the hole-2Mn and the electron-2Mn complexes.

Calculated emission spectra for a neutral and negatively charged exciton coupled to two Mn spin are presented in Figure 3.11. The main feature (*i.e.* overall splitting,

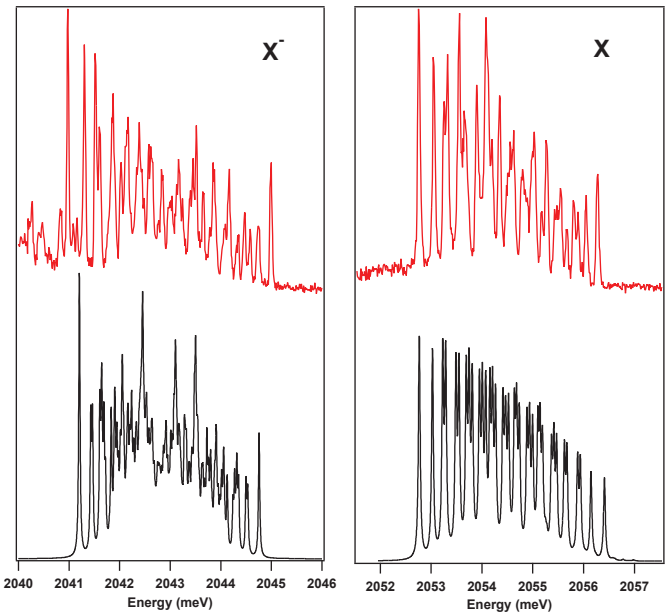

Figure 3.11: Calculated (black) and experimental (red) spectrum of a neutral (right) and negatively charged (left) 2 Mn doped quantum dot. The calculation are performed with $j_{e,1}$=-55μeV,$j_{h,1}$=150μeV, $j_{e,2}$=-90μeV,$j_{h,2}$=270μeV, $j_{eh} = -600\mu$eV and an effective valence band mixing parameter ρ/Δ_{lh-hh}=0.025. A thermalization with an effective temperature T=40K is included for X-2Mn and for h-2Mn in the initial state of the negatively charged exciton transition.

number of lines, linear polarization) of the experimental spectra can be reproduced. The quantum dot presented in Figure 3.10 corresponds to a situation where the coupling with Mn(1) is about twice the coupling with Mn(2). To reproduce the intensity distribution of the photoluminescence spectra, a thermalization on the exciton-2Mn levels with an effective temperature T=40K is included in the model. Surprisingly, a thermalization on the hole-2Mn levels has to be also included to reproduce the charged exciton spectrum suggesting an efficient hole-2Mn spin relaxation during the lifetime of X^-.

As for singly Mn doped quantum dots, the overall splitting of the charged exciton is larger than the one obtained with the values of exchange integrals used for the calculation of the neutral exciton spectra (69). In CdTe/ZnTe quantum dots, the confinement of the hole is strongly influenced by the Coulomb attraction of the confined electron. The hole-Mn exchange integral is maximum in the excited state of X^- where the Coulomb attraction of two electrons confined the hole.

A linear polarization rate is observed in the center of the emission spectra for both

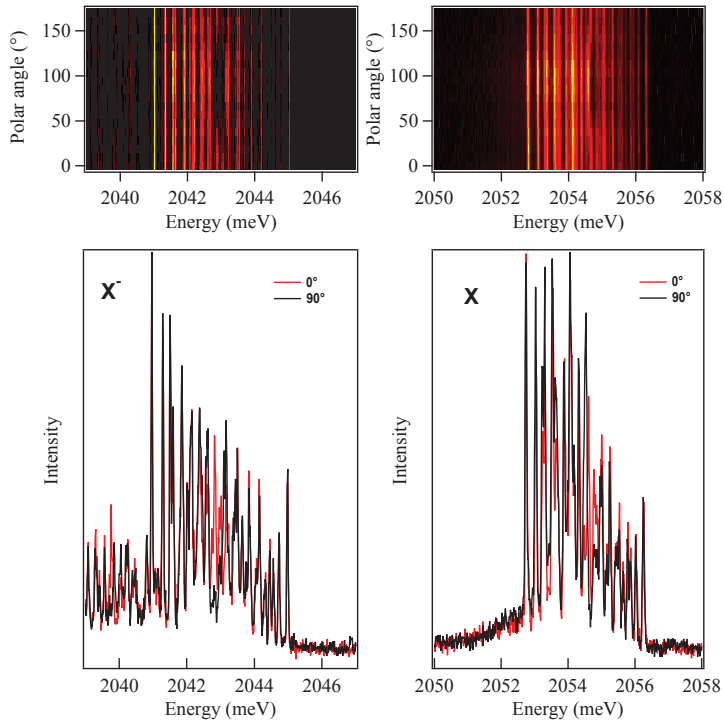

Figure 3.12: Experimental polarization resolved spectrum of a neutral (right) and negatively charged (left) 2 Mn doped quantum dot obtained at T=5K.

the neutral and the charged exciton (Figure 3.12). As in singly Mn-doped quantum dot, this polarization rate is coming from the presence of a valence band mixing.

Valence band mixing combined with the short range electron-hole exchange interaction couples the bright excitons +1 and -1 associated to the same Mn spins configuration producing linear polarization. In the absence of electron hole exchange interaction (case of a charged exciton) the presence of valence band mixing allows simultaneous hole-Mn flip-flop. This introduces coupling between different states of the hole - 2Mn complex in the initial state of the negatively charged exciton optical transition. This linear polarization is well reproduced by the spin effective model if an effective valence band mixing is introduced (Figure 3.13).

3.4 Conclusion

We have described the different terms in the Mn spin Hamiltonian, including exchange with the 0-dimensional exciton, presented the Mn spin Hamiltonian with or without the presence of the exciton, derived the effective Mn-hole coupling employing the pseudo

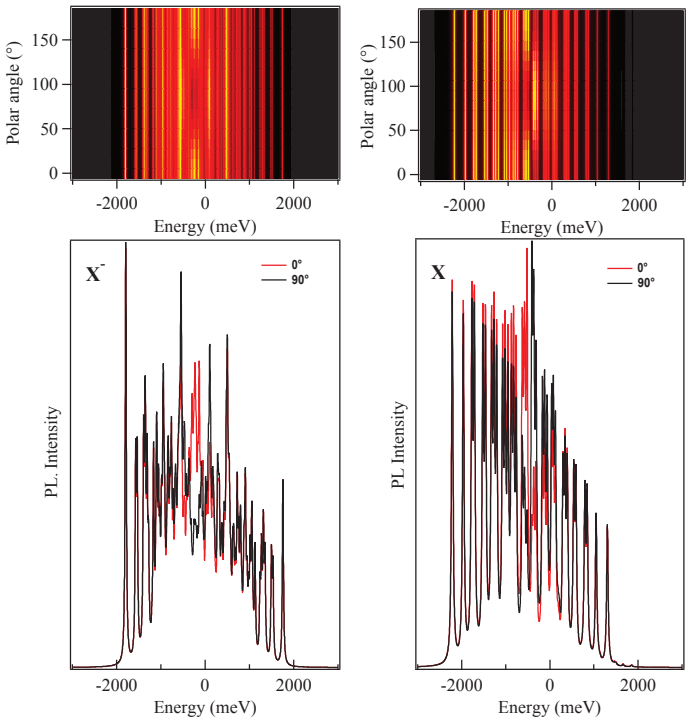

Figure 3.13: Calculated polarization resolved spectrum of a neutral (right) and negatively charged (left) 2 Mn doped quantum dot. The calculation are performed with $j_{e,1}$=-55 μeV,$j_{h,1}$=150μeV, $j_{e,2}$=-90μeV,$j_{h,2}$=270μeV, $j_{eh} = -600$ μeV and an effective valence band mixing parameter ρ/Δ_{lh-hh}=0.025. A thermalization with an effective temperature T=40K is included for X-2Mn and for h-2Mn in the initial state of the negatively charged exciton transition.

spin method. The symmetry of the exchange interaction depends on the spin properties of the carriers, which in the case of holes are strongly affected by the interplay of confinement, strain and spin orbit coupling. In section (3.1) we also use a model for holes(17, 67, 73) in quantum dots, which permits to obtain analytical expressions for the wave functions of the holes, the hole-Mn exchange, in terms of the dimensions of the dot and the Kohh-Luttinger Hamiltonian. We also calculated the detailed spectrum of Mn-exciton complex using a spin effective Hamiltonian and studied influence of A and D_0 on the spectrum. For isotropic quantum dots one expect an influence of the nuclear Mn spin on the optical emission of the exciton confined in a Mn-doped CdTe quantum dot. In realistic quantum dots, this effect can be partially masked by the dominant contribution of the electron-hole exchange interaction in an anisotropic potential or in the presence of an anisotropic in-plane strain distribution. Then we presented and modelled the emission spectrum of quantum dot containing two Mn atoms. Even if an accurate fit is difficult, a spin effective Hamiltonian permits to describe the main feature of the spectra

4

Phonon induced spin relaxation

Contents

In this chapter we discuss the Mn-phonon, hole-phonon coupling and the transition rates caused by spin-phonon coupling in detail. In the first part of this chapter, we present a general formula for phonon-induced spin-flip rate. In the second part of this chapter, we discuss the Mn spin relaxation in the absence of excitons and then discuss how the rates are modified when an exciton is interacting with the Mn. In the third part we propose a simple model for the spin relaxation of holes confined in quantum dots and split by the exchange interaction with Mn spin. The single particle spectra of holes is described within the Kohn Luttinger model plus a hard wall potential(67). The effect of time dependent strain is described by the Bir-Pikus Hamiltonian. We follow the standard master equation approach(74) to calculate the rates, considering two states of holes and the acoustic phonons as a reservoir.

4.1 General formula for phonon-induced spin-flip rate

In this section we derive a general formula for the scattering rate between two electronic state n and n' induced by a phonon emission. The Hamiltonian of the system can be split in three parts, the electronic states n, the phonon states, and their mutual coupling. The phonon states are labelled according to their polarization and momentum, λ, $\vec{q}$. We consider the following coupling

$$\mathcal{V} = \sum_{m,m',\vec{q},\lambda} \mathcal{V}^{m,m'}_{\vec{q},\lambda} |m\rangle\langle m'| \left(b^\dagger_{\lambda q} + b_{\lambda,-q} \right) \tag{4.1}$$

where m and m' are electronic states. We refer to the free phonon states as the reservoir states. Within the Born-Markov approximation, the scattering rate between states n and n' is given by:

$$\Gamma_{n\to n'} = \frac{2\pi}{\hbar} \sum_r P_r \sum_{r'} \left| \langle nr|V|n'r'\rangle \right|^2 \delta\left(E_n - E_{n'} + e_r - e_{r'}\right) \tag{4.2}$$

where P_r is the occupation of the r reservoir state with energy e_r. This equation can be interpreted as a statistical average over reservoir initial states r of the Fermi Golden rule decay rate of state N, r.

The sums over r and r' are performed using the following trick. For a given r, the initial reservoir state, r' must have an additional phonon, since we consider the phonon emission case. Thus, we write:

$$|r'\rangle = \frac{1}{\sqrt{n_{\lambda',q'}+1}} b^\dagger_{\lambda',q'} |r\rangle \tag{4.3}$$

so that

$$\langle r| b^\dagger_{q,\lambda} + b_{-q,\lambda} |r'\rangle = \delta_{-q,q'}\delta_{\lambda,\lambda'} \sqrt{n^r_{\lambda',q'}+1} \tag{4.4}$$

The matrix element

$$\langle nr|V|n'r'\rangle = \mathcal{V}^{n,n'}_{\vec{q},\lambda} \sqrt{n^r_{\lambda',q'}+1} \tag{4.5}$$

We see for all the terms in the sum that defines the coupling, only one survives and fixes the index r'. Thus, the only term that the sums left are the one over the initial reservoir states and the λ, q index which define the final state. Now we use the definition of the Bose function:

$$\sum_r P_r \left(n^r_{\lambda',q'} + 1 \right) = n_B\left(\omega_{\lambda'}(q')\right) + 1 \tag{4.6}$$

and we arrive to the following expression for the rate:

$$\Gamma_{n\to n'} = \frac{2\pi}{\hbar} \sum_{\lambda,q} |\mathcal{V}^{n,n'}_{\vec{q},\lambda}|^2 \left(n_B\left(\omega_\lambda(q)\right) + 1\right) \delta\left(E_n - E_{n'} - \omega_\lambda(q)\right) \tag{4.7}$$

Notice that it is possible to write the rate as a sum over different contributions arising from different polarizations, $\Gamma = \sum_\lambda \Gamma_\lambda$. In the particular case where we can neglect the dependence of the matrix element $\mathcal{V}_{\vec{q},\lambda}(n,n') \simeq |\mathcal{V}_{(n,n')}|^2$ on $\vec{q}$ and λ, we arrive to the following expression:

$$\Gamma_{n\to n'} = \frac{2\pi}{\hbar}\left(n_B\left(\Delta\right)+1\right)\rho_\lambda(\Delta)|\mathcal{V}_{n,n'}|^2 \tag{4.8}$$

where $\rho(\Delta) \equiv \sum_{\lambda,q}\delta\left(\Delta-\omega_\lambda(q)\right)$ is the density of states of the phonons evaluated at the transition energy Δ.

4.2 Mn spin relaxation due to spin-phonon coupling

In this section we discuss the Mn spin relaxation in the absence of excitons. In the absence of carriers and given the fact that Mn-Mn distance is comparable to the dot-dot distance (100 nm for a dot and Mn density of about $10^{10}cm^{-2}$), which makes direct super-exchange negligible, the Mn-phonon coupling should be the dominant, albeit small, Mn spin relaxation mechanism. Transverse phonons induce local rotations of the lattice. Since the crystal field, together with spin orbit coupling, determines the Mn magnetocrystalline anisotropy, the phonon induced lattice rotation (75) acts as a stochastic torque on the Mn spin, resulting in spin relaxation.

As we discussed in chapter 3, the phonon can modulate the electric crystal field surrounding the magnetic atom, since the field interacts with the orbital momentum of the ion, it can finally interacts with the spin via the spin-orbit coupling. The atomic displacement at point $\vec{r}$ in the crystal is expressed in terms of the phonon operators with wave vector $\vec{q}$, polarization mode $\lambda = T1, T2, L$, frequency $\omega_\lambda(\vec{q})$ and polarization vector $\vec{e}_\lambda(\vec{q})$(68):

$$\vec{u}(\vec{r}) = \sum_{\vec{q},\lambda}\mathcal{U}_\lambda(\vec{q})\vec{e}_\lambda(\vec{q})\left(b^\dagger_{\vec{q},\lambda}+b_{-\vec{q},\lambda}\right)e^{i\vec{q}\cdot\vec{r}} \tag{4.9}$$

where

$$\mathcal{U}_\lambda(\vec{q}) = \sqrt{\frac{\hbar}{2\rho\omega_\lambda(\vec{q})V}} \tag{4.10}$$

and V and ρ are the volume of the crystal and the mass density respectively. In a zinc-blende structure there are two transverse acoustic (TA) phonon branches and one longitudinal acoustic branch (LA). Following Woods(76) we have:

$$\vec{e}_{TA1} = \frac{1}{qq_\perp}\left(q_xq_z, q_yq_z, -q_\perp^2\right) \tag{4.11}$$

$$\vec{e}_{TA2} = \frac{1}{q_\perp}\left(q_y, -q_x, 0\right) \tag{4.12}$$

where $q \equiv |\vec{q}|$ and $q_\perp = \sqrt{q_x^2 + q_y^2}$. These vectors satisfy $\vec{q}\cdot\vec{e}_{TAi} = 0$, and $\vec{e}_{TAi}\cdot\vec{e}_{TAj} = \delta_{ij}$ The longitudinal mode has $\vec{e}_{LA} = \frac{1}{q}\vec{q}$.

The lattice rotation vector is given by (75)

$$\delta\vec{\Phi}(\vec{r}) = \vec{\nabla} \times \vec{u}(\vec{r}) \tag{4.13}$$

so that only the transverse modes contribute. Within this picture, the Mn spin-phonon coupling can be written as(75):

$$\mathcal{V}_{\mathrm{M-ph}} = i\left[\mathcal{H}_0, \vec{M}\right] \cdot \delta\vec{\Phi}(\vec{r}_{Mn}) \tag{4.14}$$

Without loss of generality we can set the Mn position as the origin, $\vec{r}_{Mn} = 0$. Equation (4.14) couples the Mn spin to a reservoir of phonons whose non-interacting Hamiltonian is

$$\mathcal{H}_{\mathrm{ph}} = \sum_{\vec{q},\lambda} \hbar\omega_\lambda(\vec{q}) b^\dagger_{\vec{q},\lambda} b_{\vec{q},\lambda} \tag{4.15}$$

Within the standard system plus reservoir master equation approach, we have derived the scattering rate from a state n to a state n', both eigenstates of the single Mn Hamiltonian $\mathcal{H}_0$, due the emission of a phonon. In order to use a general result for that rate (4.7), derived in section (4.1), we need to express the spin-phonon coupling (4.14) using the same notation than in equation (4.1):

$$\mathcal{V}^{n,n'}_{\vec{q},\lambda} = i^2 \mathcal{U}_\lambda(\vec{q}) \vec{f}_{n,n'} \cdot (\vec{q} \times \vec{e}_\lambda(\vec{q})) \tag{4.16}$$

where

$$\vec{f}_{n,n'} \equiv \langle n| \left[\mathcal{H}_0, \vec{M}\right] |n'\rangle \tag{4.17}$$

We compute now the scattering rate due to a single phonon emission assuming the 3 dimensional phonons modes described above. The rate reads:

$$\Gamma_{n\to n'} = \frac{|\Delta|^3}{12\pi\rho\hbar^4 c^5}(n_B(\Delta)+1) \sum_{b,b'=x,y,z} f^b_{n',n}(f^{b'}_{n',n})^* \tag{4.18}$$

where $c = 1.79\mathrm{kms}^{-1}$ is the CdTe speed of sound(77), $\rho = 5870\mathrm{kgm}^{-3}$ is the mass density of the CdTe unit cell(78) and $n_B(\Delta) \equiv \frac{1}{e^{\beta|\Delta|}-1}$. The $|\Delta|^3$ factor comes from the dependence of the phonon density of states on the energy.

4.2.1 Mn spin relaxation in the optical ground state

We now discuss the relaxation of the Mn electronic spin due to spin-phonon coupling without an exciton in the quantum dot. According to our experimental results(10, 11), the Mn spin relaxation time in our samples is at least 5μs.

If we take $E = 0$, the transition rate between the excited states $|\phi_n\rangle = |M_z = +\frac{5}{2}\rangle$ and $|\phi_{n'}\rangle = |M_z = +\frac{3}{2}\rangle$, via a phonon emission, is given by:

$$\Gamma_{n\to n'} = \frac{640|D_0|^5}{3\pi\rho\hbar^4 c^5}(n_B(\Delta)+1) \tag{4.19}$$

The dependence on D_0^5 comes both from the density of states of phonons $\rho \propto \omega^3$ and the square of the Mn phonon coupling, which is proportional to the anisotropy, and gives the additional D_0^2 factor. Whereas the uniaxial anisotropy of Mn in CdTe quantum wells has been determined by EPR (61), the actual value for Mn in quantum dots is not known and can not be measured directly from single exciton spectroscopy of neutral dots. Therefore, in figure (4.1) we plot the lifetime for the transition of the Mn spin from $\frac{5}{2}$ to $\frac{3}{2}$, due to a phonon emission, as a function of D_0. We take D_0 in a range around the value reported for CdTe:Mn epilayers, $D_0 = 12\mu$eV (61). We find that the spin lifetime of Mn in the optical ground state can be very large. Even for $D_0 = 20\mu eV$ the Mn spin lifetime is in the range of 0.1 seconds, well above the lower limit for the Mn spin relaxation reported experimentally(10, 11). Whereas we can not rule out completely that the Mn spin lifetimes that long, there are other spin relaxation mechanisms that might be more efficient that the Mn-phonon coupling considered above, like the coupling of the Mn electronic spin to nuclear spins of Mn and the host atoms(10).

This model can be used also in the limit case where the D_0 is much smaller and the energy splittings given by the applied field B. In that case one could expect spin relaxation rates proportional to B^5. This B^5 behavior has been observed(79) in very diluted ($x = 0.002$) bulk $Cd_{1-x}Mn_xTe$ at very high magnetic fields $B > 10T$, giving qualitative support to the assumption that phonon-induced relaxation is the dominant mechanism in the dilute limit. Quantitatively, though, the observed relaxation rate at $B = 20T$ was $\Gamma \simeq 10^6 s^{-1}$, which corresponds to a lifetime of $T_1 \simeq 1\mu s$ for a splitting of 1 meV, much larger than what we would extrapolate from figure (4.1).

Since part of the Δ^5 scaling arises from the ω^3 scaling of the phonon density of states, we have explored the possibility that phonons localized in the wetting layer could be more efficient in relaxing the Mn spin. For that matter we have considered a toy model of two dimensional phonons confined in a slab of thickness $W = 2\,nm$. The resulting Mn spin relaxation rate for those reads:

$$\Gamma_{n\to n'} = \frac{\Delta^2}{16\hbar^3 c^4 \rho W}(n_B(\Delta)+1)\sum_{b,b'=x,y,z} A_{b,b'} f^b_{n',n}(f^{b'}_{n',n})^* \tag{4.20}$$

where W is the width of the sample and A is a diagonal matrix with $A_{xx} = 1$, $A_{yy} = 1$, $A_{zz} = 2$.

In figure (4.1) we plot the associated spin lifetime in this case, taking $W = 2nm$

and show how it is at least 100 shorter than for 3D phonons, but still we would have $T_1 \simeq 1$ ms for $D_0 = 20\mu$eV.

4.2.2 Mn spin relaxation in the presence of an exciton

Here we discuss how the Mn spin relaxation due to Mn-phonon coupling is modified when an exciton is interacting with the Mn. The Mn-phonon coupling is still given by Hamiltonian (4.14), with $\mathcal{H}_0$ given by eq. (3.1). We assume that the only effect of the exciton on the Mn is to change the energy spectrum and mix the spin wave-functions, giving rise to larger spin relaxation rates, due to the larger exchange-induced energy splittings.

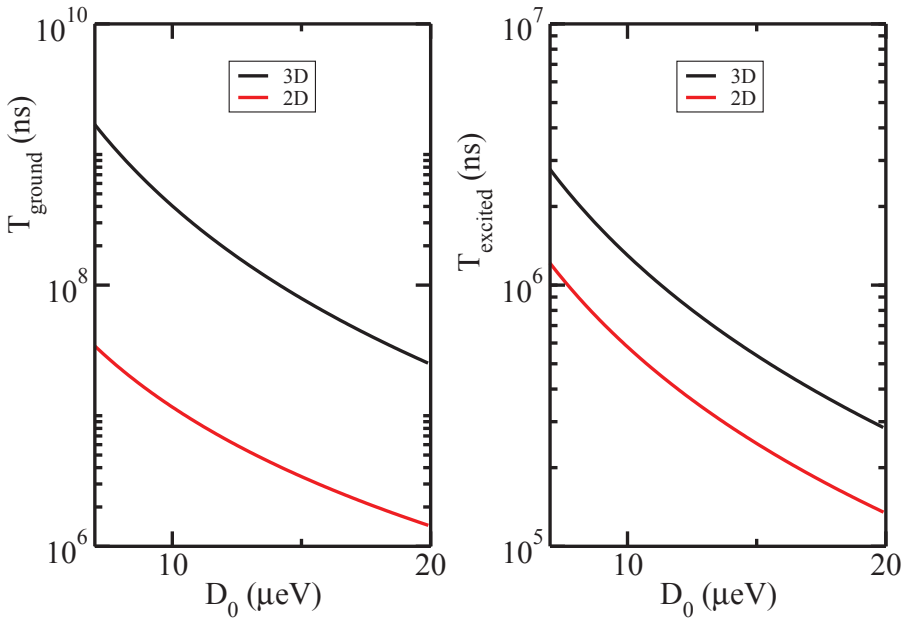

Figure 4.1: Left panel: Lifetime of the ($+\frac{5}{2}$ to $+\frac{3}{2}$) transition in the optical ground state at zero field as a function of the magnetic anisotropy energy splitting D_0. Right panel: Lifetime of the same transition in the presence of a +1 exciton for different values of D_0. The rates are calculated for a 3 dimensional (3D) and a 2 dimensional (2D) density of states of acoustic phonons.

In the presence of the exciton, the Mn-phonon coupling results in transitions between different exciton-Mn spin states, n and n'. As we did in the case of the Mn without excitons, we need to express the spin-phonon coupling (4.14) using the same

notation than in equation (4.1).

For that matter we define the matrix elements

$$\vec{F}_{n,n'} \equiv \langle \Psi_n | \left[\mathcal{H}_0, \vec{M} \right] | \Psi'_n \rangle = \sum_{X, M_z, M'_z} \Psi_n(X, M)^* \Psi_n(X, M')^* \vec{f}_{M,M'} \tag{4.21}$$

where

$$\vec{f}_{M,M'} \equiv \langle M | \left[\mathcal{H}_0, \vec{M} \right] | M' \rangle \tag{4.22}$$

M and M' stand for eigenstates of the Mn spin operator M_z. Thus, in the exciton-Mn spin states basis, the Mn-phonon coupling reads:

$$\mathcal{V}^{n,n'}_{\vec{q},\lambda} = i^2 \mathcal{U}_\lambda(\vec{q}) \vec{F}_{n,n'}(M) \cdot (\vec{q} \times \vec{e}_\lambda(\vec{q})) \tag{4.23}$$

Notice how if we neglect the spin mixing of the exciton states we have $\vec{F}_{n,n'} = \vec{f}_{M,M'}$ and the only difference in the scattering rates arises from the larger energy splittings in the presence of the exciton.

Using the equation (4.7) for the phonon induced spin relaxation rate, and in analogy with equation (4.18) we write:

$$\Gamma_{n \to n'} = \frac{|\Delta|^3}{12\pi\rho\hbar^4 c^5} (n_B(\Delta) + 1) \sum_{b,b'=x,y,z} F^b_{n,n'} (F^{b'}_{n,n'})^* \tag{4.24}$$

In figure (4.1) we see how Mn-phonon spin relaxation is much faster in the presence of the exciton. Ignoring the difference arising from the spin mixing, we can write the ratio of the rates as:

$$\frac{\Gamma_{n \to n'}(X)}{\Gamma_{n \to n'}(G)} = \left(\frac{\Delta_X}{\Delta_G} \right)^3 \tag{4.25}$$

The energy splitting associated to the $\frac{5}{2}$ to $\frac{3}{2}$ spin flip in the ground state is $4D_0$. In the presence of the exciton the energy splitting of the same transition would be $4D_0 + j_h - j_e$. If we take $D_0 = 12\mu$eV, $j_h = 360\mu$eV and $j_e = -90\mu$eV the ratio yields $\approx 10^3$. From the experimental side we know that $T_{1G} > 5\mu s$ and, in the presence of the exciton $T_1 \simeq 50ns$. Thus, the ratio could be accounted for by this mechanism. However, in order to have $T_{1G} = 5\mu$s we would need to assume an unrealistically large value for D_0. Thus, we think that another spin relaxation mechanism must be operative in the system when the exciton is in the dot which makes it possible to control the spin of the Mn in a time scale of 50 ns. In the next sections we discuss the hole spin relaxation due to phonons as the mechanism that, combined with Mn-carrier exchange, yields a quick Mn spin relaxation in the presence of the exciton.

4.3 Hole-phonon coupling in Mn doped quantum dot

4.3.1 Hole spin relaxation in non magnetic dots

We now consider the relaxation of the hole spin due to hole-phonon coupling. We consider first the case of undoped quantum dots. The coupling of the spin of the hole to phonons can be understood extending the Bir-Pikus Hamiltonian to the case of inhomogeneous strain associated to lattice vibrations:

$$\epsilon_{ij}(\vec{r}) \equiv \frac{1}{2}\left(\frac{\partial u_i}{\partial r_j} + \frac{\partial u_j}{\partial r_i}\right) \tag{4.26}$$

It is convenient to write the strain tensor field as:

$$\epsilon_{ij}(\vec{r}) = \sum_{\vec{q}} e^{i\vec{q}\cdot\vec{r}}\epsilon_{ij}(\vec{q}) \tag{4.27}$$

so that we write:

$$\epsilon_{ij}(\vec{q}) = \frac{1}{2}\sum_{\lambda} \mathcal{U}_\lambda(\vec{q})\left(b^\dagger_{\vec{q},\lambda} + b_{-\vec{q},\lambda}\right)\left(q_j e^i_\lambda(\vec{q}) + q_i e^j_\lambda(\vec{q})\right) \tag{4.28}$$

We consider the coupling of the ground state doublet, formed by states $\Uparrow$ and $\Downarrow$, to the phonon reservoir (80, 81, 82). The effective hole-phonon Hamiltonian is obtained by projecting the BP Hamiltonian onto this subspace:

$$\mathcal{V}_{\mathrm{h-phonon}} = \sum_{ij,\vec{q}\sigma_h,\sigma'_h} I^{\sigma_h,\sigma'_h}_{ij}(\vec{q})|\sigma_h\rangle\langle\sigma'_h|\epsilon_{ij}(\vec{q}) \tag{4.29}$$

Here $|\sigma_h\rangle$ denotes the quantum dot state defined in eq. (3.20) and the coupling constant reads

$$I^{\sigma_h,\sigma'_h}_{ij}(\vec{q}) \equiv \sum_{j_z,j'_z} V_{ij}\mathcal{C}^*_h(j_z)\mathcal{C}_{h'}(j'_z)\langle j_z|J_iJ_j|j'_z\rangle I_{\vec{q}} \tag{4.30}$$

where $I_{\vec{q}} = \int |\psi_0(\vec{r})|^2 e^{i\vec{q}\cdot\vec{r}}d\vec{r}$. Hamiltonian (4.29) shows how the absorption or emission of a phonon can induce a transition between the two quantum dot hole states, $\Uparrow$ and $\Downarrow$.

We now calculate the time scale for the spin relaxation of a single hole in a non magnetic dot under the influence of an applied magnetic field so that the hole ground state doublet is split in energy. In order to compute the transition rate for decay of the hole from the excited to the ground state we use again the general equation (4.7). For that matter, we express the hole-spin coupling (4.29) as:

$$\mathcal{V}_{\mathrm{h-phonon}} = \sum_{\vec{q},\lambda\sigma_h,\sigma'_h} \mathcal{V}^{\sigma_h,\sigma'_h}_{\vec{q},\lambda}|\sigma_h\rangle\langle\sigma'_h|\left(b^\dagger_{\lambda q} + b_{\lambda,-q}\right) \tag{4.31}$$

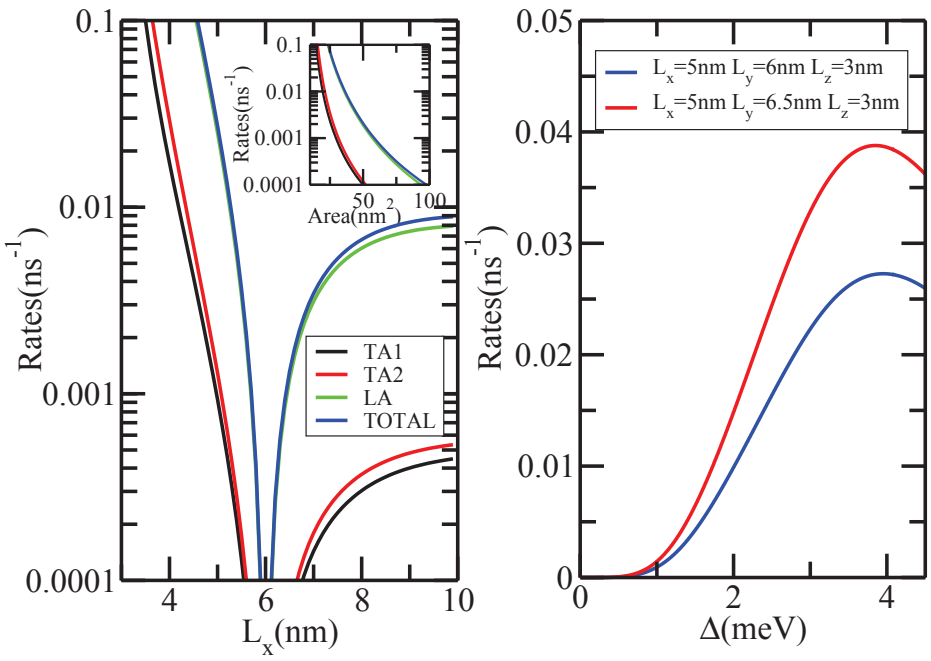

Figure 4.2: Left panel: Hole spin-flip rate as a function of the dot size and shape. L_y is fixed at 6nm, scanning of L_x change the LH-HH mixing. In the inset the ratio L_y/L_x is fixed at 1.2 so the shape of the dot are fixed, only the size of the dot changes. One can see that the hole spin-flip rate is a size sensitive quantum quantity, the rate is a semi-exponential function of the size of the dot. Right panel: Hole spin-flip rate as a function of the energy splitting for two different values of the quantum dot anisotropy, ie LH-HH mixing.

where

$$\mathcal{V}_{\vec{q},\lambda}^{\sigma_h,\sigma'_h} = \frac{i}{2}\sum_{i,j} I_{ij}^{\sigma_h,\sigma'_h}(\vec{q})\mathcal{U}_\lambda(\vec{q})\left(q_i e_\lambda^j(\vec{q}) + q_j e_\lambda^i(\vec{q})\right) \tag{4.32}$$

In order to illustrate the physics of the phonon-driven hole spin relaxation, we consider the case of a single hole in a non-magnetic dot under the influence of an applied magnetic field. For that matter, we compute the Hamiltonian (4.32) using the wave functions from the simple model of confined holes defined in eq. (3.12). We focus on the non-diagonal terms in the hole spin index, i.e., the terms that result in scattering form $\Uparrow$ to $\Downarrow$ due to phonon emission.

Importantly, the BP Hamiltonian couples hole states that differ in, at most, two units of J_z. Thus, in the absence of LH-HH mixing, the BP Hamiltonian does not couple directly the $\Uparrow$ and $\Downarrow$ states. Transitions between $\Uparrow$ and $\Downarrow$ states, as defined in eq. (3.20), are only possible, through one phonon processes, through the $\epsilon_{yz}(J_yJ_z + J_zJ_y)$ and $\epsilon_{zx}(J_zJ_x + J_xJ_z)$ terms in the Hamiltonian. After a straightforward calculation we obtain:

$$\mathcal{V}_{\vec{q},\lambda}^{\Uparrow,\Downarrow} = \frac{i}{2}\sqrt{3}dSin\left(\frac{\theta_1-\theta_2}{2}\right)\left(\epsilon_{yz}(\vec{q}) - i\epsilon_{zx}(\vec{q})\right) \tag{4.33}$$

The important role played by the $LH-HH$ mixing $\theta_{1,2}$ is apparent. Using equation (4.7) it is quite straightforward to compute the rate for the 3 phonon branches. They are all proportional to

$$\Gamma^0_{\Uparrow\to\Downarrow} = \frac{1}{18\pi}D_{u'}^2 Sin^2\left(\frac{\theta_1-\theta_2}{2}\right)\frac{\Delta^3}{\rho\hbar^4c^5} \tag{4.34}$$

with coefficients $\frac{7}{5}$, 1 and $\frac{8}{5}$ for the TA1, TA2 and L modes respectively. Here, $D_{u'}$ stands for the deformation potential of Kleiner-Roth(83), following reference (66), $D_{u'} = -\frac{3\sqrt{3}d}{2}$, ρ for the mass density of CdTe, c for its transverse speed of sound, and Δ for the energy splitting between the $\Uparrow$ and $\Downarrow$ states, which is proportional to the external magnetic field B. In figure (4.2) we plot the rates $\Gamma_{TA1}, \Gamma_{TA2}, \Gamma_L$, as well as their sum as function of the dot size (left panel) and as a function of the energy splitting between the initial and final hole state, Δ (right panel). We see how hole spin relaxation rates can be in the range of $\Gamma \simeq 1/(40ns)$.

The results of figure (4.2) suggest that for sufficiently high Δ, as those provided by the Mn-hole exchange, the hole spin can relax in a time scale of $30ns$. These numbers are in the same range than those obtained by Woods et al (76). As we discuss in the next section, these spin flips, together with Mn-carrier exchange, can also induce Mn spin relaxation in a time scale much shorter than the one due to Mn-phonon coupling only. Notice that the saturation of the hole spin relaxation rate as the energy splitting is increased is related to the phonon wavelength becoming smaller than the dot size, leading to a suppression of the matrix element $I_{\vec{q}}$ (84).

Importantly, the rate is finite only if $\theta_1 - \theta_2 \neq 0$, which is the case in the presence of an applied magnetic field. This indicates that, within the simple model of eq. (3.12), the non-diagonal terms in the hole-phonon Hamiltonian (4.29) vanishes identically. Similar cancellation of the spin relaxation at zero field occur in other models and might be a general result (85). The exchange coupling of the hole to either Mn or electron spin are expected to have a similar effect on the hole wave functions, and thereby on the phonon-induced hole spin relaxation, than the magnetic field. However, this effect is only captured if the system is described with the complete hole basis, ie, without removing from the Hilbert space the 2 high energy hole states. It is worth pointing out that hole spin relaxation is thereby very different if an electron (or a Mn atom) is present in the dot. In the presence of an electron, zero field hole spin relaxation can take place(81).

4.3.2 Spin relaxation in magnetic dots due to hole-phonon coupling

The results of the previous sections indicate that, because of their coupling to phonons, the hole spin lifetime in a non-magnetic dot is much shorter than the Mn spin lifetime. Here we explore the consequences of this phonon-driven hole spin relaxation for the single exciton states in a dot doped with one magnetic atom. The leading process results in a Mn spin conserving decay from the bright exciton to the dark exciton state, via hole-spin flip in a time scale in the 10 ns range. Combined with the optical recombination of the dark state, made possible via Mn-hole or Mn-electron spin flip, provide a pathway for exciton induced Mn spin relaxation in a time scale under 100 ns, as observed experimentally (6, 10, 11).

We also explore the scattering between two bright states enabled by the combination of phonon induced hole spin relaxation and Mn-carrier exchange. The lifetimes of these processes is in the range of 10^3 ns and higher, and therefore they are probably not determinant for the optical orientation of the Mn spin in the sub-microsecond scale.

4.3.2.1 Exciton-phonon coupling in magnetic dots

The Hamiltonian that couples the exciton states Ψ_n to the phonons is derived by projecting the hole-phonon coupling Hamiltonian (4.29) onto the exciton states (3.66). The result reads:

$$\mathcal{V}_{\mathrm{X-phon}} = \sum_{n,n'\vec{q}\lambda} |\Psi_n\rangle\langle\Psi_{n'}| \mathcal{V}^{n,n'}_{\vec{q},\lambda} \left(b^{\dagger}_{\lambda q} + b_{\lambda,-q} \right) \tag{4.35}$$

where

$$\mathcal{V}^{n,n'}_{\vec{q},\lambda} = \sum_{M_z,\sigma_e,\sigma_h,\sigma'_h} \mathcal{V}^{\sigma_h,\sigma'_h}_{\vec{q},\lambda} \Psi_n(M_z, X) \Psi^*_{n'}(M_z, X') \tag{4.36}$$

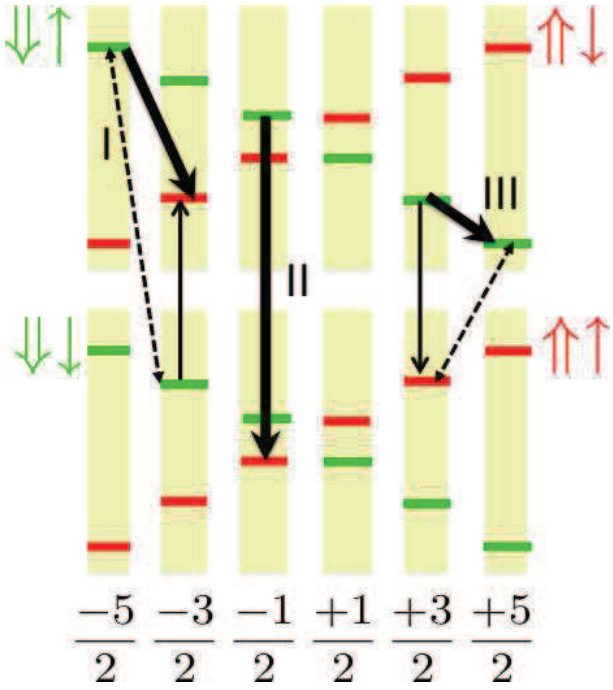

Figure 4.3: Scheme of the Mn spin flip channels due to the combined action of hole-phonon coupling and carrier-Mn exchange.

where $X = (\sigma_e, \sigma_h)$ and $X' = (\sigma_e, \sigma'_h)$ (same electron spin) and $\mathcal{V}_{\vec{q},\lambda}^{\sigma_h,\sigma'_h}$ is given by equation (4.32).

4.3.2.2 Qualitative description of the spin relaxation processes

In order to describe qualitatively the variety of different processes accounted for by Hamiltonian (4.35) it is convenient to consider an initial state ψ_n as a linear combination of a dominant component $|M\rangle|\downarrow\rangle_e|\Uparrow\rangle_h$ plus a minor contribution of two dark components, which arise from the coherent exchange of the Mn with either the electron or the hole:

$$\begin{aligned} |\psi_n\rangle &= |M\rangle|\downarrow\rangle_e|\Uparrow\rangle_h + \\ &+ \quad \epsilon_e|M-1\rangle|\uparrow\rangle_e|\Uparrow\rangle_h + \epsilon_h|M+1\rangle|\downarrow\rangle_e|\Downarrow\rangle_h \end{aligned} \tag{4.37}$$

where $\epsilon_e \propto j_e/j_{eh}$ and $\epsilon_h \propto j_h/j_{eh}$ are small dimensionless coefficients that can be obtained doing perturbation theory.

Depending on the elementary process that takes place, there are several possible final states:

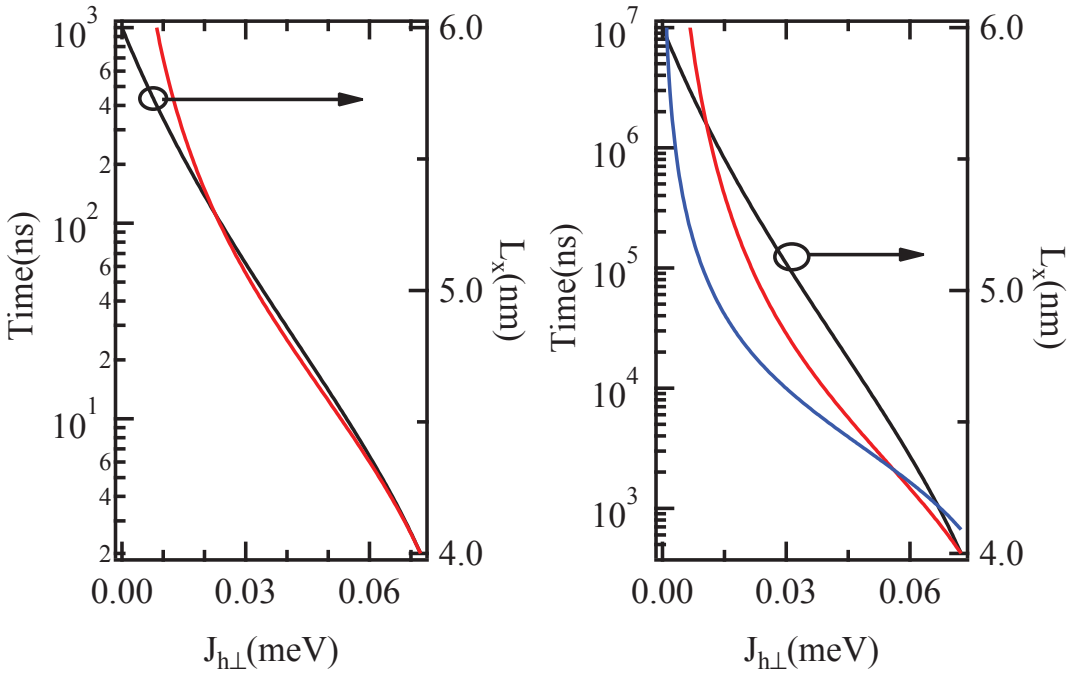

Figure 4.4: Calculated rates for the transitions between exciton states in a Mn-doped quantum dot due to hole-phonon coupling. Left panel, red line, transition from $|-1,-\frac{5}{2}>$ to $|+2,-\frac{5}{2}>$, Right panel, red line, transition from$|-1,-\frac{5}{2}>$ to $|-2,-\frac{1}{2}>$. Blue line, transition from $|-1,-\frac{5}{2}>$ to $|+1,-\frac{3}{2}>$. L_y is fixed at 6nm and scanning L_x changes the LH-HH mixing parameter $J_{h\perp}$.

1. Hole spin relaxation. In this case the final state would be dominantly a dark exciton whose wave function read:

$$|\psi_{n'}\rangle \quad = \quad |M\rangle|\downarrow\rangle_e|\Downarrow\rangle_h + O(\epsilon) \tag{4.38}$$

and the scattering rate Γ_0 would be proportional to $|I^{\Uparrow,\Downarrow}|^2$. This is process II in figure (4.3).

2. Hole spin relaxation plus coherent hole-Mn spin flip. This is process III in figure (4.3). This can be realized through two dominant channels. An incoherent hole spin flip will couple the dominant component of the initial state, $|M\rangle|\ \downarrow\rangle_e|\Uparrow\rangle_h$ with a secondary component $|M\rangle|\downarrow\rangle_e|\Downarrow\rangle_h$ of the final state

$$\begin{aligned} |\psi_{n'}\rangle \quad &= \quad |M-1\rangle|\downarrow\rangle_e|\Uparrow\rangle_h + \\ + \qquad &\epsilon_h|M\rangle|\downarrow\rangle_e|\Downarrow\rangle_h + O(\epsilon_e) \end{aligned} \tag{4.39}$$

In this case the final state is a bright exciton in the same branch +1 than the initial state but the Mn component goes from M to $M-1$.

The second channel comes from the hole spin flip of the minority dark component of the initial state, $\epsilon_h|M+1\rangle|\downarrow\rangle_e|\Downarrow\rangle_h$ which decays into the majority component of the final state

$$|\psi_{n'}\rangle \quad = \quad |M+1\rangle|\downarrow\rangle_e|\Uparrow\rangle_h + O(\epsilon_{e,h}) \tag{4.40}$$

Thus, in this second case a hole spin flips due to phonons, plus a coherent Mn-electron spin flip connect the $X=+1, M$ initial state to the $X=-1, M+1$ state. Thus, both the initial and final state in this process are the same than in the first channel, the rates for each would be proportional to $\epsilon_h^2\Gamma_0$, but the decay pathways are different, and interferences are expected.

3. Hole spin relaxation plus coherent electron-Mn spin flip. This is process I in figure (4.3). As in the previous case, there are two channels for this type of process. In the first channel, the majority component of the initial state decays into a final state given by:

$$|\psi_{n'}\rangle \quad = \quad |M-1\rangle|\uparrow\rangle_e|\Downarrow\rangle_h + \epsilon'_e|M\rangle|\downarrow\rangle_e|\Downarrow\rangle_h \tag{4.41}$$

The incoherent hole spin flip connects the initial state (4.37) to the final state (4.41) through the minority component $|M\rangle|\downarrow\rangle_e|\Downarrow\rangle_h$ of the later.

The second channel comes from the hole spin flip of the minority dark component of the initial state, $\epsilon_e|M-1\rangle|\uparrow\rangle_e|\Uparrow\rangle_h$ which decays into the majority component of the final state

$$|\psi_{n'}\rangle \quad = \quad |M-1\rangle|\uparrow\rangle_e|\Downarrow\rangle_h + O(\epsilon_{e,h}) \tag{4.42}$$

Thus, a hole spin flips due the phonon, plus a coherent Mn-electron spin flip connect the $X=+1, M$ initial state to the $X=-1, M-1$ state. The scattering rate of these two process scales as $\epsilon_e^2\Gamma_0$

4.3.2.3 Calculation of the relaxation rates

In order to implement equations (4.35 and 4.36) to compute scattering rates, we use the single particle basis for the holes done with equations (3.12) which leads, at finite magnetic field to the matrix element (4.33) that would be incorporated into equations (4.36) to compute the rates using equation (4.7). As discussed above, a zero field model (3.12) yields a zero spin-flip matrix element in equation (4.33). This is a feature of the simple hole model rather than an intrinsic property of the system. Thus, for the sake of simplicity, we compute the rates between exciton states by computing the matrix element (4.33) as if there was a magnetic field that yields the energy splitting between the initial and final exciton states equal to the splitting produced by the exchange interaction with the Mn spin.

In the calculation of the rates we perform an additional approximation: we only consider spin-flip terms in equation (4.36) and we do exclude spin-conserving terms. The results for transition rates from the state n with dominant $(-1, -\frac{5}{2})$ to three possible final states with dominant components $(+2, -\frac{5}{2})$, $(-2, -\frac{1}{2})$ and $(+1, -\frac{3}{2})$ as a function of the spin-flip Mn hole exchange $J_{h\perp}$, are shown in figure (4.4). The transition to the $(+2, -\frac{5}{2})$, which only involves the irreversible spin flip of the hole via a phonon emission is the dominant process and has a lifetime of 30 ns. The transition to the $(+1, -\frac{3}{2})$ state requires both the hole spin flip and the Mn-hole spin flip and it is three orders of magnitude less efficient.

Thus, these calculations indicate that the most likely mechanism for Mn spin orientation in the presence of an exciton combines a rapid bright-to dark conversion, produced by phonon induced hole spin flip, and a dark to ground transition, enabled by Mn-carrier spin exchange and radiative recombination.

4.4 Conclusion

In section (4.2) we studied the dissipative dynamics of the Mn spin due to its coupling to phonons, both with and without excitons in the dot. The Mn spin-phonon coupling arises from the time dependent stochastic fluctuations of the crystal field and thereby of the single ion magnetic anisotropy, induced by the phonon field. Whereas the Mn spin relaxation is accelerated by 2 or 3 orders of magnitude in the presence of the exciton, the efficiency of this mechanism is too low to account for the optical orientation of the Mn spin reported experimentally(6, 10, 11). The small Mn spin-phonon coupling comes from the small magnetic anisotropy of Mn as a substituional impurity in CdTe.

In section (4.3) we described the interaction between the hole spin and the phonons in non-magnetic dots. Using the simple analytical model for the holes presented in section (3.1) we obtained analytical formulas for the hole spin relaxation. We find that hole spin lifetime can be in the range of 30 ns for a hole spin splitting as large as that provided by the hole-Mn coupling. Thus, we expect that bright excitons will relax into dark excitons via hole-spin relaxation. This provides a microscopic mechanism to the scenario for Mn spin relaxation proposed by Cywinski (14): bright excitons relax into dark excitons, via carrier spin relaxation, and the joint process of Mn-carrier spin exchange couples the dark excitons to the bright excitons, resulting in PL from dark states which implies Mn spin relaxation in a time scale of a few nanoseconds. we will see in the next chapter, how these calculated spin flip rates can explain the observed spin dynamics in Mn doped quantum dots driven by a resonant laser field.

5

Laser driven spin dynamics

Contents

Experiments show that a Mn spin in a quantum dot can be optically oriented using resonant laser excitation. In this chapter we discuss theoretically the optical Mn spin orientation mechanism in a single Mn doped CdTe quantum dot employing standard master equation and the spin-flip rates calculated in chapter 4. In this chapter we only consider the time evolution of the diagonal part of the density matrix (population), the coherence evolution will be discussed in the next chapter.

5.1 Scattering mechanisms and master equation

The spin dynamics of a single Mn atom in a laser driven quantum dot is described in terms of the 24 exciton states Ψ_n and the 6 ground states ϕ_m. In the previous chapter we have calculated the scattering rates of these states. They can be summarized as follows:

1. Transitions from the Ψ_n to the ϕ_m, via photon emission (eq. (3.69)). In the case of bright excitons, this process is the quickest of all, with a typical lifetime of 0.3 ns. In the case of dark excitons the lifetime depends on the bright/dark mixing, which is both level and dot dependent. Dark lifetime ranges from twice the one of bright excitons to 1000 times larger, ie, between 1 and 300 nanoseconds. In any event, dark recombination involves a Mn spin flip.

2. Transitions between different ϕ_m states, due to Mn spin phonon coupling (eq. (4.18)). The lifetimes of these transitions are, at least, 1ms (see right panel of figure 4.1).

3. Transitions between different exciton states Ψ_n that flip the spin of the Mn only, due to Mn-phonon coupling (equation (4.24)). The lifetimes of these transitions are, at least, 0.1ms (see left panel figure 4.1).

4. Transitions between exciton states due to hole-phonon coupling (equation (4.35)). The bright to dark transition is the quickest process with a lifetime of about 30ns (see figure 4.4). Bright to bright transitions, combining hole-phonon and Mn-carrier interactions, have lifetimes in the 10 μs range.

In addition to these dissipative scattering processes, we have to consider driving effect of the laser field, described in the semiclassical approximation. All things considered, we arrive to a master equation that describes the evolution of the occupations p_N, where $N = (n, m)$ includes states both with and without exciton in the dot. The master equation reads:

$$\frac{dp_N}{dt} = \sum_{N'} \Gamma_{N' \to N} p_{N'} - \sum_{N'} \Gamma_{N \to N'} p_N \tag{5.1}$$

Eq. (5.1) is a system of 36 coupled differential equations that we solve by numerical iteration, starting from a thermal distribution for the initial occupation p_N. Since the temperature is larger than the energy splitting in the ground state, but much smaller than the band gap, at $t = 0$ we have the six ground states with similar occupation $P_m \simeq 1/6$, $P_n \simeq 0$. As a result, the average magnetization, defined as:

$$\langle M_z \rangle = \sum_m p_m \langle \phi_m | M_z | \phi_m \rangle \tag{5.2}$$

is zero, at zero magnetic field, as expected.

5.2 Optical Mn spin orientation

Under the action of the laser, the exciton states become populated and, under the adequate pumping conditions, the average Mn magnetization $\langle M_z \rangle$ acquires a non-zero value. This transfer of angular momentum, known as optical Mn spin orientation has been observed experimentally (10) and predicted theoretically(12). It results from a decrease of the Mn spin lifetime in the presence of the exciton in the dot. In that circumstance, the laser transfers population from the M_z state to the X, M_z state. The enhanced relaxation transfers population from X, M_z to X, M_z' and the recombination to M_z' state. Thus, if the laser is resonant with a single M_z to X, M_z transition, the M_z

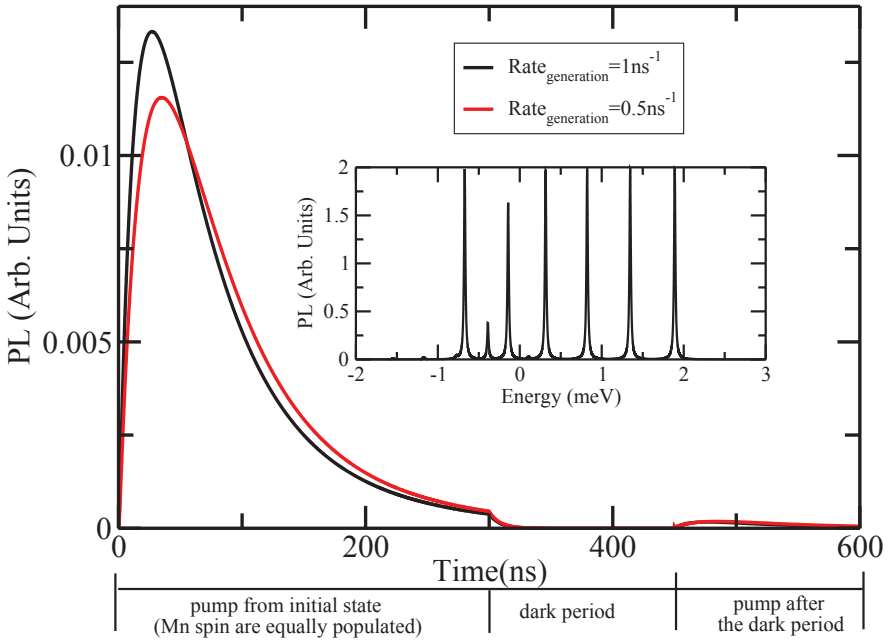

Figure 5.1: Simulation of PL intensity from state ($X = +1, M_z = -\frac{5}{2}$) under the influence of a driving laser pumping the system resonantly from optical ground state $M_z = -\frac{5}{2}$ to the excited state ($X = -1$, $M_z = -\frac{5}{2}$) for two laser intensities. The inset is the PL spectrum assuming all the states are equally populated. In the calculation, the quantum dot anisotropy (L_x=5nm and L_y=6nm) controls the LH-HH mixing. The other parameters are discussed in the text.

state is depleted, which results in a decrease of the PL coming both from the X, M_z and the $-X, M_z$ transitions.

In figure (5.1) we show the result of our simulations for a dot at thermal equilibrium ($k_B T = 4$K) at $t = 0$ which is pumped with a laser pulse resonant with the $X = -1, M_z = -\frac{5}{2}$ transition, which is the high energy one, since the hole is parallel to Mn spin. The laser pulse has a duration of 300 nanoseconds, so that the spectral broadening is negligible. In the upper panel we plot the PL coming from the counter-polarized transition, $X = +1, M_z = -\frac{5}{2}$, which has lower energy and can be detected without interference with the laser, for two different pumping power intensity. It is apparent that after a rise of the PL in a time scale of tens of nanoseconds , corresponding the spin relaxation of the exciton spin from $X = -1$ to $X = +1$, probably mediated by exciton-Mn exchange, the PL signal is depleted. The origin of the depletion is seen in

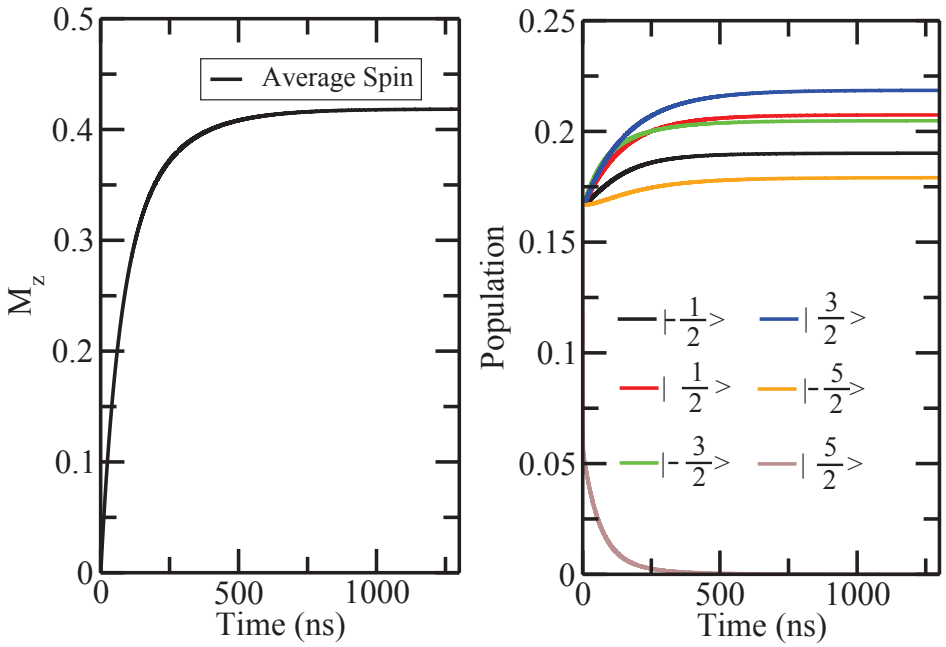

Figure 5.2: Left panel: average magnetization and right panel: occupation of the different spin states under optical pumping of the state ($X = -1$, $M_z = -\frac{5}{2}$). Parameters are the same as for the calculation presented in figure (5.1).

figure (5.2). The occupation of the $M_z = -\frac{5}{2}$ spin state in the ground reduced down to zero, in benefit of the other Mn spin states.

Accordingly, the average magnetization becomes finite. Thus, net angular momentum is transferred from the laser to the Mn spin. The transfer takes place through Mn spin relaxation enabled in the presence of the exciton. As discussed above, the most efficient mechanism combines hole-spin relaxation due to phonons combined with dark-bright mixing, which involves a Mn spin flip.

Interestingly, the fact that in the steady state several Mn spin states are occupied, including the higher energy ones, is compatible with a picture in which the Mn spin is precessing. Thus, a steady supply of spin-polarized excitons in the dot would result in the precession of the Mn spin, a scenario similar to that of current drive spin-torque oscillators(86). Further work is necessary to confirm this scenario.

The efficiency of the process increases with the laser power, as shown in figure (5.3). We define the spin orientation time τ_{pump} as the time at which the PL of the counter

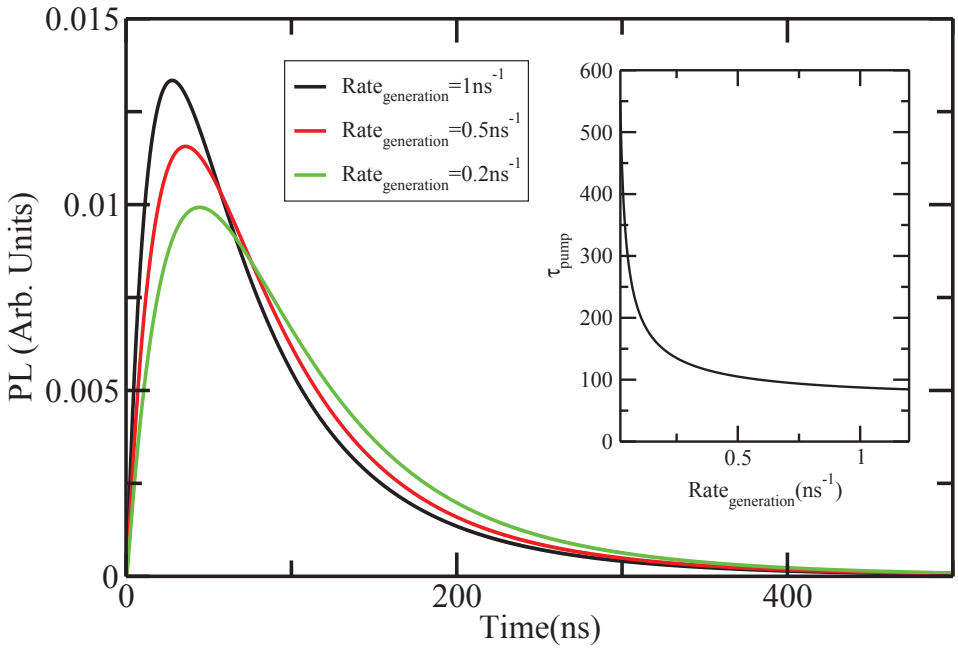

Figure 5.3: Evolution of Mn spin orientation efficiency as a function of the laser power. The pumping is detected in the PL intensity from state ($X = +1$,$M_z = -\frac{5}{2}$) under the influence of a driving laser pumping the system from optical ground state $M_z = -\frac{5}{2}$ to the excited state ($X = -1$, $M_z = -\frac{5}{2}$). The inset presents the laser power dependence of τ_{pump}, from where we can see that the efficiency of the pumping gets higher with the increasing of the laser power.

polarized transition is half the maximum. We can see that, as expected, τ_{pump} is a decreasing function of the laser power. A pumping time $\tau_{pump} \simeq$90ns is obtained with a generation rate of about 1ns^{-1}. The amplitude of the valence band mixing, controlled by the anisotropy of the confinement potential or the in-plane strain distribution, is the main quantum dot parameter controlling the efficiency of the optical pumping. As presented in figure (5.4), decreasing the quantum dot anisotropy, i.e., decreasing the LH-HH mixing parameter $J_{h\perp}$, produces a rapid increase of τ_{pump} (inset of figure (5.4). This is a direct consequence of the reduction of the phonon induced hole spin flip rates.

Quantity	Symbol	Value
Hole-Mn exchange	j_h	0.31 meV
Electron-Mn exchange	j_e	-0.09 meV
Electron-Hole	j_{eh}	-0.73 meV
Uniaxial Anisotropy	D_0	10 μeV
In plane Anisotropy	E	0
Quantum dot width	L_y	6nm
Quantum dot width	L_x	5nm
Quantum dot height	L_z	3nm

Table 5.1: Parameters used in the simulation of the resonant PL observed in the time resolved optical pumping experiments.

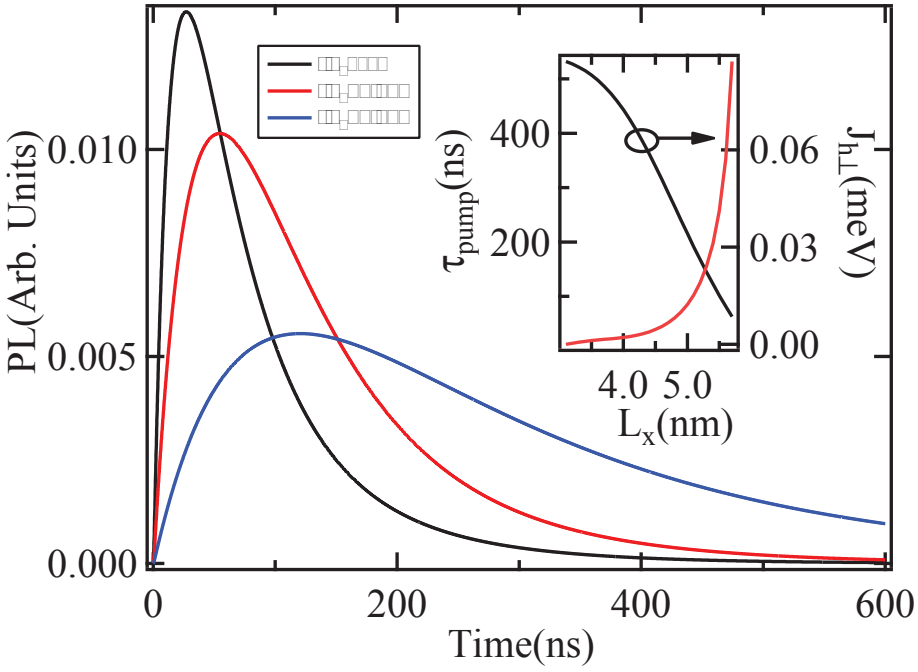

Figure 5.4: Evolution of Mn spin orientation efficiency as a function of the valence band mixing controlled by the anisotropy of the confinement potentiel (L_y=13nm, variable L_x). The pumping is detected in the PL intensity from state ($X = +1, M_z = -\frac{5}{2}$) under the influence of a driving laser pumping the system from optical ground state $M_z = -\frac{5}{2}$ to the excited state ($X = -1$, $M_z = -\frac{5}{2}$). The inset shows the evolution of τ_{pump} with L_x and $J_{h\perp}$. The exciton generation rate is fixed at 1 ns^{-1}.

5.3 Conclusions

We have studied the spin dynamics of a single Mn atom in a CdTe quantum dot excited by a laser that drives the transition between the 6 optical ground states, associated to the $2S+1$ states of the Mn spin $S=\frac{5}{2}$, and the 24 single exciton states, corresponding to $X=\pm 1,\pm 2$ states interacting with the Mn spin. The main goal was to have a microscopic theory for the Mn spin relaxation mechanisms that makes it possible to produce laser induced Mn spin orientation in a time scale of less than 100 ns. (6, 10, 11) For that matter, we need to describe how the Mn and the quantum dot exciton affect each other. In this section 5.1 we presented the master equation that governs the dynamics of the 30 states of the dot, we solve it numerically and we model the optical Mn spin orientation reported experimentally.

Our main conclusions are:

- Mn spin-phonon spin relaxation is presumably too weak to account for Mn spin dynamics in the presence of the exciton
- The Mn spin orientation is possible in a time scale of one hundred nanoseconds via a combination of phonon-induced hole spin relaxation and the subsequent recombination of the dark exciton enabled by spin-flip exchange of the Mn and the carrier
- The critical property that governs the hole-Mn exchange and the hole spin relaxation is the mixing between light and heavy holes, which depends both on the shape of the dot and on strain.
- Our microscopic model permits to account for the optically induced Mn spin orientation. However, for a quantitative agreement, a strong hole localization has to considered. This strong localization is also consistent with the large value of J_{h-Mn} observed experimentally.

6

Coherent dynamics of a Mn spin

Contents

We want to estimate in this chapter how we could use optical or microwave excitation of a quantum dot to study the coherent dynamics of the spin state of a Mn atom. After a short description of recent experiments showing that the energy of the spin state of a Mn atom can be tuned using the optical Stark effect we will show the

influence of the Mn fine and hyperfine structure on a direct coherent optical control exploiting time resolved optical Stark effect. We will also demonstrate the importance of the coherent dynamics of the coupled electronic and nuclear Mn spins on the optical pumping of the Mn atom. We will then show how Mn spin switching at zero magnetic field can be performed via optically induced electron-nuclei flip-flops. Finally we will show how direct microwave coherent control of the Mn spin could be optically detected.

6.1 Experimental evidence of optical Stark effect on an individual Mn spin.

Each spin state of the Mn can be addressed with a control laser circularly polarized ($\sigma\pm$) and tuned on resonance with an emission line of the exciton-Mn (XMn) complex (87). The strong coupling between the control laser and the excited two level system can induce an energy shift and a splitting of the electronic states. The splitting induced by the control laser tuned to the high energy line of XMn in $\sigma+$ polarization can be detected in $\sigma-$ polarization on the low energy line of XMn as both lines correspond to the same Mn spin. This is the equivalent of the Autler-Townes splitting observed in atomic physics (88).

The effect of the control laser field is to mix the states with a Mn spin component M_z=+5/2 in the presence (XMn) or absence (Mn alone) of the exciton. At the resonance, the unperturbed states $|Mn\rangle \otimes |n\rangle$ and $|XMn\rangle \otimes |n-1\rangle$ can be dressed into pairs of hybrid matter-field states $|I,n\rangle$ and $|II,n\rangle$ where $|n\rangle$ is a n-photons state of the control laser. These states can be written as (89):

$$|I,n\rangle = c|Mn\rangle \otimes |n\rangle - s|XMn\rangle \otimes |n-1\rangle$$
$$|II,n\rangle = s|Mn\rangle \otimes |n\rangle + c|XMn\rangle \otimes |n-1\rangle$$

with corresponding energies $E_\pm = \frac{\hbar}{2}(\omega_c + \omega_0) \pm \frac{\hbar}{2}\Omega'_r$. Here, $c = \sqrt{\frac{1}{2}(1 - \frac{\delta}{\Omega'})}$ and $s = \sqrt{\frac{1}{2}(1 + \frac{\delta}{\Omega'})}$. $\delta = \omega_c - \omega_0$ is the laser detuning with ω_0 the resonance frequency of the unperturbed transition and ω_c the frequency of the control laser. $\hbar\Omega'_r = \hbar\sqrt{\Omega_r^2 + \delta^2}$ defines the energy splitting of the dressed states where $\Omega_r = \mathcal{P}\mathcal{E}/\hbar$ is the Rabi frequency with $\mathcal{P}$ the dipolar moment of the quantum dot transition and $\mathcal{E}$ the amplitude of the electric field of the control laser. A power dependent Autler-Townes type splitting is then expected for all transitions that share such an optically dressed state (88, 90).

Experimental data corresponding to a control laser tuned on $|+1,+5/2\rangle$ and the observation of an Autler-Townes splitting in the PL of the state $|-1,+5/2\rangle$ are presented in Fig. 6.1. Particular care is given to the effect of the detuning of the control laser from the XMn resonance (Fig. 6.1(c) and 6.1(d)) and its intensity (Fig. 6.1(e) and 6.1(f)). At large laser detuning, the optically active transitions asymptotically approach the

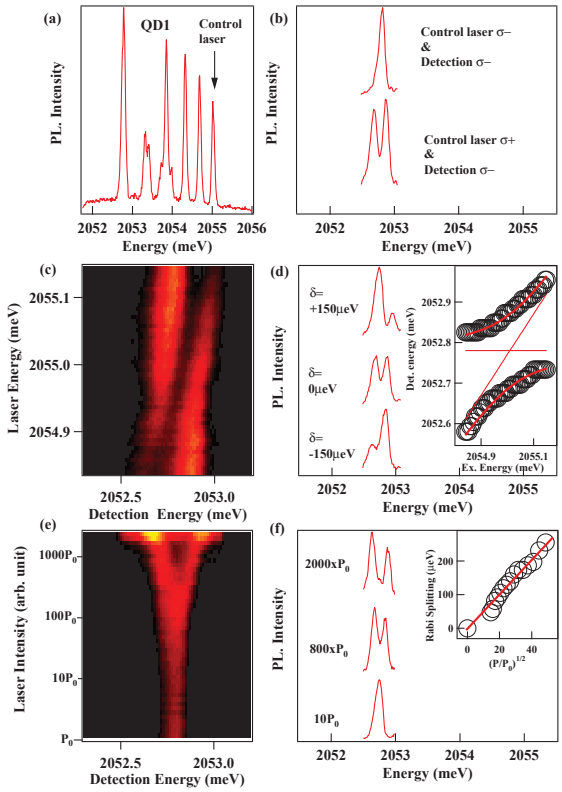

Figure 6.1: Autler-Townes splitting of the emission of $|-1,+5/2\rangle$ in a Mn-doped quantum dot resonantly excited on $|+1,+5/2\rangle$. (a) shows the non-resonant photoluminescence of the quantum dot. The intensity map (c) shows the excitation energy dependence of the Rabi splitting. The corresponding emission line-shape is presented in (d). The inset shows the spectral position of the Autler-Townes doublet as a function of the pump detuning. The fit is obtained with a Rabi energy $\hbar\Omega_r = 180\mu eV$. The straight lines corresponds to the uncoupled exciton and laser energy. The excitation intensity dependence of the Autler-Townes doublet is presented in the intensity map (e). The corresponding emission line-shape are presented in (f). The inset shows the evolution of the Rabi splitting as a function of the square-root of the pump intensity. A linear increase is observed. (b) presents the circular polarization dependence of the Rabi splitting obtained under resonant excitation. Extracted from reference (87).

original excitonic transitions where the remaining energy offset is the **optical Stark shift**. At the resonance, an anti-crossing is observed showing that the strong coupling between the laser field and the exciton creates hybrid light-matter states. As presented in the inset of Fig. 6.1(d), a good agreement with the simple dressed atom model is obtained with a Rabi energy of $\hbar\Omega_r$=180μeV. On resonance, the emission from the $|-1,+5/2\rangle$ state splits into a doublet when the power of the control laser is increased, as expected from the Autler-Townes model. The splitting is plotted as a function of the square root of the control laser intensity in Fig. 6.1(f), showing that the splitting linearly depends on the laser field strength. The laser induced energy shift can be easily larger than the magnetic anisotropy of an isolated Mn spin created by the strain in the quantum dot plane (≈40μeV) (10, 55, 56). As we will see in the following, the laser induced shift of the Mn spin could be used for a fast optical coherent manipulation and the optical tuning of the fine structure may lead to a control of the coherent dynamics of the isolated Mn spin.

6.2 Coherent control of a Mn spin using time resolved optical Stark effect.

The model developed in this part describes the coherent time evolution of the coupled electronic and nuclear spins of the Mn spin in a transverse magnetic field under pulsed laser coupling to an exciton state. We want to estimate how the pulsed excitation of the quantum dot could be used to coherently control the spin of an individual Mn atom exploiting time resolved optical Stark effect.

6.2.1 Master equation.

As presented in Fig. 6.2, we consider the coherent evolution of coupled electronic and nuclear spins in a transverse magnetic field laser coupled to a single exciton-Mn state. This can be achieved under resonant optical excitation of one transition of X-Mn with picosecond pulses(≈ 10 ps).

We compute the time evolution of ϱ, the 42x42 density matrix describing the population and the coherence of the 36 nuclear (I_z) and Mn spins (M_z) in the ground state and 6 exciton sates (+1,M_z=5/2,I_z) in the excited state.

The general form of the master equation which governs the Mn evolution ϱ is given by:

$$\frac{\partial \varrho}{\partial t} = -i/\hbar[H, \varrho] + L\varrho \tag{6.1}$$

The first term represents the Hamiltonian evolution and the second term describes all the coupling with the environment. $L\varrho$ separates into one contribution for each

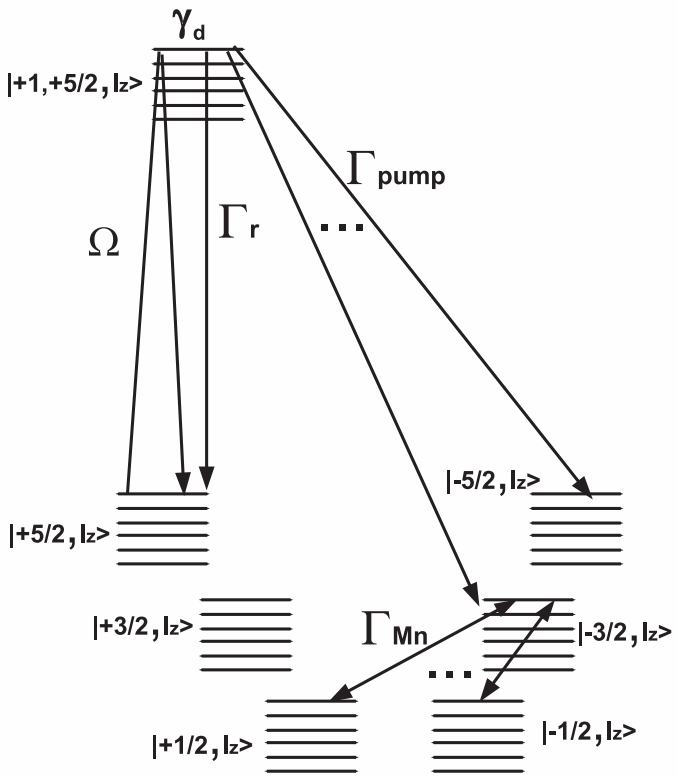

Figure 6.2: Scheme of the energy levels and transitions rates involved in the resonant excitation model. Ω is the coupling with the laser, γ_d is a pure dephasing of the exciton, Γ_{Mn} is the relaxation rate of the Mn, Γ_r is the optical recombination rate of the exciton. A relaxation rate of the exciton-Mn complex Γ_{pump} can be introduced for an effective description of the optical pumping effect.

coupling or decay channel (91):

1- The coherent coupling between two levels induced by a resonant laser $i \leftrightarrow j$ leads to Rabi oscillation between the populations ϱ_{ii} and ϱ_{jj} and coherence of these levels $\varrho_{ij} = \varrho_{ji}^*$. This reversible coupling is described by the operator:

$$L_{coh,i\leftrightarrow j}\varrho = i\frac{\Omega_{ij}}{2}(|j\rangle\langle i|\varrho + |i\rangle\langle j|\varrho - \varrho|j\rangle\langle i| - \varrho|i\rangle\langle j|) \tag{6.2}$$

where $\Omega_{ij} = \mathcal{P}_{ij}\mathcal{E}/\hbar$ is the Rabi frequency with $\mathcal{P}_{ij}$ the dipolar moment of the quantum dot transition and $\mathcal{E}$ the amplitude of the electric field of the control laser.

2- The incoherent population decay from level j to level i in an irreversible process associated with a coupling to a reservoir. It results in a one way exponential decay that can be described by the operator:

$$L_{inc,j\rightarrow i}\varrho = \frac{\Gamma_{j\rightarrow i}}{2}(2|i\rangle\langle j|\varrho|j\rangle\langle i| - \varrho|j\rangle\langle j| - |j\rangle\langle j|\varrho) \tag{6.3}$$

where $\Gamma_{j\rightarrow i}$ is the incoherent relaxation rate from level j to level i. This form operator can describe the radiative decay of the exciton (irreversible coupling to the photon modes) or the relaxation of the Mn spin (irreversible coupling to the phonon modes)

3- A pure dephasing (*i.e.* not related to an exchange of energy with a reservoir) can also be introduced and is described by an operator of the form:

$$L_{deph,jj}\varrho = \frac{\gamma_{jj}}{2}(2|j\rangle\langle j|\varrho|j\rangle\langle j| - \varrho|j\rangle\langle j| - |j\rangle\langle j|\varrho) \tag{6.4}$$

where γ_{jj} is a pure dephasing rate.

6.2.2 Hamiltonian

The Hamiltonian of the coupled electronic and nuclear Mn spins in the ground state is given in equation 3.79 of chapter 3. We consider only one exciton state $|+1\rangle$ laser coupled with one state of the Mn $|M_z = +5/2, I_z\rangle$ with a Rabi frequency Ω. This approximation is justified in strongly confined CdTe/ZnTe quantum dots resonantly excited by a narrow band laser. The exciton can relax to the ground state by conserving the Mn spin with a rate Γ_r. The exciton presents a pure dephasing γ_d. At low transverse magnetic field, the hole Mn exchange interaction is much larger than the Mn Zeeman energy and we can neglect its influence on the exciton-Mn state. Additional relaxation terms could be added in the excited state (exciton-Mn) to take into account the Mn spin relaxation within the exciton-Mn complex.

The relaxation of the Mn spins in the ground state are described by a relaxation rate Γ_{Mn} coupling one by one the different spin states M_z. We do not consider any

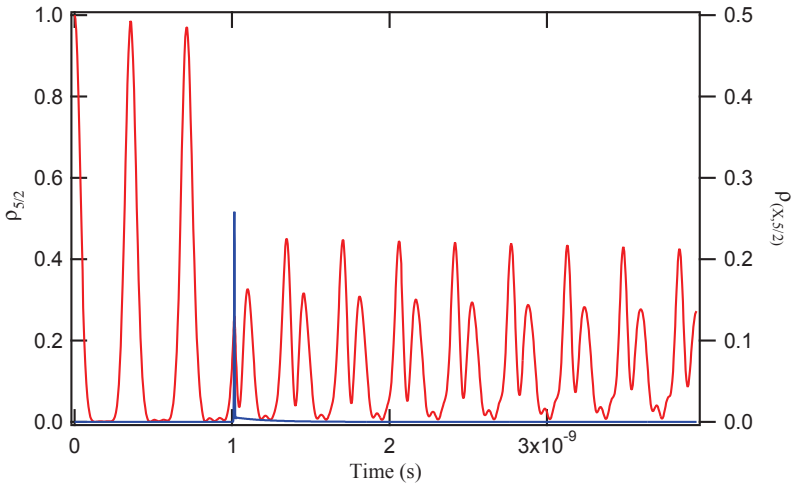

Figure 6.3: Time evolution of $\varrho_{5/2}$ obtained with for a pure electronic spin M=5/2 (A=0 μeV, a=0 μeV, D_0=0 μeV) under a transverse magnetic field $B_x = 0.1T$ and with $\Gamma_r = 200ps^{-1}, \Gamma_{Mn} = 20ns^{-1}, \gamma_d = 100ps^{-1}$, $\varrho_{5/2}(0) = 1$. A 2π Gaussian pulse with a width of $\tau = 10ps$ is sent at $t_1 = 1ns$ (the blue line presents the time evolution of the $|X, 5/2\rangle$ population displayed on the right axis).

spin relaxation for the nuclear spin I which is considered to be frozen in the timescale of the data presented here.

6.2.3 Time resolved optical Stark effect on a Mn spin.

This simplified model can be used to model pulsed optical coherent control experiments on a Mn spin. These experiments are difficult to implement but theoretically interesting.

A rotation of the Mn spin can be performed with picosecond optical pulses which will move the system outside of the Mn spin subspace during the rotation in the transverse magnetic field. field. This introduces a phase shift between each Mn spin component. Such phase shifts can be seen as a rotation of the Mn spin. Any direction of the Mn spin could be targeted with a carefully designed pulse sequence (amplitude and delay). For instance, in a simple three level model, a 2π pulse induces a π rotation about the z axis. This coherent manipulation is illustrated in Fig. 6.3 in the case of a pure electronic spin M=5/2 (no coupling to the nuclear spin and no crystal field).

For a real Mn atom in a semiconductor matrix, the hyperfine coupling with the nuclear spin and the crystal field as to be taken into account. The precession of a Mn spin in a transverse magnetic field $B_x = 0.25T$ for different values of strained

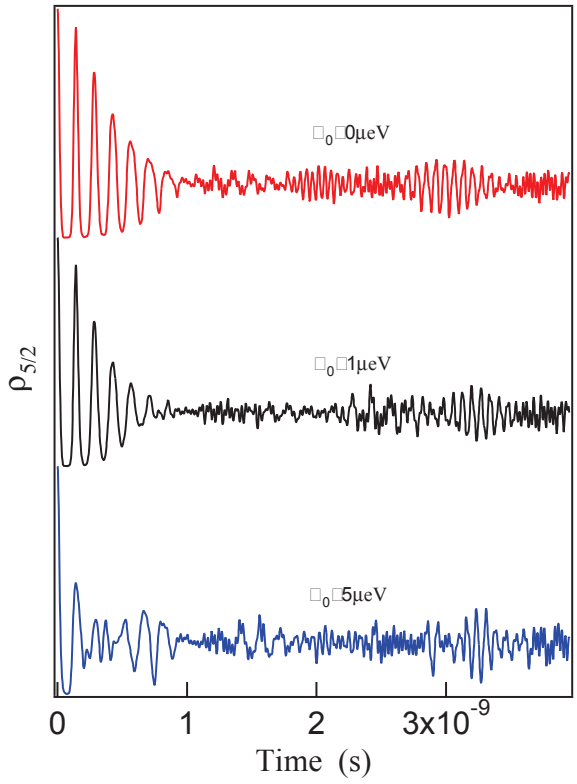

Figure 6.4: Time evolution of $\varrho_{5/2}$ obtained with A=0.68 μeV, a=0.32 μeV and variable D_0 under a transverse magnetic field $B_x = 0.25T$ with $\Gamma_{Mn} = 20ns^{-1}$ and $\varrho_{5/2}(0) = 1$.

induced magnetic anisotropy D_0 is presented in Fig. 6.4. After $1ns$, the precession of the electronic Mn spin is blurred by the hyperfine coupling and influence of crystal field. In a transverse field, a coherent control of the Mn can only be performed in the first $1ns$ and in a weakly strained quantum dot resulting in a D_0 typically lower than 1 μeV.

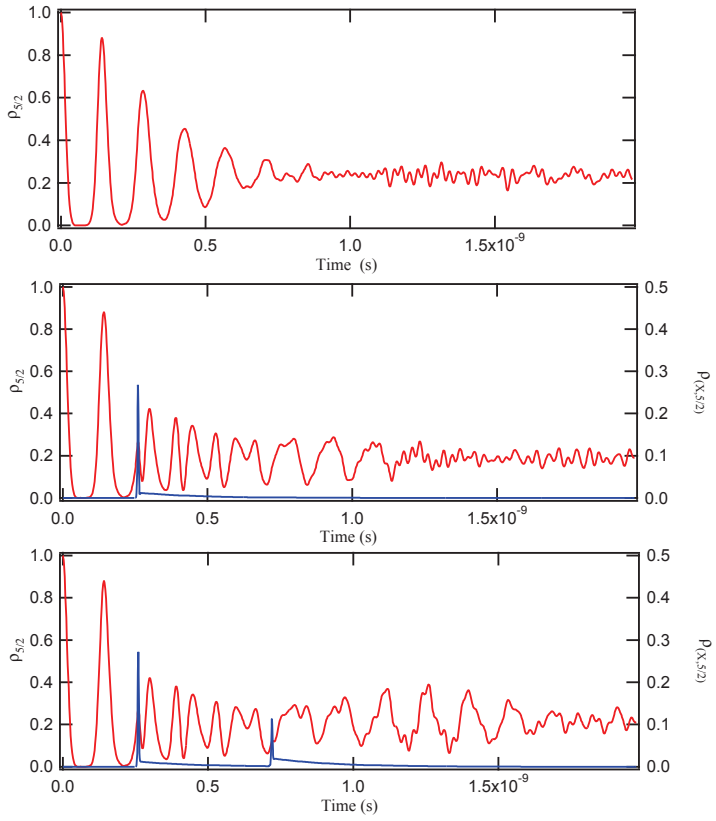

Figure 6.5: Time evolution of $\varrho_{5/2}$ in a weakly strained Mn-doped quantum dot (A=0.68 μeV, a=0.32 μeV and $D_0 = 1\mu$eV) under a transverse magnetic field $B_x = 0.25T$, with $\Gamma_{Mn} = 20ns^{-1}$ and $\varrho_{5/2}(0) = 1$. 0, 1 or 2 2π Gaussian pulses with a width of $\tau = 10ps$ are sent at t_1= 260 ps and t_2=720 ps. The calculations are performed with $\Gamma_r = 200ps^{-1}$ and a pure dephasing for the exciton $\gamma_d = 100ps^{-1}$

Such coherent control is presented in Fig. 6.5 for D_0= 1 μeV and sequences of one or two resonant picosecond pulses. This model shows that a phase shift can be induced in the precessing Mn spin during the first ns.

In conclusion, in a transverse magnetic field, the optical Stark effect could be used to act on the Mn spin only during the first ns of its precession. In addition, this optical

coherent control scheme works well only for a free precessing spin. D_0 in highly strained quantum dots is a problem.

6.3 Influence of the Mn spin coherent dynamics on the optical pumping.

The same model of Mn spin coherent dynamics under resonant optical excitation can be used to analyze the origin of the residual fluorescence signal observed under optical pumping conditions: Experimentally, the optical pumping efficiency nether reach 100%, a resonant fluorescence signal can always be observed at zero magnetic field. This intensity of resonant fluorescence decreases under a small magnetic applied along the quantum dot growth axis (11)

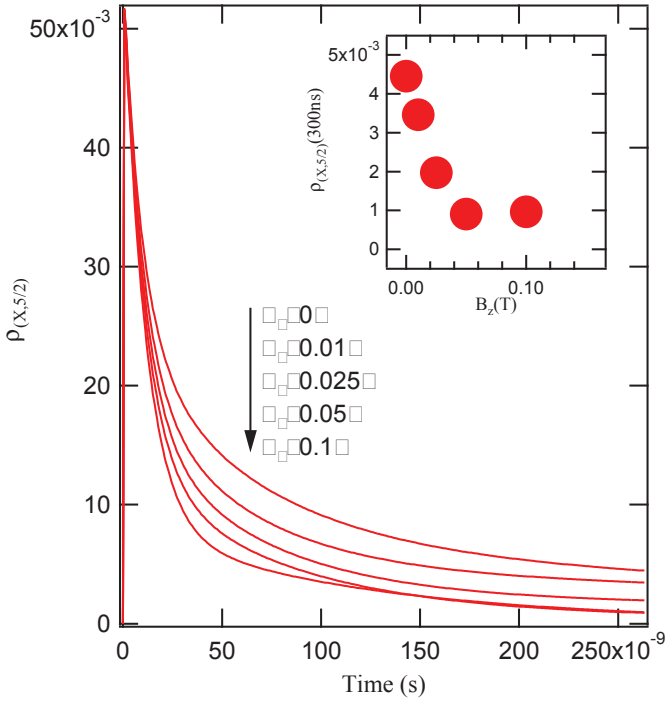

Figure 6.6: Magnetic field dependence of the optical pumping transient calculated with D_0=4μeV, a=0.32μeV A=0.68μeV, E=0μeV, T_{pump}=20ns, T_g=0.5ns T_{Mn}=10μs and T_r=0.25ns. The inset shows the amplitude of $\rho_{X,5/2}$ at 300ns (steady state) as a function of a magnetic field applied along the quantum dot growth axis z.

An effective spin relaxation rate ($\Gamma_{pump} = 1/T_{pump}$) for the exciton-Mn complex is

introduced in the model presented in Fig.6.2. It allows a transfer of population from the state $|+1,+5/2,I_z\rangle$ to any other spin state of the Mn $|M_z\rangle$ with I_z unchanged. This is a simplified effective way to include the exciton-Mn spin relaxation channels we discussed in the previous chapters. Here, we do not take into account the details of these relaxation channels. These spin flips rates are responsible for an optical pumping of the Mn spin state under resonant optical excitation. However, as confirmed by the calculated PL transients presented in Fig. 6.6, the coherent coupling with the nuclear spin prevents the optical pumping efficiency to reach 100% (10). This is particularly pronounced for a weak value of D_0. As observed experimentally, this effect can be suppressed by a weak magnetic field applied along the quantum dot growth axis. This evolution is qualitatively reproduced by our simple model (Inset of Fig. 6.6). When the Zeeman energy exceeds the hyperfine coupling and the tetragonal crystal field energies (magnetic field larger than 50 mT), the coherent precession of M_z in its hyperfine field is blocked and the efficiency of optical pumping is maximum.

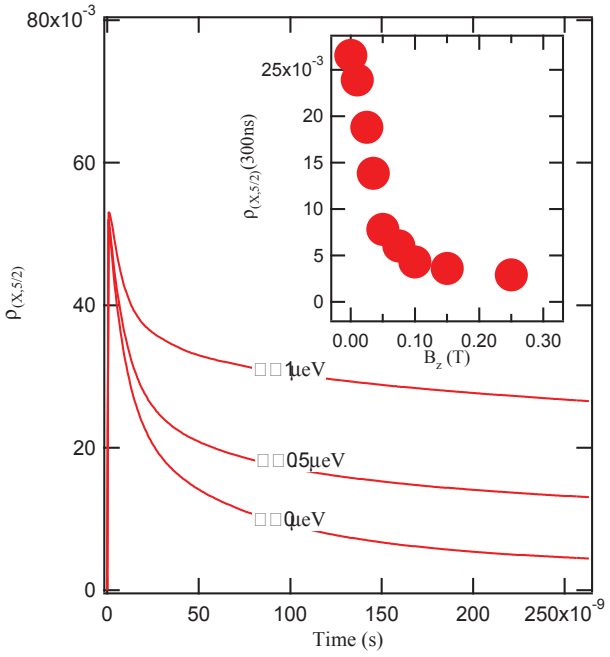

Figure 6.7: Optical pumping transients calculated for different values of E with D_0=5μeV, a=0.32μeV A=0.68μeV, T_{pump}=20ns, T_g=0.5ns and T_r=0.25ns. The inset shows the amplitude of $\rho_{X,5/2}$ at 300ns (steady state) as a function of magnetic field applied on a quantum dot with $E = 1\mu$eV along its growth axis z. $\rho_{X,5/2}(300ns)$ is proportional to the steady state PL.

An anisotropy in the strain distribution at the Mn spin location, resulting in a term $E(M_x^2 - M_y^2)$ in Mn fine structure, can also be responsible for a poor optical pumping efficiency. This is illustrated in Fig. 6.7 where the influence of E on the optical pumping transient are presented. Even a weak anisotropy of the strain ($E = 0.5\mu$eV compared to the isotropic term D_0=4μeV) significantly reduces the efficiency of the optical pumping. In the presence of this strain anisotropy, a magnetic field along z has a strong influence on the optical pumping transient. The pumping is almost fully restored and the resonance fluorescence almost suppressed within the first 100mT, in good agreement with experimental data (11). This model confirms that the presence of anisotropic strain at the Mn location is responsible for the magnetic field dependence of the resonance fluorescence signal and the poor efficiency of the resonant optical pumping in most of the Mn doped quantum dots.

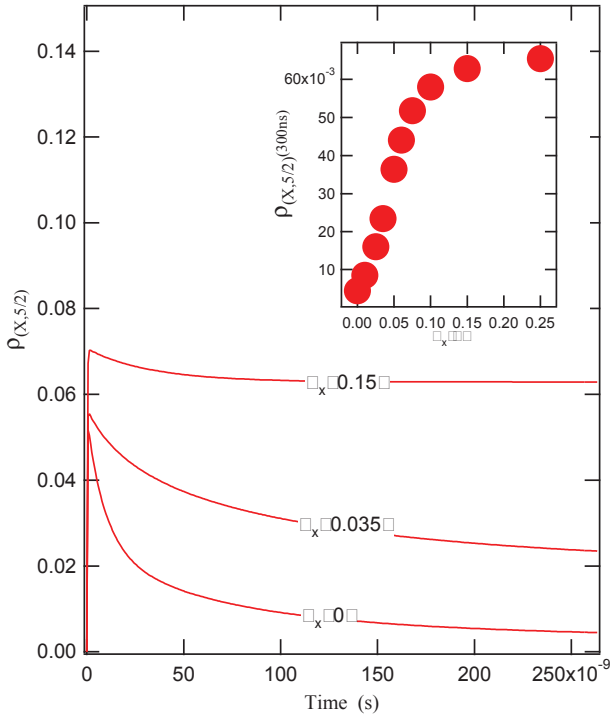

Figure 6.8: Optical pumping transients calculated for different values of transverse magnetic field B$_x$ with D_0=4μeV, a=0.32μeV A=0.68μeV, E=0μeV T_{pump}=20ns, T_g=0.5ns and T_r=0.25ns. The inset shows the amplitude of $\rho_{X,5/2}$ at 300ns (steady state) as a function of magnetic field.

The fine and hyperfine structure of the Mn also control the transverse magnetic field dependence of the optical pumping. In this case, the determinant parameter is

the magnetic anisotropy D_0 which blocks the precession of the Mn spin at low magnetic field (Fig. 6.8). The larger the value of D_0, the larger the field needed to suppress the optical pumping.

6.4 Optically controlled electron-nuclei coupling for Mn spin switching.

Alternatively, the hyperfine coupling could be exploited to perform an optical manipulation of the Mn spin at zero external magnetic field. We want to show in this part how the optical Stark shift induced by a resonant single mode laser can be used to control the coupling between the electronic and nuclear spin of an Mn atom. This controlled interaction could be exploited for an all optical detection of the Mn fine structure and for a control of the dynamics of the electronic Mn spin.

6.4.1 Mn energy levels in the strong coupling regime.

We want first to analyze the Mn fine structure in the optical strong coupling regime. We start again from the Hamiltonian of the coupled electronic and nuclear Mn spins given in equation 3.79 of chapter 3. It is mainly controlled by A, the hyperfine coupling with the nuclear spin, and D_0 the strain induced magnetic anisotropy.

Lets us consider, as in the experiments presented previously, that the Mn spin is coherently coupled to a single excited exciton-Mn level $(+1, M_z = 5/2, I_z)$ with a resonant laser field. This is a good approximation if the Rabi splitting induced by resonant laser is much weaker than the splitting between the lines of the X-Mn complex. This can be verified in most of the Mn doped quantum dots as the laser energy shift we need to influence the Mn spin fine structure is typically lower than 50μeV.

The Hamiltonian of the coupled light matter systems reads:

$$\mathcal{H}_{lm} = \mathcal{H}_{Mn} + \hbar\omega_0 |XMn\rangle\langle XMn| + \hbar\omega_l a a^\dagger + \hbar\Omega_r (a d^\dagger + a^\dagger d) \tag{6.5}$$

where a (resp. $a^\dagger$) is the annihilation (resp. creation) operator of a photon in the mode at energy ω_l. ω_0 is the energy of the optical transition and d (resp. $d^\dagger$) is the annihilation (resp. creation) operator of an exciton of energy ω_0. $\Omega_r = \sqrt{n}g$ is the Raby frequency, with g the electrical dipole matrix element describing the coupling between the dipole of the quantum dot transition and the mode ω_l of the electric field and n the number of photons in the mode. The optically dressed states are found diagonalizing the total Hamiltonian. The result of the diagonalization for different values of $\hbar\Omega_r$ is presented in Fig. 6.9. As expected, optically dressed states are created for M_z=5/2 and all the spin states of the nuclei I_z. As observed experimentally, the laser induced

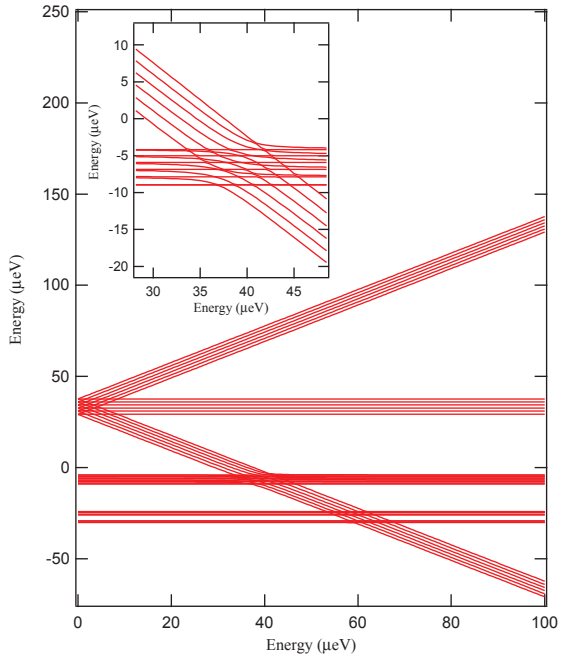

Figure 6.9: Fine structure of the Mn spin in a strained quantum dot as a function of the Raby energy $\hbar\Omega_R$. The enlarged view in the inset shows anti-crossing between the different Mn spin states $M_z = 5/2$ and $M_z = 3/2$. Calculated with $A = 0.68$ μeV, $D_0 = 10$ μeV, $a = 0.32$ μeV.

splitting can be much larger than the fine structure produced by D_0. Consequently, the degeneracy between M_z=+5/2 and M_z=+3/2 can be optically restored. The strong coupling with the laser field could be used to tune the energy of any other spin state of the Mn and control there degeneracy (87).

When the light induced energy shift compensate the strain induced magnetic anisotropy, two consecutive spin states of the Mn are coupled by simultaneous electron-nuclei flip-flops, governed by A. This is responsible for the anti-crossing observed between the states M_z=+5/2 and M_z=+3/2 in the inset of Fig. 6.9. At the resonance, as D_0 blocks further evolution in the spin ladder, the electronic and nuclear spins will start to oscillate at a frequency governed by A. This coherent oscillation controlled during a time Δt could be exploited for a coherent manipulation of the electronic Mn spin.

6.4.2 Optical switching of the Mn spin at zero magnetic field.

We consider a Mn spin in the state +5/2. With a large value of $\mathcal{D}_0$ (larger than 5 μeV), the coherent precession of the electronic and nuclear spin is blocked. The precession starts when a control laser tuned on resonance with the (X,+5/2) transition is turned on putting on resonance +5/2 and +3/2 levels. The hyperfine interaction

$$\mathcal{H}_{Hyper} = \mathcal{A}[I_z M_z + \frac{1}{2}(I^+ M^- + I^- M^+)] \tag{6.6}$$

simultaneously flips the electronic and nuclear spins with a characteristic time governed by $\mathcal{A}$. With $\mathcal{A}$=0.68μeV a flip-flop occurs in typically 6 ns. If the control laser is switched off after this characteristic time, the precession stops and the Mn electronic spin has been switched from 5/2 to 3/2.

6.5 Optically detected coherent control via resonant microwave excitation

Optically detected magnetic resonance is often used to study the property of the nitrogen-vacancy centers in diamond (21). The nitrogen-vacancy system is similar to our single Mn doped quantum dot system except that we have more energy levels. Here we will consider the probability to use this technique in our system.

In this section, we will present a model for optically detected coherent control of a Mn spin induced by a resonant microwave excitation using optical Bloch equation. We will first derive the general optical Bloch equation for any level system driven by one and two fields and then we will show some preliminary results of this model applied to the case of an individual Mn spin in a quantum dot.

We consider the 42 levels system (6 excited states and 36 optical ground states) driven by a laser field (microwave field) which couples one ground states and one excited state (two ground states). The scheme of the system is shown in Figure 6.10. $|+1,+5/2,+5/2>$ and $|+5/2,+5/2>$ are coupled by laser with a frequency of ω_l. $|+5/2,+5/2>$ and $|+3/2,+5/2>$ are coupled by a microwave field with a frequency of ω_m. The lifetime of exciton is $1/\Gamma_r$. To induce the pumping, we introduce the rates Γ_{pump} that stands for the transition from $|+1,+5/2,+5/2>$ to all the ground states that has different Mn spin with conservation of the spin of nuclei. The relaxation of the Mn spin in the ground states is described by a rate Γ_{Mn} which conserves the nuclear spin. Notice that Mn spin flips only by 1 unit with a rate of Γ_{Mn}, which may be caused by phonons as we discussed in the previous chapters.

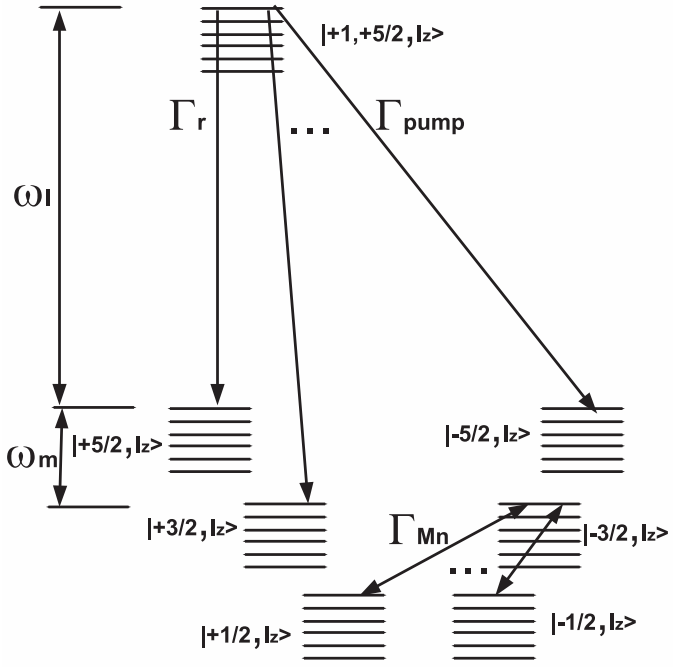

Figure 6.10: Scheme of the energy levels and transition rates involved in the optically detected coherent control model. Laser field couples $|+1,+5/2,+5/2>$ and $|+5/2,+5/2>$ with a frequency of ω_l and microwave field couples $|+5/2,+5/2>$ and $|+3/2,+5/2>$ with a frequency of ω_m. Γ_r is the recombination rates for exction, Γ_{Mn} is the relaxation rate of the Mn spin in ground states and Γ_{pump} is the transition rates from $|+1,M_z,I_z>$ to $|M_z',I_z>$ $(M_z \neq M_z')$

The Hamiltonian of the system can be written as follows:

$$
\begin{aligned}
H &= H_{dot} + H_{ESR} + H_{d-L} && (6.7)\\
H_{ESR} &= \hat{M} \cdot g\mu_B \vec{B} Cos\,(\omega_m t) && (6.8)\\
H_{d-L} &= \hat{d} \cdot \vec{\epsilon} Cos\,(\omega_l t) && (6.9)\\
H_{dot} &= H_A + H_{e-Mn} + H_{h-Mn} + H_{e-h} && (6.10)\\
H_A &= D_0 M_z^2 + A\vec{I} \cdot \vec{M} + \frac{a}{6}(M_x^4 + M_y^4 + M_z^4) && (6.11)
\end{aligned}
$$

H_{dot} is the total carrier-Mn Hamiltonian. It contains the electron-Mn (H_{e-Mn}), hole-Mn (H_{h-Mn}), and electron-hole coupling (H_{e-h}). H_A is the Hamiltonian of the empty quantum dot, described in equation 3.79 in chapter 3 at zero magnetic field. It contains the magnetic anisotropy ($D_0 \cdot M_z^2$), the hyperfine coupling ($A\vec{I} \cdot \vec{M}$) and the tetragonal crystal field. H_{ESR} and H_{d-L} are the coupling between the atom and microwave/laser field respectively. ω_m/ω_l are the frequency of the microwave/laser, $\hat{d}$ is the electric dipole moment of the atom and $\vec{\epsilon}$ is the amplitude of the laser electric field. $\hat{M}$ is the magnetic dipole moment of the atom and $\vec{B}$ is the amplitude of the incident microwave field. We define $\hat{d} \cdot \vec{\epsilon} = \hbar\Omega_l$, Ω_l is the Rabi frequency of the laser field-atom interaction and $\hbar\Omega$ is the corresponding Rabi energy, which depends on the power of the laser. Similarly, we can define a Rabi frequency and Rabi energy for microwave-nuclei coupling. The diagonalization of H_{dot} gives:

$$H_{dot}\phi_n = E_n\phi_n \tag{6.12}$$

where E_n are the eigenvalues of the Hamiltonian and the corresponding wave function ϕ_n of the system can be written in the product basis:

$$\phi_n = \sum_i C_i^n |X_i M_z^i> \tag{6.13}$$

where $|X_i M_z^i>$ is the basis of the X+Mn system, X_i is the spin of the exciton, it can be $-2, -1, +1, +2$ and M_z^i is the spin of Mn in z direction. We write down the Schrodinger equation:

$$i\hbar\dot{\sigma} = [H, \sigma] \tag{6.14}$$

To start our analysis, we first assume that H_{ESR} couple $|m_1\rangle$ and $|n_1\rangle$, and H_{d-L} couples $|m_2\rangle$ and $|n_2\rangle$. By expanding the equation 6.14 in the product basis, and adding the damping terms from spontaneous emission relaxation, we get the Bloch equation for the multi-level system which is discussed in detail in the following section.

6.5.1 Bloch equation under one monochromatic field

We first consider the Bloch equation for a multi-level system driven by one monochromatic field.

We assume the interaction between the atom and the monochromatic field can be described by:

$$H_{inter} = \hat{W} Cos(\omega t) \tag{6.15}$$

Where $\hat{W} = \hbar\Omega$. The Liouville Von-Neumann equation of the system can be written as:

$$i\hbar\dot{\sigma} = [H + H_{inter}, \sigma] \tag{6.16}$$

where H is the Hamiltonian of the atom. We assume the interaction Hamiltonian couples states $|m\rangle$ and $|n\rangle$, where $|m\rangle$ is the ground state and $|n\rangle$ is the excited state. The Hamiltonian in the basis $\{|m\rangle, |n\rangle, \cdots\}$ can be written:

$$\begin{aligned} H_{inter} &= (W_{mn}|m\rangle\langle n| + W_{nm}|n\rangle\langle m|)\, Cos\omega t \\ &= \frac{1}{2}\{e^{i\omega t}W_{mn}|m\rangle\langle n| + e^{-i\omega t}W_{nm}|n\rangle\langle m| + e^{-i\omega t}W_{mn}|m\rangle\langle n| \\ &\quad + e^{i\omega t}W_{nm}|n\rangle\langle m|\} \end{aligned} \tag{6.17}$$

The first two terms inside the brace describe processes where the atom falls from n to m by emitting a photon and rises from m to n by absorbing a photon. These process are resonant near $\omega = \omega_0$, where ω_0 is the emission frequency of the transition $n \to m$. The nonresonant processes associated with the last two terms in equation 6.17 where the atom falls from n to m by absorbing a photon and rises from m to n by emitting photon. Therefore, we omit the last two terms of equation 6.17, this approximation is called the rotating-wave approximation. We get:

$$H_{inter} \approx \frac{1}{2}\left\{e^{i\omega t}W_{mn}|m\rangle\langle n| + e^{-i\omega t}W_{nm}|n\rangle\langle m|\right\} \tag{6.18}$$

Using this approximation, after a straightforward calculation, we get the Liouville Von-Neumann equation (equation 6.16) in the basis of energy eigenstates.

$$\begin{aligned} i\hbar\dot{\sigma}_{ij} &= \frac{1}{2}\{e^{i\omega t}W_{mn}\sigma_{nj}\delta_{im} + e^{-i\omega t}W_{nm}\sigma_{mj}\delta_{in} \\ &\quad - e^{i\omega t}W_{mn}\sigma_{im}\delta_{jn} - e^{-i\omega t}W_{nm}\sigma_{in}\delta_{jm}\} + \hbar\omega_{ij}\sigma_{ij} \end{aligned} \tag{6.19}$$

Right now, we did not consider the coupling between the atom and the vacuum, which caused the spontaneous emission. Here we describe the effect of spontaneous emission by using the same terms as those derived in the absence of radiation field, we neglect the modifications of spontaneous emission connected with the presence of the incident radiation. Such an approximation is valid if the effect of the coupling with this radiation can be neglected during the correlation time of the vacuum fluctuations that are responsible for spontaneous emission, that is indeed the case if the Rabi frequency is much smaller than the frequency of the transition of the coupled two levels. By adding the damping terms of spontaneous emission, we can get the optical Bloch equation(74):

First, we get the time evolution of the population σ_{ii}:

$$\begin{aligned}\dot{\sigma}_{ii} &= \frac{1}{2i\hbar}\{e^{i\omega t}W_{mn}\sigma_{ni}\delta_{im} + e^{-i\omega t}W_{nm}\sigma_{mi}\delta_{in} - e^{i\omega t}W_{mn}\sigma_{im}\delta_{in} \\ &\quad -e^{-i\omega t}W_{nm}\sigma_{in}\delta_{im}\} + \sum_{p\neq i}\Gamma_{p\to i}\sigma_{pp} - \sum_{q\neq i}\Gamma_{i\to q}\sigma_{ii} \end{aligned} \tag{6.20}$$

Second, we get the time evolution of the coherence $\sigma_{ij}(i \neq j)$:

$$\begin{aligned}\dot{\sigma}_{ij} &= \frac{1}{2i\hbar}\{e^{i\omega t}W_{mn}\sigma_{nj}\delta_{im} + e^{-i\omega t}W_{nm}\sigma_{mj}\delta_{in} - e^{i\omega t}W_{mn}\sigma_{im}\delta_{jn} \\ &\quad -e^{-i\omega t}W_{nm}\sigma_{in}\delta_{jm}\} - i\omega_{ij}\sigma_{ij} + R_{ijij}\sigma_{ij} \end{aligned} \tag{6.21}$$

Right now, the coefficients in the evolution equation of both population and coherence are time dependent. We can suppress any time dependence in the coefficients of these equations by introducing new variables:

$$\begin{aligned}\hat{\sigma}_{ij} &= e^{i\omega t}\sigma_{ij} && \text{i, j}\in \text{m, n or i, j}\notin\text{m, n and i}\neq\text{j and } E_i > E_j \\ \hat{\sigma}_{ij} &= e^{-i\omega t}\sigma_{ij} && \text{i, j}\in \text{m, n or i, j}\notin\text{m, n and i}\neq\text{j and } E_i < E_j \\ \hat{\sigma}_{im} &= \sigma_{im}e^{i\omega t} && \hat{\sigma}_{in} = \sigma_{in} \qquad \text{i}\notin \text{m, n} \\ \hat{\sigma}_{mj} &= \sigma_{mj}e^{-i\omega t} && \hat{\sigma}_{nj} = \sigma_{nj} \qquad \text{j}\notin \text{m, n} \\ \hat{\sigma}_{ii} &= \sigma_{ii} \end{aligned}$$

Using these new variables, we get the evolution of the population:

$$\dot{\hat{\sigma}}_{ii} = \frac{1}{2i\hbar}\{W_{mn}\hat{\sigma}_{nm}(\delta_{im}-\delta_{in}) + W_{nm}\hat{\sigma}_{mn}(\delta_{in}-\delta_{im})\} + \sum_{p\neq i}\Gamma_{p\to i}\hat{\sigma}_{pp} - \sum_{q\neq i}\Gamma_{i\to q}\hat{\sigma}_{ii} \tag{6.22}$$

and we can get the evolution of coherence:

$$\begin{aligned}\dot{\hat{\sigma}}_{ij} &= \frac{1}{2i\hbar}\left(W_{nm}\hat{\sigma}_{mm}\delta_{in} - W_{nm}\hat{\sigma}_{nn}\delta_{jm} + W_{mn}\hat{\sigma}_{nn}\delta_{im} - W_{mn}\hat{\sigma}_{mm}\delta_{jn}\right) \\ &\quad +i\left(\gamma_{ij}-\omega_{ij}\right)\hat{\sigma}_{ij} + R_{ijij}\hat{\sigma}_{ij} \end{aligned} \tag{6.23}$$

where γ_{ij} is defined by $\hat{\sigma}_{ij} = \sigma_{ij}e^{i\gamma_{ij}t}$ and $\hbar\omega_{ij} = E_i - E_j$, which is the energy difference between the two states i and j.

So far we get the optical Bloch equation for a mutli-level system under one monochromatic field. These new variables removes the time dependence in the coefficients and makes the equation much simpler. Notice that the populations keep the same form for the new variables. We will derive the optical Bloch equation for a multi-level system under two monochromatic field in the next section.

6.5.2 Bloch equation under two monochromatic field

We can write down the Liouville-Von Neumann equation as:

$$i\hbar\dot{\sigma} = \left[H + \hat{W}Cos\omega_1 t + \hat{W}'Cos\omega_2 t, \sigma\right] \tag{6.24}$$

Where W couples m_1 and n_1, W' couples m_2 and n_2. m_i are the lower level and n_i are the higher level coupled by the field. We suppose n_1 and n_2 are different here. Analogous to the one monochromatic field case, we can get the Bloch equation. For $i = j$, we get the time evolution for the population:

$$\begin{aligned}
\dot{\sigma}_{ii} &= \frac{1}{2i\hbar}\{e^{i\omega_1 t}W_{m_1n_1}\sigma_{n_1i}\delta_{im_1} + e^{-i\omega_1 t}W_{n_1m_1}\sigma_{m_1i}\delta_{in_1} - e^{i\omega_1 t}W_{m_1n_1}\sigma_{im_1}\delta_{in_1} \\
&\quad -e^{-i\omega_1 t}W_{n_1m_1}\sigma_{in_1}\delta_{im_1}\} + \frac{1}{2i\hbar}\{e^{i\omega_2 t}W'_{m_2n_2}\sigma_{n_2i}\delta_{im_2} \\
&\quad +e^{-i\omega_2 t}W'_{n_2m_2}\sigma_{m_2i}\delta_{in_2} - e^{i\omega_2 t}W'_{m_2n_2}\sigma_{im_2}\delta_{in_2} - e^{-i\omega_2 t}W'_{n_2m_2}\sigma_{in_2}\delta_{im_2}\} \\
&\quad + \sum_{p\neq i}\Gamma_{p\to i}\sigma_{pp} - \sum_{q\neq i}\Gamma_{i\to q}\sigma_{ii}
\end{aligned} \tag{6.25}$$

For $i \neq j$, we get the time evolution for the coherence:

$$\begin{aligned}
\dot{\sigma}_{ij} &= \frac{1}{2i\hbar}\{e^{i\omega_1 t}W_{m_1n_1}\sigma_{n_1j}\delta_{im_1} + e^{-i\omega_1 t}W_{n_1m_1}\sigma_{m_1j}\delta_{in_1} - e^{i\omega_1 t}W_{m_1n_1}\sigma_{im_1}\delta_{jn_1} \\
&\quad -e^{-i\omega_1 t}W_{n_1m_1}\sigma_{in_1}\delta_{jm_1}\} + \frac{1}{2i\hbar}\{e^{i\omega_2 t}W'_{m_2n_2}\sigma_{n_2j}\delta_{im_2} + e^{-i\omega_2 t}W'_{n_2m_2}\sigma_{m_2j}\delta_{in_2} \\
&\quad -e^{i\omega_2 t}W'_{m_2n_2}\sigma_{im_2}\delta_{jn_2} - e^{-i\omega_2 t}W'_{n_2m_2}\sigma_{in_2}\delta_{jm_2}\} \\
&\quad -i\omega_{ij}\sigma_{ij} + R_{ijij}\sigma_{ij}
\end{aligned} \tag{6.26}$$

Employing the following new variables, we can get the time-independent form of Bloch equation for a multilevel system driven by two monochromatic field.

$$\begin{aligned}
\hat{\sigma}_{n_1m_1} &= \sigma_{n_1m_1}e^{i\omega_1 t} & \hat{\sigma}_{m_1n_1} &= \sigma_{m_1n_1}e^{-i\omega_1 t} & \\
\hat{\sigma}_{n_2m_2} &= \sigma_{n_2m_2}e^{i\omega_2 t} & \hat{\sigma}_{m_2n_2} &= \sigma_{m_2n_2}e^{-i\omega_2 t} & \\
\hat{\sigma}_{im_1} &= \sigma_{im_1} & \hat{\sigma}_{im_2} &= \sigma_{im_2} & i \notin m_1, n_1, m_2, n_2 \\
\hat{\sigma}_{in_1} &= \sigma_{in_1}e^{-i\omega_1 t} & \hat{\sigma}_{in_2} &= \sigma_{in_2}e^{-i\omega_2 t} & i \notin m_1, n_1, m_2, n_2 \\
\hat{\sigma}_{m_1j} &= \sigma_{m_1j} & \hat{\sigma}_{m_2j} &= \sigma_{m_2j} & j \notin m_1, n_1, m_2, n_2 \\
\hat{\sigma}_{n_1j} &= \sigma_{n_1j}e^{i\omega_1 t} & \hat{\sigma}_{n_2j} &= \sigma_{n_2j}e^{i\omega_2 t} & j \notin m_1, n_1, m_2, n_2 \\
\hat{\sigma}_{ij} &= \sigma_{ij} & i, j \notin n_1, m_1, n_2, m_2 & \text{ and } i \neq j & \\
\hat{\sigma}_{ii} &= \sigma_{ii} & & &
\end{aligned} \tag{6.27}$$

For $n_1 \neq m_2$:

$$\begin{aligned}
\hat{\sigma}_{n_1n_2} &= \sigma_{n_1n_2}e^{i(\omega_1-\omega_2)t} & \hat{\sigma}_{m_1n_2} &= \sigma_{m_1n_2}e^{-i\omega_2 t} \\
\hat{\sigma}_{n_1m_2} &= \sigma_{n_1m_2}e^{i\omega_1 t} & \hat{\sigma}_{m_1m_2} &= \sigma_{m_1m_2} \\
\hat{\sigma}_{n_2n_1} &= \sigma_{n_2n_1}e^{i(\omega_2-\omega_1)t} & \hat{\sigma}_{m_2n_1} &= \sigma_{m_2n_1}e^{-i\omega_1 t} \\
\hat{\sigma}_{n_2m_1} &= \sigma_{n_2m_1}e^{i\omega_2 t} & \hat{\sigma}_{m_2m_1} &= \sigma_{m_2m_1}
\end{aligned} \tag{6.28}$$

For $n_1 = m_2$:

$$\begin{aligned}
\hat{\sigma}_{n_1n_2} &= \sigma_{n_1n_2}e^{-i\omega_2 t} & \hat{\sigma}_{m_1n_2} &= \sigma_{m_1n_2}e^{-i(\omega_1+\omega_2)t} \\
\hat{\sigma}_{n_1m_2} &= \sigma_{n_1m_2} & \hat{\sigma}_{m_1m_2} &= \sigma_{m_1m_2}e^{-i\omega_1 t} \\
\hat{\sigma}_{n_2n_1} &= \sigma_{n_2n_1}e^{i\omega_2 t} & \hat{\sigma}_{m_2n_1} &= \sigma_{m_2n_1} \\
\hat{\sigma}_{n_2m_1} &= \sigma_{n_2m_1}e^{i(\omega_1+\omega_2)t} & \hat{\sigma}_{m_2m_1} &= \sigma_{m_2m_1}e^{i\omega_1 t}
\end{aligned} \tag{6.29}$$

After a straightforward calculation, we get the evolution of the population:

$$\begin{aligned}
\dot{\hat{\sigma}}_{ii} = & \frac{1}{2i\hbar}\left\{W_{m_1n_1}\hat{\sigma}_{n_1m_1}(\delta_{im_1}-\delta_{in_1}) + W_{n_1m_1}\hat{\sigma}_{m_1n_1}(\delta_{in_1}-\delta_{im_1})\right\} \\
& + \frac{1}{2i\hbar}\left\{W'_{m_2n_2}\hat{\sigma}_{n_2m_2}(\delta_{im_2}-\delta_{in_2}) + W'_{n_2m_2}\hat{\sigma}_{m_2n_2}(\delta_{in_2}-\delta_{im_2})\right\} \\
& + \sum_{p\neq i}\Gamma_{p\to i}\hat{\sigma}_{pp} - \sum_{q\neq i}\Gamma_{i\to q}\hat{\sigma}_{ii}
\end{aligned} \tag{6.30}$$

We can also get the coherent evolution:

$$\begin{aligned}
\dot{\hat{\sigma}}_{ij} = & \frac{1}{2i\hbar}\left\{W_{m_1n_1}(\hat{\sigma}_{n_1j}\delta_{im_1} - \hat{\sigma}_{im_1}\delta_{jn_1}) + W_{n_1m_1}(\hat{\sigma}_{m_1j}\delta_{in_1} - \hat{\sigma}_{in_1}\delta_{jm_1})\right\} \\
& + \frac{1}{2i\hbar}\left\{W'_{m_2n_2}(\hat{\sigma}_{n_2j}\delta_{im_2} - \hat{\sigma}_{im_2}\delta_{jn_2}) + W'_{n_2m_2}(\hat{\sigma}_{m_2j}\delta_{in_2} - \hat{\sigma}_{in_2}\delta_{jm_2})\right\} \\
& + i\left(\gamma_{ij} - \omega_{ij}\right)\hat{\sigma}_{ij} + \sum_{i'j'}^{sec} R_{i'j'ij}\hat{\sigma}_{ij}
\end{aligned} \tag{6.31}$$

where

$$\hat{\sigma}_{ij} = \sigma_{ij}e^{i\gamma_{ij}t} \tag{6.32}$$

and $\hbar\omega_{ij} = E_i - E_j$, the energy difference between the states i and j. $\sum_{i'j'}^{sec} R_{i'j'ij}$ is the Redfield factor (74)

6.5.3 Optically detected coherent control of Mn spin

Now we use the Bloch equation (Equation 6.30 and Equation 6.31) discussed in the above section 6.5.2 to calculate the steady states of the 42 levels system driven by the laser and the microwave fields. Figure 6.10 shows the scheme of the system.

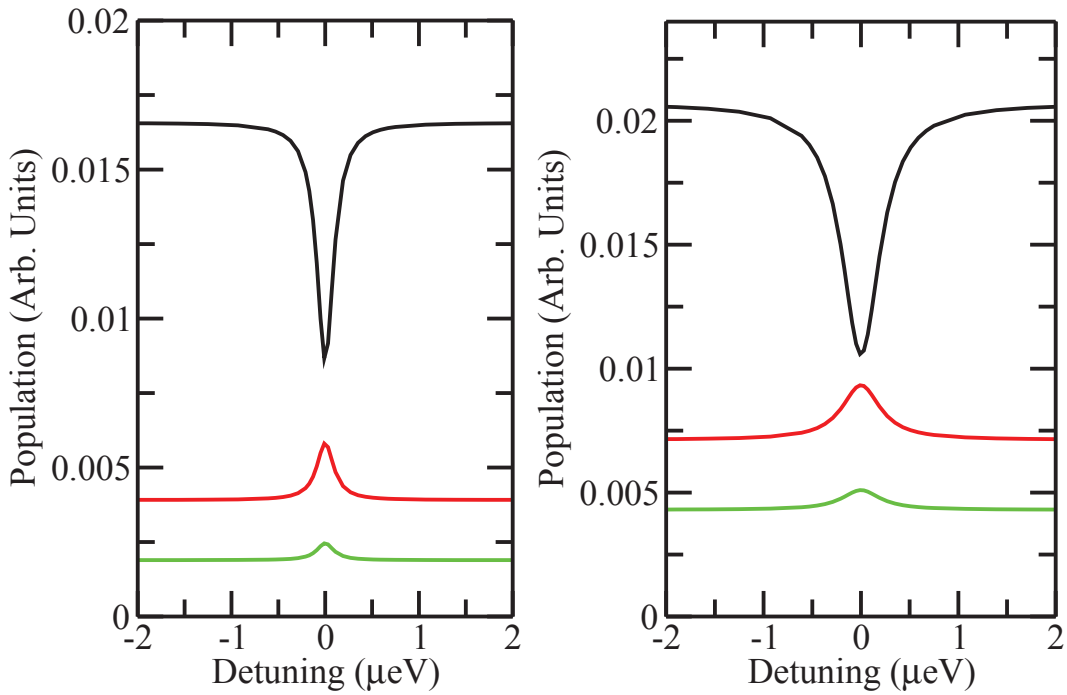

Figure 6.11: Population vs microwave detuning. Black line is the population of $|+5/2,+5/2>$ the red line is the population of $|+3/2,+5/2>$ and the green line is the population of $|+1,+5/2,+5/2>$. $\Gamma_{Mn} = (20\mu s)^{-1}$ for the left panel and $\Gamma_{Mn} = (10\mu s)^{-1}$ for the right panel respectively and $\Gamma_r = (0.25ns)^{-1}$, $\Gamma_{pump} = (100ns)^{-1}$ for both panels, the power of microwave and laser are P_m and P_l for both panels.

In the system driven by two monochromatic fields (laser and microwave), the laser/microwave couples several pairs of energy levels whose emission frequency is close to the laser/microwave frequency with different detuning. However, it is a good approximation that the laser or microwave couples only one pair of levels. This approximation simplify the calculation and can show some basic properties of the optically detected coherent control induced by microwave excitation in our system.

Since we are indeed interested in the steady state, instead of calculating the time evolution of the population (Equation 6.30) and coherence (Equation 6.31), we can solve the optical Bloch equations with steady state condition $\hat{\sigma}_{ij} = 0$ to uniquely determine the steady state (see Appendix E for details).

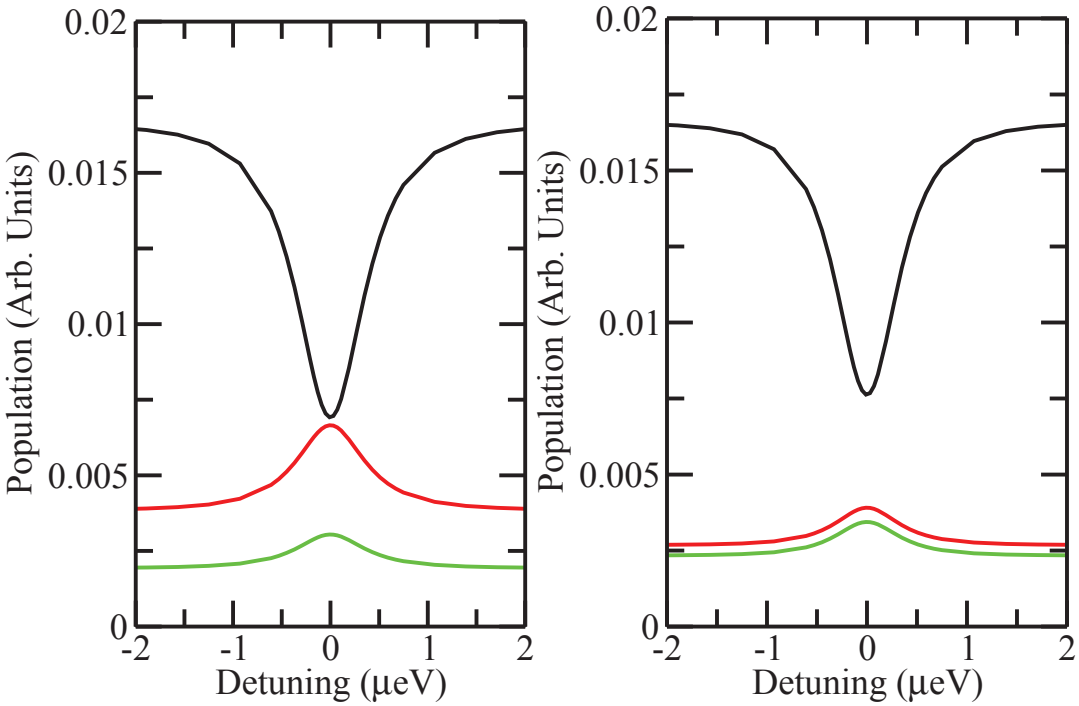

Figure 6.12: Population vs microwave detuning. Black line is the population of $|+5/2, +5/2>$ the red line is the population of $|+3/2, +5/2>$ and the green line is the population of $|+1, +5/2, +5/2>$. $\Gamma_{Mn} = (20\mu s)^{-1}$, $\Gamma_r = (0.25ns)^{-1}$ and $\Gamma_{pump} = (100ns)^{-1}$ for both panels, the power of microwave and laser are $2P_m$, P_l for the left panel and P_m, $2P_l$ for the right panel

Figure 6.11 and Figure 6.12 demonstrated the detuning dependence of population under different parameters. This calculation shows how the change of the ground state

levels induced by the microwave could be detected optically, through the corresponding change of the occupation of the exciton level, which would imply a change in the photoluminescence. The microwave couples states $|+5/2,+5/2>$ and $|+3/2,+5/2>$. The detuning is the energy difference between the splitting of these two coupled states and the energy of the microwave. The laser couples states $|+1,+5/2,+5/2>$ and $|+5/2,+5/2>$ resonantly. Comparing the left panel and right panel of figure 6.11, we can see that the linewidth increases with the transition rate in the ground states which is consistent with the NMR experiments. We also notice that the pumping is less efficient for the ground states with a larger lifetime $\Gamma_{Mn} = (20\mu s)^{-1}$ (left panel) than for the ground states with a smaller lifetime $\Gamma_{Mn} = (10\mu s)^{-1}$ (right panel). Comparing the left panel of figure 6.11 and the right panel of figure 6.12, we can see that with the increase of the power of the laser, the population of the optical excited states gets bigger, it is because the laser can excite more population to $|+1,+5/2,+5/2>$, and consequently the population of state $|+5/2,+5/2>$ is depleted. The linewidth is also broadened with the increase of the power of the laser and microwave field.

6.6 Conclusion

In this chapter, we discussed the coherent dynamics of a Mn spin in a quantum dot. After the introduction of the experimental evidence of optical Stark effect, we proposed a model to describe the coherent control of a Mn spin using time resolved optical Stark effect, then, we discussed the influence of the coherent dynamics on the optical pumping and suggested possible use of optically controlled electron-nuclei coupling for Mn spin switching. Finally, we discussed optically detected microwave excitation. In this model, we avoided the calculation of the fast oscillation induced by the coherent coupling using singular value decomposition.

7

Conclusion

In this thesis, models to study the spin dynamics in Mn doped CdTe quantum were presented. Our core goal was to explain the optical pumping experiment performed recently and to understand the origin of the observed fast optical spin orientation.

We first presented some recent experiments showing that an efficient optical spin orientation of a single magnetic atom in a semiconductor host can be performed. These experiments shows that the Mn spin lifetime in the ground state is larger than a few microseconds. This fast optical pumping requires an efficient Mn spin relaxation in the presence of an exciton in the quantum dot. These experiments also suggested a strong influence of the Mn fine and hyperfine structure of the Mn on the pumping process.

We then developed a model to explain these experimental results. We have first described the different terms in the Mn spin Hamiltonian, including exchange with the 0-dimensional exciton, presented the Mn spin Hamiltonian with or without the presence of the exciton, derived the effective Mn-hole coupling employing the pseudo spin method. Our calculation suggested that the hole-Mn interaction are strongly affected by the interplay of confinement, strain and spin orbit coupling. Then, we presented a detailed spin effective model showing that for isotropic quantum dots, one expects a significant influence of the nuclear Mn spin on the optical emission of the exciton confined in a Mn-doped CdTe quantum dot. We also presented and modelled the emission spectrum of quantum dot containing two Mn atoms. To simulate the optical pumping experiments, we introduced a simple rate equation model employing phenomenological transition rates to describe the exciton Mn dynamics.

To study the spin relaxation mechanism and the optical Mn spin orientation in detail, we developed a quantum dot model in order to compute the carrier-phonon coupling and its influence on the spin dynamics of the exciton Mn system. The Mn spin-phonon coupling arises from the time dependent stochastic fluctuations of the crystal field and thereby of the single ion magnetic anisotropy, induced by the phonon field. Since Mn spin relaxation in the presence of the exciton is too slow to account for the

optical orientation of the Mn spin reported experimentally(6, 10, 11), we investigated the interaction between the hole spin and the phonons in magnetic quantum dots as a possible origin for spin orientation. We find that hole spin lifetime can be in the range of 30 ns for a hole spin splitting as large as that provided by the hole-Mn coupling. Thus, bright excitons relax into dark excitons via hole-spin relaxation, resulting in photoluminescence from dark states which implies Mn spin relaxation in a time scale of a few tens of nanoseconds. The hole-Mn exchange and the hole spin relaxation are governed by the mixing between light and heavy holes, which depends both on the shape of the dot and on strain. In Chapter 5, we showed how these calculated spin flip rates can explain the observed spin dynamics in Mn doped quantum dots driven by a resonant laser field.

In the last part of the thesis, we discussed the coherent dynamics of a Mn spin in a quantum dot. We proposed a model to describe the coherent control of a Mn spin using time resolved optical Stark effect, then, we discussed the influence of the coherent dynamics on optical pumping. We have shown that the optically controlled electron-nuclei coupling could be used for a Mn spin switching. Then, we discussed the optically detected microwave excitation. We have shown how the change in the population of the ground state levels induced by the microwave could be detected optically, through the corresponding change of the occupation of the exciton level detected in the photoluminescence.

Appendix A

Kohn Luttinger Hamiltonian in short notation

In this appendix, we derive the Kohn-Luttinger Hamiltonian in short notation, which is used in Chapter 3.

Using the notation in Chapter 3, the Kohn-Luttinger Hamiltonian for the 4 topmost valence bands of a zinc-blend compound under zero mangentic field is given by:

$$V^{\mathrm{KL}}(k_x, k_y, k_z) = \begin{pmatrix} P+Q & S & R & 0 \\ S^\dagger & P-Q & 0 & R \\ R^\dagger & 0 & P-Q & -S \\ 0 & R^* & -S^* & P+Q \end{pmatrix} \tag{A.1}$$

We can write this Hamiltonian as:

$$H = PM_P + QM_Q + RM_R + R^*M_{R*} + SM_S + S^*M_{S*} \tag{A.2}$$

where M_i is a 4 by 4 matrice that we can express in terms of the $J = 3/2$ matrices shown in appendix C.

From inspection, it is trivial that

$$M_P = 1 = \frac{1}{J(J+1)}(J_x^2 + J_y^2 + J_z^2)$$

.

In the case of M_Q, a bit of algebra (using the angular momentums matrices presented in appendix C) leads to:

$$M_Q = J_z^2 - \frac{5}{4}1 = J_z^2 - \frac{5}{4}\left(J_x^2 + J_y^2 + J_z^2\right)$$

.

The R terms must be related to $J_x^2 - J_y^2 \pm i(J_xJ_y + J_yJ_x)$. We can check that:

$$M_R = \frac{1}{2\sqrt{3}}\left(J_x^2 - J_y^2 - i(J_xJ_y + J_yJ_x)\right)$$

Unsurprisingly, we have:

$$M_{R^*} = \frac{1}{2\sqrt{3}}\left(J_x^2 - J_y^2 + i(J_xJ_y + J_yJ_x)\right)$$

Finally, the S terms are written as:

$$M_S = \frac{-1}{2\sqrt{3}}\left(i(J_yJ_z + J_zJ_y) + J_zJ_x + J_xJ_z\right)$$

and

$$M_{S^*} = \frac{1}{2\sqrt{3}}\left(i(J_yJ_z + J_zJ_y) - J_zJ_x - J_xJ_z\right)$$

Thus, we can finally write:

$$H = \sum_{ij=x,y,z} V_{ij}J_iJ_j \tag{A.3}$$

where

$$V_{ij} = \begin{pmatrix} V_{xx} & V_{xy} & V_{xz} \\ V_{yx} & V_{yy} & V_{yz} \\ V_{zx} & V_{zy} & V_{zz} \end{pmatrix} \tag{A.4}$$

with :

$$\begin{aligned}
V_{xx} &= \frac{4}{15}P - \frac{5}{4}Q + \frac{R}{2\sqrt{3}} + \frac{R^*}{2\sqrt{3}} \\
V_{xy} &= \frac{-i}{2\sqrt{3}}R + \frac{i}{2\sqrt{3}}R^* \\
V_{xz} &= \frac{-1}{2\sqrt{3}}S - \frac{1}{2\sqrt{3}}S^* \\
V_{yx} &= \frac{-i}{2\sqrt{3}}R + \frac{i}{2\sqrt{3}}R^* \\
V_{yy} &= \frac{4}{15}P - \frac{5}{4}Q + \frac{R}{2\sqrt{3}} + \frac{R^*}{2\sqrt{3}} \\
V_{yz} &= \frac{-i}{2\sqrt{3}}S + \frac{i}{2\sqrt{3}}S^* \\
V_{zx} &= \frac{-1}{2\sqrt{3}}\left(S + S^*\right) \\
V_{zy} &= \frac{i}{2\sqrt{3}}\left(-S + S^*\right) \\
V_{zz} &= \frac{4}{15}P - \frac{1}{4}Q
\end{aligned}$$

Now, we can write the Kohn-Luttinger Hamiltonian under an additional magentic field in a short notation as follows:

$$\mathcal{H}_{\mathrm{KL}} = \sum_{i,j=x,y,z} V_{ij}^{\mathrm{KL}}(\vec{k}) J_i J_j + \kappa \mu_B J_z B \tag{A.5}$$

A. KOHN LUTTINGER HAMILTONIAN IN SHORT NOTATION

Appendix B

Bir-Pikus Hamiltonian in a strained quantum dots

The Bir-Pikus Hamiltonian describes the effect of strain on the top of the valence band states in zinc-blende semicondouctors. It reads(68):

$$\mathcal{H}_{\rm BP} = a(e_{xx}+e_{yy}+e_{zz}) + b\left[(J_x^2-\frac{J^2}{3})e_{xx}+c.p.\right] + \frac{2d}{\sqrt{3}}\left(\frac{1}{2}(J_xJ_y+J_yJ_x)e_{xy}+c.p.\right) \tag{B.1}$$

where a, b and d are the three deformation potentials and $c.p.$ stands for coordinate permutation. For CdTe we have $a=-0.91eV$, $b=-1.2eV$, $d=-5.4eV$. we can also write:

$$\mathcal{H}_{\rm BP} = \left(a-\frac{3b}{4}\right)(e_{xx}+e_{yy}+e_{zz}) + b\sum_{i=x,y,z} J_i^2 e_{ii} + \frac{d}{\sqrt{3}}\sum_{i,j,c.p.}(J_iJ_j+J_jJ_i)\,e_{ij} \tag{B.2}$$

For CdTe quantum dots grown in CdTe, we mainly consider the effects of strain anisotropy in the growth plane(92) and describe the strain by the average values of e_{xy} and $e_{xx}-e_{yy}$. Thus, we keep the following terms in the BP Hamiltonian

$$\begin{aligned}\mathcal{H}_{\rm BP} &= a(e_{xx}-e_{yy}) + b\left[(J_x^2-\frac{J^2}{3})e_{xx}+(J_y^2-\frac{J^2}{3})e_{yy}\right] + \frac{2d}{\sqrt{3}}\left(\frac{1}{2}(J_xJ_y+J_yJ_x)e_{xy}\right)\\ &= \left(a-\frac{3b}{4}+bJ_x^2\right)e_{xx} + \left(a-\frac{3b}{4}+bJ_y^2\right)e_{yy}\\ &\quad + \frac{d}{\sqrt{3}}(J_xJ_y+J_yJ_x)\,e_{xy}\end{aligned} \tag{B.3}$$

Since naturally, the two hole states $|\Uparrow>$ and $|\Downarrow>$ described in Chapter 3 has no overlap (each of them couples two of the four J_z states independently), the constant term $a-\frac{3b}{4}$

has no contribution to the spin flip rates in the basis of $|\Uparrow>$ and $|\Downarrow>$, then it can be safely negelected, so we write:

$$\mathcal{H}_{\rm BP} = bJ_x^2 e_{xx} + bJ_y^2 e_{yy} + \frac{d}{\sqrt{3}}\left(J_x J_y + J_y J_x\right) e_{xy} \tag{B.4}$$

$$= V_{ij} e_{ij} \tag{B.5}$$

In the $(+3/2, -1/2, +1/2, -3/2)$ basis, the Bir-Pikus Hamiltonian is reduced to a block diagonal matrix

$$\mathcal{H}_{BP} = \begin{pmatrix} \mathcal{H}_{BP+} & 0 \\ 0 & \mathcal{H}_{BP-} \end{pmatrix} \tag{B.6}$$

where :

$$\mathcal{H}_{BP+} = \begin{pmatrix} P+Q & R \\ R^* & P-Q \end{pmatrix} \tag{B.7}$$

$$\mathcal{H}_{BP-} = \begin{pmatrix} P-Q & R \\ R^* & P+Q \end{pmatrix} \tag{B.8}$$

with

$$P = a\sum_i e_{ii} \tag{B.9}$$

$$Q = b\left(\frac{e_{xx}+e_{yy}}{2}\right) \tag{B.10}$$

$$R = ide_{xy} - b\frac{\sqrt{3}}{2}\left(e_{xx}-e_{yy}\right) \tag{B.11}$$

using the heavy hole band as the orign of the energies in the valence-band:

$$\mathcal{H}_{BP+} = \begin{pmatrix} 0 & \rho_s e^{-2i\varphi_s} \\ \rho_s e^{2i\varphi_s} & \Delta_{lh-hh} \end{pmatrix} \tag{B.12}$$

$$\mathcal{H}_{BP-} = \begin{pmatrix} \Delta_{lh-hh} & \rho_s e^{-2i\varphi_s} \\ \rho_s e^{2i\varphi_s} & 0 \end{pmatrix} \tag{B.13}$$

this notation allows us to introduce useful parameters to describe the strain effects, namely, the light-heavy hole splitting Δ_{lh-hh}, the strain coupling amplitude ρ_s, and the strain induced anisotropy axis in the QD plane defined by the angle φ_s with respect to the x (100) axis corresponding to the cleaved edge of the sample.

Appendix C

Angular momentum matrices for hole

$$J_X = \begin{pmatrix} 0 & \frac{\sqrt{3}}{2} & 0 & 0 \\ \frac{\sqrt{3}}{2} & 0 & 1 & 0 \\ 0 & 1 & 0 & \frac{\sqrt{3}}{2} \\ 0 & 0 & \frac{\sqrt{3}}{2} & 0 \end{pmatrix} \quad J_Y = \begin{pmatrix} 0 & \frac{\sqrt{3}i}{2} & 0 & 0 \\ -\frac{\sqrt{3}i}{2} & 0 & i & 0 \\ 0 & -i & 0 & \frac{\sqrt{3}i}{2} \\ 0 & 0 & -\frac{\sqrt{3}i}{2} & 0 \end{pmatrix} \tag{C.1}$$

$$J_z = \begin{pmatrix} 3/2 & 0 & 0 & 0 \\ 0 & 1/2 & 0 & 0 \\ 0 & 0 & -1/2 & 0 \\ 0 & 0 & 0 & -3/2 \end{pmatrix} \tag{C.2}$$

$$J_X^2 = \begin{pmatrix} \frac{3}{4} & 0 & \frac{\sqrt{3}}{2} & 0 \\ 0 & \frac{7}{4} & 0 & \frac{\sqrt{3}}{2} \\ \frac{\sqrt{3}}{2} & 0 & \frac{7}{4} & 0 \\ 0 & \frac{\sqrt{3}}{2} & 0 & \frac{3}{4} \end{pmatrix} \quad J_Y^2 = \begin{pmatrix} \frac{3}{4} & 0 & -\frac{\sqrt{3}}{2} & 0 \\ 0 & \frac{7}{4} & 0 & -\frac{\sqrt{3}}{2} \\ -\frac{\sqrt{3}}{2} & 0 & \frac{7}{4} & 0 \\ 0 & -\frac{\sqrt{3}}{2} & 0 & \frac{3}{4} \end{pmatrix} \tag{C.3}$$

$$J_X^2 - J_Y^2 = \sqrt{3} \begin{pmatrix} 0 & 0 & 1 & 0 \\ 0 & 0 & 0 & 1 \\ 1 & 0 & 0 & 0 \\ 0 & 1 & 0 & 0 \end{pmatrix} \tag{C.4}$$

$$J_x J_y + J_y J_x = \begin{pmatrix} 0 & 0 & \sqrt{3}i & 0 \\ 0 & 0 & 0 & \sqrt{3}i \\ -\sqrt{3}i & 0 & 0 & 0 \\ 0 & -\sqrt{3}i & 0 & 0 \end{pmatrix} = \sqrt{3}i \begin{pmatrix} 0 & 0 & +1 & 0 \\ 0 & 0 & 0 & +1 \\ -1 & 0 & 0 & 0 \\ 0 & -1 & 0 & 0 \end{pmatrix} \tag{C.5}$$

$$\mathcal{J}_{y,z} \equiv J_y J_z + J_z J_y = \begin{pmatrix} 0 & i\sqrt{3} & 0 & 0 \\ -i\sqrt{3} & 0 & 0 & 0 \\ 0 & 0 & 0 & -i\sqrt{3} \\ 0 & 0 & i\sqrt{3} & 0 \end{pmatrix} \tag{C.6}$$

$$\mathcal{J}_{z,x} \equiv J_z J_x + J_x J_z = \begin{pmatrix} 0 & \sqrt{3} & 0 & 0 \\ \sqrt{3} & 0 & 0 & 0 \\ 0 & 0 & 0 & -\sqrt{3} \\ 0 & 0 & -\sqrt{3} & 0 \end{pmatrix} \tag{C.7}$$

We can now write:

$$i\mathcal{J}_{y,z} + \mathcal{J}_{z,x} = 2\sqrt{3} \begin{pmatrix} 0 & -1 & 0 & 0 \\ 0 & 0 & 0 & 0 \\ 0 & 0 & 0 & 1 \\ 0 & 0 & 0 & 0 \end{pmatrix} \tag{C.8}$$

We can now write:

$$i\mathcal{J}_{y,z} - \mathcal{J}_{z,x} = 2\sqrt{3} \begin{pmatrix} 0 & 0 & 0 & 0 \\ 1 & 0 & 0 & 0 \\ 0 & 0 & 0 & 0 \\ 0 & 0 & -1 & 0 \end{pmatrix} \tag{C.9}$$

Appendix D

Derivation of V

In chapter 5, when we calculate the effective hole-Mn Hamiltonian, we need to transform the matrix elements of V_α to a linear combination of the unit matrix and the Pauli matrices σ. In this appendix, we will show the detailed derivation of V_z, V^+ and V^-.

D.1 Calculation of V_z

In the section, we show the calculation of $V_z(h,h')$. We write:

$$\begin{aligned} V_z(h,h') &= \sum_{j_z} C_h(j_z)^* C_{h'}(j_z) j_z \\ &= \begin{pmatrix} \frac{3}{2}Cos^2(\theta_+/2) - \frac{1}{2}Sin^2(\theta_+/2) & 0 \\ 0 & -\frac{3}{2}Cos^2(\theta_-/2) + \frac{1}{2}Sin^2(\theta_-/2) \end{pmatrix} \end{aligned} \quad \text{(D.1)}$$

From here we derive:

$$V_z(h,h') = a_z 1 + b_z \sigma_z \quad \text{(D.2)}$$

with

$$a_z = \frac{1}{2}\left[\frac{3}{2}\left(Cos^2(\theta_+/2) - Cos^2(\theta_-/2)\right) - \frac{1}{2}\left(Sin^2(\theta_+/2) - Sin^2(\theta_-/2)\right)\right] \quad \text{(D.3)}$$

and

$$b_z = \frac{1}{2}\left[\frac{3}{2}\left(Cos^2(\theta_+/2) + Cos^2(\theta_-/2)\right) - \frac{1}{2}\left(Sin^2(\theta_+/2) + Sin^2(\theta_-/2)\right)\right] \quad \text{(D.4)}$$

At zero field we have $\theta_+ = \theta_-$ so that $a_z = 0$ and

$$b_z(b=0) = \frac{1}{2}\left[3Cos^2(\theta/2) - Sin^2(\theta/2)\right] = 2Cos^2(\theta/2) - \frac{1}{2} \quad \text{(D.5)}$$

D.2 Calculation of V^+

We now compute:

$$V^+(h,h') = \sum_{j_z,j_z'} C_h(j_z)^* C_{h'}(j_z') \langle j_z|J^+|j_z'\rangle \tag{D.6}$$

Using

$$\langle j_z|J^+|j_z'\rangle = \delta_{j_z,j_z'-1}\sqrt{J(J+1)-j_z(j_z+1)} \tag{D.7}$$

we can obtain

$$V^+(h,h') = \sum_{j_z} C_h(j_z)^* C_{h'}(j_z-1)\sqrt{J(J+1)-j_z(j_z+1)} \tag{D.8}$$

It is apparent that the diagonal entries of V^+ are zero. We now compute:

$$\begin{aligned}\langle \Uparrow |V^+| \Downarrow\rangle &= Cos\theta_+/2 Sin\theta_-/2\langle +3/2|J^+|+1/2\rangle + Sin\theta_+/2 Cos\theta_-/2\langle -1/2|J^+|-3/2\rangle \\ &= \sqrt{3}Sin\left(\frac{\theta_+ + \theta_-}{2}\right)\end{aligned} \tag{D.9}$$

Similarly, we obtain

$$\langle \Downarrow |V^+| \Uparrow\rangle = Sin\theta_-/2 Sin\theta_+/2\langle +1/2|J^+|-1/2\rangle = 2Sin\theta_-/2 Sin\theta_+/2 \tag{D.10}$$

So, we get the matrix form of V^+

$$V^+(h,h') = \begin{pmatrix} 0 & \sqrt{3}Sin\left(\frac{\theta_+ + \theta_-}{2}\right) \\ 2Sin(\theta_+/2)Sin(\theta_-/2) & 0 \end{pmatrix} \tag{D.11}$$

If $b = 0$ we have $\theta_+ = \theta_- \equiv \theta$ and

$$V^+(h,h') = \begin{pmatrix} 0 & \sqrt{3}Sin\theta \\ 1-Cos(\theta) & 0 \end{pmatrix} = \frac{\sqrt{3}}{2}Sin\theta\sigma^+ + \frac{1-Cos(\theta)}{2}\sigma^- \tag{D.12}$$

In the small θ limit we have:

$$V^+(h,h') \simeq \theta \begin{pmatrix} 0 & \sqrt{3} \\ \frac{\theta}{2} & 0 \end{pmatrix} \tag{D.13}$$

Notice how the spin-flip Mn-hole coupling vanishes if there is no LH-HH mixing.

D.3 Calculation of V^-

We now compute V^-:

$$V^-(h,h') = \sum_{j_z,j_z'} C_h(j_z)^* C_{h'}(j_z') \langle j_z|J^-|j_z'\rangle \tag{D.14}$$

Using

$$\langle j_z|J^-|j'_z\rangle = \delta_{j_z,j'_z+1}\sqrt{J(J+1)-j_z(j_z-1)} \tag{D.15}$$

we can get

$$V^-(h,h') = \sum_{j_z} C_h(j_z)^* C_{h'}(j_z+1)\sqrt{J(J+1)-j_z(j_z-1)} \tag{D.16}$$

It is apparent that the diagonal entries of V^- are zero. We now compute the offdiagonal elements:

$$\langle \Uparrow |V^-| \Downarrow\rangle = Sin\theta_+/2 Sin\theta_-/2\langle -1/2|J^-|+1/2\rangle = 2Sin\theta_+/2 Sin\theta_-/2 \tag{D.17}$$

$$\begin{aligned}\langle \Downarrow |V^-| \Uparrow\rangle &= Cos\theta_-/2 Sin\theta_+/2\langle -3/2|J^-|-1/2\rangle + Sin\theta_-/2 Cos\theta_+/2\langle +1/2|J^-|3/2\rangle \\ &= \sqrt{3}Sin\left(\frac{\theta_+ + \theta_-}{2}\right)\end{aligned} \tag{D.18}$$

So, we can write

$$V^-(h,h') = \begin{pmatrix} 0 & 2Sin(\theta_+/2)Sin(\theta_-/2) \\ \sqrt{3}Sin\left(\frac{\theta_+ + \theta_-}{2}\right) & 0 \end{pmatrix} \tag{D.19}$$

If $b = 0$ we have $\theta_+ = \theta_- \equiv \theta$ and

$$V^-(h,h') = \begin{pmatrix} 0 & 1-Cos(\theta) \\ \sqrt{3}Sin\theta & 0 \end{pmatrix} = \frac{\sqrt{3}}{2}Sin\theta\sigma^- + \frac{1-Cos(\theta)}{2}\sigma^+ \tag{D.20}$$

Appendix E

Steady state solution of the optical Bloch equation

In this appendix, we present a method to find the steady state solution of the Optical Bloch equation. The optical Bloch equation is given by

$$\frac{d\hat{\boldsymbol{\sigma}}}{dt} = \boldsymbol{M} \cdot \hat{\boldsymbol{\sigma}} \tag{E.1}$$

with a given initial state $\hat{\boldsymbol{\sigma}}_{\mathbf{0}}$ at $t = 0$ where $\boldsymbol{M}$ is a matrix defined by Equation 6.11 and Equation 6.12. For stationary cases, $t \to \infty$, we have $\frac{d\hat{\boldsymbol{\sigma}}}{dt} = 0$. Then we obtain a system of linear equations:

$$\boldsymbol{M} \cdot \hat{\boldsymbol{\sigma}} = 0 \tag{E.2}$$

The equation itself does not uniquely determine $\hat{\boldsymbol{\sigma}}$ in general because the matrix $\boldsymbol{M}$ may be singular. We can see this because if it is singular, the set of equations in Equation E.2 are not linearly independent. Theorefore, we need more conditions to uniquely determine the steady state. We have two more constraint to take advantage, the normalization condidtion $\sum_i \sigma_{ii} = 1$ and the initial condition $\hat{\boldsymbol{\sigma}}|_{t=0} = \hat{\boldsymbol{\sigma}}_{\mathbf{0}}$. If the rank of matrix $\boldsymbol{M}$ is smaller than the dimension (number of columns) of $\boldsymbol{M}$, it is possible to use the normalization condition to reach the steady state, if not, we need to use the initial states. Here we introduce a technique to get the steady state using the initial state $\hat{\boldsymbol{\sigma}}|_{t=0} = \hat{\boldsymbol{\sigma}}_{\mathbf{0}}$. It can be generally used to get steady state of one order linear differential equation groups.

We fist use the singular value decomposition of $\boldsymbol{M}$

$$\boldsymbol{M} = \boldsymbol{U}\boldsymbol{D}\boldsymbol{V}^{\boldsymbol{T}} \tag{E.3}$$

where $\boldsymbol{U}$ and $\boldsymbol{V}$ are orthogonal matrices and $\boldsymbol{D}$ is a diagonal matrix. The diagonal elements of $\boldsymbol{D}$ are called **singular values**. All singular values are zero or positive and

the diagonal elements of $\boldsymbol{D}$ are in descending order. Equation E.2 can be written as

$$\frac{d\boldsymbol{z}}{dt} = \boldsymbol{D}\boldsymbol{y} \tag{E.4}$$

where $\boldsymbol{z} = \boldsymbol{U}^{\boldsymbol{T}}\boldsymbol{P}$, $\boldsymbol{y} = \boldsymbol{V}^{\boldsymbol{T}}\boldsymbol{P}$. Separating the null space (B) and the complementary space (A) of $\boldsymbol{D}$, it becomes

$$\frac{d}{dt}\begin{pmatrix} \boldsymbol{z}_A \\ \boldsymbol{z}_B \end{pmatrix} = \begin{pmatrix} \boldsymbol{D}_A & 0 \\ 0 & 0 \end{pmatrix}\begin{pmatrix} \boldsymbol{y}_A \\ \boldsymbol{y}_B \end{pmatrix} \tag{E.5}$$

Then we can get:

$$\frac{d\boldsymbol{z}_A}{dt} = \boldsymbol{D}_A\boldsymbol{y}_A, \qquad \frac{d\boldsymbol{z}_B}{dt} = 0 \tag{E.6}$$

$\boldsymbol{z}_A$ is a diagonal matrix whose diagonal elements are the nonzero singular values of $\boldsymbol{M}$. Since time derivative of $\boldsymbol{z}_B$ is zero, we obtain

$$\boldsymbol{z}_B(t) = \boldsymbol{z}_B(0) \tag{E.7}$$

at all time t. At $t \to \infty$, all time derivatives are zero and we also obtain

$$\frac{d\boldsymbol{z}_A(t\to\infty)}{dt} = \boldsymbol{D}_A\boldsymbol{y}_A(t\to\infty) = 0 \tag{E.8}$$

Considering $\boldsymbol{D}_A$ is a diagonal matrix with nonzero diagonal elements, we get

$$\boldsymbol{y}_A(t\to\infty) = 0 \tag{E.9}$$

Using

$$\boldsymbol{y} = \boldsymbol{V}^T\boldsymbol{P} = \boldsymbol{V}^T\boldsymbol{U}\boldsymbol{z} \equiv \boldsymbol{W}\boldsymbol{z} \tag{E.10}$$

We get

$$\begin{pmatrix} \boldsymbol{y}_A \\ \boldsymbol{y}_B \end{pmatrix} = \begin{pmatrix} \boldsymbol{W}_{AA} & \boldsymbol{W}_{AB} \\ \boldsymbol{W}_{BA} & \boldsymbol{W}_{BB} \end{pmatrix}\begin{pmatrix} \boldsymbol{z}_A \\ \boldsymbol{z}_B \end{pmatrix} \tag{E.11}$$

So, we get

$$\boldsymbol{y}_A(\infty) = \boldsymbol{W}_{AA}\boldsymbol{z}_A(\infty) + \boldsymbol{W}_{AB}\boldsymbol{z}_B(\infty) = 0 \tag{E.12}$$

We also get the equation for $\boldsymbol{z}_A(\infty)$

$$\boldsymbol{W}_{AA}\boldsymbol{z}_A(\infty) = -\boldsymbol{W}_{AB}\boldsymbol{z}_B(\infty) \tag{E.13}$$

$$\boldsymbol{z}_A(\infty) = -\boldsymbol{W}_{AA}^{-1}\boldsymbol{W}_{AB}\boldsymbol{z}_B(0) \tag{E.14}$$

Where we use the result that $\boldsymbol{z}_B$ is constant in time. The existance of W_{AA}^{-1} can be proved easily. Once we have $\boldsymbol{z}(\infty)$, we can find the steady state of $\boldsymbol{\sigma}$ using

$$\boldsymbol{\sigma}(t\to\infty) = \boldsymbol{U}\boldsymbol{z}(\infty) \tag{E.15}$$

Publication related to this thesis

1. "Modelling optical spin pumping of a single Mn atom in a CdTe quantum dot", C. L. Cao, L. Besombes and J. Fernández-Rossier, Journal of Physics: Conference Series 210 (2010) 012046

2. "Spin-phonon coupling in single Mn-doped CdTe quantum dot", C. L. Cao, L. Besombes and J. Fernndez-Rossier, PHYSICAL REVIEW B 84, 205305 (2011)

3. "Optical initialization, readout, and dynamics of a Mn spin in a quantum dot", C. Le Gall, R. S. Kolodka, C. L. Cao, H. Boukari, H. Mariette, J. Fernández-Rossier and L. Besombes, PHYSICAL REVIEW B 81, 245315 (2010)

4. "Theory of optical detection of single spin magnetic resonance in Mn-doped CdTe quantum dots", in preparation

5. "Optical probing and control of the spin state of two Mn atoms in a quantum dot", in preparation

E. STEADY STATE SOLUTION OF THE OPTICAL BLOCH EQUATION

References

[1] P. M. Koenraad and M. E. Flatte. **Single dopants in semiconductors**. *Nature*, **10**:91, 2011.

[2] C. Hirjibehedin, C.-Y. Lin, A. Otte, M. Ternes, C. P. Lutz, B. A. Jones, and A. J. Heinrich. **Large Magnetic Anisotropy of a Single Atomic Spin Embedded in a Surface Molecular Network**. *Science*, **317**:1199, 2007.

[3] S. Loth, K. von Bergmann, M. Ternes, and A. J. Heinrich A. F. Otte, C. P. Lutz. **Controlling the state of quantum spins with electric currents**. *Nature Physics*, **6**:340, 2010.

[4] F. Jelezko, T. Gaebel, I. Popa, A. Gruber, and J. Wrachtrup. **Observation of Coherent Oscillations in a Single Electron Spin**. *Phys. Rev. Lett.*, **92**:076401, 2004.

[5] L. Besombes, Y. Léger, L. Maingault, D. Ferrand, H. Mariette, and J. Cibert. **Probing the Spin State of a Single Magnetic Ion in an Individual Quantum Dot**. *Phys. Rev. Lett.*, **93**:207403, 2004.

[6] M. Goryca, T. Kazimierczuk, M. Nawrocki, A. Golnik, J. A. Gaj, P. Kossacki, P. Wojnar, and G. Karczewski. **Optical Manipulation of a Single Mn Spin in a CdTe-Based Quantum Dot**. *Phys. Rev. Lett.*, **103**:087401, 2009.

[7] A. Kudelski, A. Lemaître, A. Miard, P. Voisin, T. C. M. Graham, R. J. Warburton, and O. Krebs. **Optically Probing the Fine Structure of a Single Mn Atom in an InAs Quantum Dot**. *Phys. Rev. Lett.*, **99**:247209, Dec 2007.

[8] O. Krebs, E. Benjamin, and A. Lemaitre. **Magnetic anisotropy of singly Mn-doped InAs/GaAs quantum dots**. *Phys. Rev. B*, **80**:165315, 2009.

[9] L. Besombes, Y. Léger, J. Bernos, H. Boukari, H. Mariette, J.P. Poizat, J. Fernandez-Rossier, and R. Aguado. **Optical Probing of spin fluctuations of a single paramagnetic Mn atom in a semiconductor quantum dot**. *Phys. Rev. B*, **78**:125324, 2008.

REFERENCES

[10] C. Le Gall, L. Besombes, H. Boukari, R. Kolodka, J. Cibert, and H. Mariette. **Optical Spin Orientation of a Single Manganese Atom in a Semiconductor Quantum Dot Using Quasiresonant Photoexcitation**. *Phys. Rev. lett.*, **102**:127402, 2009.

[11] C. Le Gall, R. S. Kolodka, C. L. Cao, H. Boukari, H. Mariette, J. Fernández-Rossier, and L. Besombes. **Optical initialization, readout, and dynamics of a Mn spin in a quantum dot**. *Phys. Rev. B*, **81**:245315, 2010.

[12] A. V. Govorov, A. O.and Kalameitsev. **Optical properties of a semiconductor quantum dot with a single magnetic impurity: photoinduced spin orientation**. *Phys. Rev. B*, **71**:035338, 2005.

[13] C. L. CAO, L. Besombes, and J. Fernandez-Rossier. **Modelling optical spin pumping of a single Mn atom in a CdTe quantum dot**. *Journal of Physics: Conference Series*, **210**:0120406, 2010.

[14] L. Cywinski. **Optical orientation of a single Mn spin in a quantum dot: Role of carrier spin relaxation**. *Phys. Rev. B*, **82**:075321, 2010.

[15] Y. Léger, L. Besombes, L. Maingault, D. Ferrand, and H. Mariette. **Geometrical Effects on the Optical Properties of Quantum Dots Doped with a Single Magnetic Atom**. *Phys. Rev. Lett.*, **95**:047403, 2005.

[16] Y. Léger, L. Besombes, L. Maingault, D. Ferrand, and H. Mariette. **Hole spin anisotropy in single Mn-doped quantum dots**. *Phys. Rev. B*, **72**:241309, 2005.

[17] J. Fernández-Rossier. **Single-exciton spectroscopy of semimagnetic quantum dots**. *Phys. Rev. B*, **73**:045301, 2006.

[18] Mark Johnson and R. H. Silsbee. **Interfacial charge-spin coupling: Injection and detection of spin magnetization in metals**. *Phys. Rev. Lett.*, **55**:1790, Oct 1985.

[19] M. N. Baibich, J. M. Broto, A. Fert, F. Nguyen Van Dau, F. Petroff, P. Etienne, G. Creuzet, A. Friederich, and J. Chazelas. **Giant Magnetoresistance of (001)Fe/(001)Cr Magnetic Superlattices**. *Phys. Rev. Lett.*, **61**(21):2472, Nov 1988.

[20] G. Binasch, P. Grünberg, F. Saurenbach, and W. Zinn. **Enhanced magnetoresistance in layered magnetic structures with antiferromagnetic interlayer exchange**. *Phys. Rev. B*, **39**(7):4828, Mar 1989.

[21] Christian Kurtsiefer, Sonja Mayer, Patrick Zarda, and Harald Weinfurter. **Stable Solid-State Source of Single Photons**. *Phys. Rev. Lett.*, **85**:290, Jul 2000.

[22] B. E. Kane. **A silicon-based nuclear spin quantum compute**. *NATURE*, **393**:133, 1998.

[23] Y. Léger, L. Besombes, L. Maingault, and H. Mariette. **Valence-band mixing in neutral, charged, and Mn-doped self-assembled quantum dots**. *Phys. Rev. B*, **76**:045331, Jul 2007.

[24] C. Çelebi, J. K. Garleff, A. Yu. Silov, A. M. Yakunin, P. M. Koenraad, W. Van Roy, J.-M. Tang, and M. E. Flatté. **Surface Induced Asymmetry of Acceptor Wave Functions**. *Phys. Rev. Lett.*, **104**:086404, Feb 2010.

[25] I. Dyakonov Mikhail. *Spin Physics in Semiconductors*. Springer, 2008.

[26] Daniel Loss and David P. DiVincenzo. **Quantum computation with quantum dots**. *Phys. Rev. A*, **57**:120, Jan 1998.

[27] J.K. Furdyna. **Diluted magnetic semiconductors**. *J. Appl. Phys.*, **64**:R29, 1988.

[28] J.K.Furdyna and J.Kossut, editors. *Diluted Magnetic Semiconductors*, **25** of *Semiconductors and Semimetals*. Academic Press, Boston, 1988.

[29] J. Schneider, U. Kaufmann, W. Wilkening, M. Baeumler, and F. Köhl. **Electronic structure of the neutral manganese acceptor in gallium arsenide**. *Phys. Rev. Lett.*, **59**(2):240, Jul 1987.

[30] M. Linnarsson, E. Janzén, B. Monemar, M. Kleverman, and A. Thilderkvist. **Electronic structure of the GaAs:Mn_{Ga}scenter**. *Phys. Rev. B*, **55**(11):6938, Mar 1997.

[31] J. A. Gaj, R. Planel, and G. Fishman. **title**. *Solid State Communications*, **29**:435, 1979.

[32] A. Twardowski, P. Swiderski, M. von Ortenberg, and R. Pauthenet. **title**. *Solid State Communications*, **50**:509, 1984.

[33] H. Boukari, P. Kossacki, M. Bertolini, D. Ferrand, J. Cibert, S. Tatarenko, A. Wasiela, J. A. Gaj, and T. Dietl. **Light and Electric Field Control of Ferromagnetism in Magnetic Quantum Structures**. *Phys. Rev. Lett.*, **88**(20):207204, 2002.

[34] A. V. Chernenko, P. S. Dorozhkin, V. D. Kulakovskii, A. S. Brichkin, S. V. Ivanov, and A. A. Toropov. **Auger recombination of excitons in semimagnetic quantum dot structure in a magnetic field**. *Phys. Rev. B*, **72**(4):045302, Jul 2005.

[35] A. A. Maksimov, G. Bacher, A. McDonald, V. D. Kulakovskii, A. Forchel, C. R. Becker, G. Landwehr, and L. W. Molenkamp. **Magnetic polarons in a single diluted magnetic semiconductor quantum dot**. *Phys. Rev. B*, **62**(12):R7767, Sep 2000.

[36] J. Seufert, G. Bacher, M. Scheibner, A. Forchel, S. Lee, M. Dobrowolska, and J. K. Furdyna. **Dynamical Spin Response in Semimagnetic Quantum Dots**. *Phys. Rev. Lett.*, **88**(2):027402, Dec 2001.

[37] G. Mackh, W. Ossau, D. R. Yakovlev, A. Waag, G. Landwehr, R. Hellmann, and E. O. Göbel. **Localized exciton magnetic polarons in $Cd_{1-x}Mn_xTe$**. *Phys. Rev. B*, **49**(15):10248, Apr 1994.

[38] D. R. Yakovlev, K. V. Kavokin, I. A. Merkulov, G. Mackh, W. Ossau, R. Hellmann, E. O. Göbel, A. Waag, and G. Landwehr. **Picosecond dynamics of magnetic polarons governed by energy transfer to the Zeeman reservoir**. *Phys. Rev. B*, **56**(15):9782, Oct 1997.

[39] G. Bacher, A. A. Maksimov, H. Schömig, V. D. Kulakovskii, M. K. Welsch, A. Forchel, P. S. Dorozhkin, A. V. Chernenko, S. Lee, M. Dobrowolska, and J. K. Furdyna. **Monitoring Statistical Magnetic Fluctuations on the Nanometer Scale**. *Phys. Rev. Lett.*, **89**(12):127201, Aug 2002.

[40] P. S. Dorozhkin, A. V. Chernenko, V. D. Kulakovskii, A. S. Brichkin, A. A. Maksimov, H. Schoemig, G. Bacher, A. Forchel, S. Lee, M. Dobrowolska, and J. K. Furdyna. **Longitudinal and transverse fluctuations of magnetization of the excitonic magnetic polaron in a semimagnetic single quantum dot**. *Phys. Rev. B*, **68**(19):195313, Nov 2003.

[41] A. Hundt, J. Puls, and F. Henneberger. **Spin properties of self-organized diluted magnetic $Cd_{1-x}Mn_xSe$ quantum dots**. *Phys. Rev. B*, **69**(12):121309, Mar 2004.

[42] D. J. Norris, Nan Yao, F. T. Charnock, and T. A. Kennedy. **High-Quality Manganese-Doped ZnSe Nanocrystals**. *Nanoletters*, **1**:3, 2001.

[43] S. C. Erwin, L. Zu, M. I. Haftel, A. L. Efros, T. A. Kennedy, and D. J. Norris. **Doping semiconductor nanocrystals**. *Nature*, **436**:91, 2005.

[44] A. K. Bhattacharjee and J. Pérez-Conde. **Optical properties of paramagnetic ion-doped semiconductor nanocrystals**. *Phys. Rev. B*, **68**(4):045303, Jul 2003.

[45] P. I. Archer, S. A. Santangelo, and D. R. Gamelin. **Direct Observation of sp-d Exchange Interactions in Colloidal Mn^{2+} and Co^{2+} Doped CdSe Quantum Dots**. *Nanoletters*, **7**:1037, 2007.

[46] R. Beaulac, L. Schneider, P.I. Archer, G. Bacher, and D.R. Gamelin. **Light-Induced Spontaneous Magnetization in Doped Colloidal Quantum Dots**. *Science*, **325**(5943):973, 2009.

[47] S. Mackowski, T. Gurung, H. E. Jackson, L. M. Smith, and G. Karczewski. **Exciton-controlled magnetization in single magnetic quantum dots**. *Appl. Phys. Lett.*, **87**:072502, 2005.

[48] T. Clément, D. Ferrand, L. Besombes, H. Boukari, and H. Mariette. **Dynamical equilibrium between magnetic ions and photocarriers in low Mn-doped single quantum dots**. *Phys. Rev. B*, **81**(15):155328, Apr 2010.

[49] Y. Léger, L. Besombes, J. Fernández-Rossier, L. Maingault, and H. Mariette. **Electrical Control of a Single Mn Atom in a Quantum Dot**. *Phys. Rev. Lett.*, **97**(10):107401, Sep 2006.

[50] F. Tinjod, B. Gilles, S. Moehl, K. Kheng, and H. Mariette. **II-VI quantum dot formation induced by surface energy change of a strained layer**. *Appl. Phys. Lett.*, **82**:4340, 2003.

[51] L. Maingault, L. Besombes, Y. Léger, C. Bougerol, and H. Mariette. **Inserting one single Mn ion into a quantum dot**. *Appl. Phys. Lett.*, **89**:193109, 2006.

[52] M. M. Glazov, Ivchenko, E. L., L. Besombes, Y. Léger, L. Maingault, and H. Mariette. **Fine structure of exciton excited levels in a quantum dot with a magnetic ion**. *Phys. Rev. B*, **75**:205313, 2007.

[53] L. Besombes, Y. Léger, J. Bernos, H. Boukari, H. Mariette, J.P. Poizat, J. Fernandez-Rossier, and R. Aguado. **Optical probing of spin fluctuations of a single paramagnetic Mn atom in a semiconductor quantum dot**. *Phys. Rev. B*, **78**:125324, 2008.

[54] R. C. Myers, M. H. Mikkelsen, J.-M. Tang, A. C. Gossard, M. E. Flatt, and D. D. Awschalom. **Zero-field optical manipulation of magnetic ions in semiconductors**. *Nature materials*, **7**:203, 2008.

[55] M. Qazzaz, G. Yang, S.H. Xin, L. Montes, H. Luo, and J.K. Furdyna. **Electron paramagnetic resonance of Mn2+ in strained layer semiconductor superlattices**. *Solid State Communications*, **96**:405, 1995.

[56] M. Goryca, D. Ferrand, P. Kossacki, M. Nawrocki, W. Pacuski, W. Maslana, J.A. Gaj, S. Tatarenko, J. Cibert, T. Wojtowicz, and G. Karczewski. **Magnetization Dynamics Down to a Zero Field in Dilute (Cd,Mn)Te Quantum Wells**. *Phys. Rev. Lett.*, **102**:046408, 2009.

[57] J. Dreiser, M. Atatre, C. Galland, T. Mller, A. Badolato, and A. Imamoglu. **Optical investigations of quantum dot spin dynamics as a function of external electric and magnetic fields**. *Phys. Rev. B*, **77**:075317, 2008.

[58] JB. D. Gerardot, D. Brunner, P. A. Dalgarno, P. Ohberg, S. Seidl, M. Kroner, K. Karrai, N. G. Stoltz, P. M. Petroff, and R. Warburton. **Optical pumping of a single hole spin in a quantum dot**. *Nature*, **451**:441, 2008.

[59] E.B. Flagg, A. Muller, J.W. Robertson, S. Founta, D. G. Deppe, M. Xiao, W. Ma, G. J. Salamo, and C.K. Shih. **Resonantly driven coherent oscillations in a solid-state quantum emitter**. *Nature Physics*, **5**:203, 2009.

[60] B. Patton, W. Langbein, U. Woggon, L. Maingault, and H. Mariette. **Time- and spectrally-resolved four-wave mixing in single CdTe/ZnTe quantum dots**. *Phys. Rev. B*, **73**:235354, 2006.

[61] M. Qazzaz, G. Yang, S.H. Xin, L. Montes, H. Luo, and J.K. Furdyna. **Electron paramagnetic resonance of Mn2+ in strained-layer semiconductor superlattices**. *Solid State Communications*, **96**:405, 1995.

[62] E. Tsitsihvili, R.V. Baltz, and H. Kalt. **Exciton spin relaxation in single semiconductor quantum dots**. *Phys. Rev. B*, **67**:205330, 2003.

[63] A. O. Govorov. **Optical probing of the spin state of a single magnetic impurity in a self-assembled quantum dot**. *Phys. Rev. B*, **70**:035321, 2004.

[64] J.M. Luttinger and W. Kohn. **Motion of Electrons and Holes in Perturbed Periodic Fields**. *Phys. Rev. B*, **97**:869, 1955.

[65] D. Broido and L. J. Sham. **Effective masses of holes at GaAs-AlGaAs heterojunctions**. *Phys. Rev. B*, **31**:888, 1985.

[66] Lok C. Lew Yan Voon and Morten Willatzen. *The k·p Method Electronic Properties of Semiconductors*. Springer, 1990.

[67] F. V. Kyrychenko and J. Kossut. **Diluted magnetic semiconductor quantum dots:An extreme sensitivity of the hole Zeeman splitting on the aspect ratio of the confining potential**. *Phys. Rev. B*, **70**:205317, 2004.

[68] Peter Yu and Manuel Cardona. *Fundammentals of Semiconductors*. Springer, 1996.

[69] Y. Léger, L. Besombes, L. Maingault, and H. Mariette. **Valence-band mixing in neutral, charged, and Mn-doped self-assembled quantum dots**. *Phys. Rev. B*, **76**:045331, 2007.

[70] A. K. Bhattarjee and C. Benoit a la Guillaume. **Model for the Mn acceptor in GaAs**. *Solid State Communications*, **113**:17, 1999.

[71] J. Fernandez-Rossier and R. Aguado. **Single-Electron Transport in Electrically Tunable Nanomagnets**. *Phys. Rev. Lett.*, **98**:106805, 2007.

[72] F. Qu and Hawrylack P. **Theory of electron mediated Mn-Mn interactions in quantum dots**. *Phys. Rev. Lett*, **96**:157201, 2006.

[73] D. E. Reiter, T.M. Kuhn, and V. M. Axt. **All-Optical Spin Manipulation of a Single Manganese Atom in a Quantum Dot**. *Phys. Rev. Lett.*, **102**:177403, 2009.

[74] Claude Cohen-Tannoudji, Jacques Dupont-Roc, and Gilbert Grynberg. *Atom-Photon Interactions: Basic Process and Applications*. John Wiley, 1992.

[75] E. M. Chudnovsky, D. A. Garanin, and R. Schilling. **Universal mechanism of spin relaxation in solids**. *Phys. Rev. B*, **72**:094426, 2005.

[76] L. M. Woods, T. L. Reinecke, and R. Kotlyar. **Hole spin relaxation in quantum dots**. *Phys. Rev. B*, **69**:125330, 2004.

[77] J. C. Merle, R. Sooryakumar, and M. Cardona. **Resonant Brillouin scattering in cadmium telluride**. *Phys. Rev. B*, **30**:3261, 1984.

[78] J. G. Collins, G. K. White, J. A. Birch, and T. F. Smith. **Thermal expansion of ZnTe and HgTe and heat capacity of HgTe at low temperatures**. *J. Phys. C*, **13**:1649, 1980.

[79] T. Strutz, A. M. Witowski, and P. Wyder. **Spin-lattice relaxation at high magnetic fields**. *Phys. Rev. Lett.*, **68**:3912, 1992.

[80] L. M. Woods, T. L. Reinecke, and R. Kotlyar. **Hole spin relaxation in quantum dots**. *Phys. Rev. B*, **69**:125330, Mar 2004.

[81] E. Tsitsishvili, R. v. Baltz, and H. Kalt. **Exciton-spin relaxation in quantum dots due to spin-orbit interaction**. *Phys. Rev. B*, **72**:125333, 2005.

[82] K. Roszak, V. M. Axt, T. Kuhn, and P. Machnikowski. **Exciton spin decay in quantum dots to bright and dark states**. *Phys. Rev. B*, **76**:195324, 2007.

[83] W.H.Kleiner and L.M.Roth. **Deformation potential in germanium from optical absorption lines for exciton formation**. *Phys. Rev. B*, **2**:334, 1959.

[84] U. Bockelmann. **Phonon scattering between zero-dimensional electronic states: Spatial versus Landau quantization**. *Phys. Rev. B*, **50**:17271, Dec 1994.

[85] Al. V. Khaetskii and Y. V. Nazarov. **Spin relaxation in semiconductor quantum dots**. *Phys. Rev. Lett.*, **64**:125316, 2001.

[86] S. I. Kiselev, J. C. Sankey, I. N. Krivorotov, N. C. Emley, R. J. Schoelkopf, R. A. Buhrman, and D. C. Ralph. **Deformation Potential in Germanium from Optical Absorption Lines for Exciton Formation**. *Nature*, **425**:380, 2003.

[87] C. Le Gall, A. Brunetti, H. Boukari, and L. Besombes. **Optical Stark effect and dressed exciton states in a Mn-Doped CdTe quantum dot**. *Phys. Rev. Lett.*, **107**:057401, 2011.

[88] S.H. Autler and C. H. Townes. **Stark Effect in Rapidly Varying Fields**. *Phys. Rev.*, **100**:703, 1955.

[89] S. J. Boyle, A. J. Ramsay, A. M. Fox, M. S. Skolnick, A. P. Heberle, and M. Hopkinson. **Beating of Exciton-Dressed States in a Single Semiconductor** InGaAs/GaAs **Quantum Dot**. *Phys. Rev. Lett.*, **102**:207401, 2009.

[90] B. R. Mollow. **Stimulated Emission and Absorption near Resonance for Driven Systems**. *Phys. Rev. A*, **5**:2217, 1972.

[91] M. P. van Exter, J. Gudat, G. Nienhuis, and D. Bouwmeester. **Spin quantum jumps in a singly charged quantum dot**. *Phys. Rev. A*, **80**:023812, 2009.

[92] Y. Léger, L. Besombes, L. Maingault, and H. Mariette. **Valence-band mixing in neutral, charged, and Mn-doped self-assembled quantum dots**. *Phys. Rev. B*, **76**:045331, 2007.

Résumé

Nous avons étudié la dynamique de spin d'un atome de Mn inséré dans une boite quantique CdTe. Nos résultats montrent que la relaxation de spin du Mn est plus rapide lorsque la boite quantique contient un exciton. Ceci peut permettre une orientation optique du spin du Mn. Le mélange de bande de valence est le paramètre essentiel permettant la relaxation rapide du spin du Mn dans le champ d'échange de l'exciton. Ce mélange de bande de valence est controlé par la forme et les contraintes dans la boite quantique. L'influence de ces paramètres sur la dynamique du pompage optique a été analysée en détail. Nos simulations du pompage optique sont en bon accord avec les expériences. La dynamique cohérente d'un Mn individuel a aussi été étudiée. L'influence sur le pompage optique de la dynamique cohérente du spin électronique et nucléaire est discutée. Nous avons montré que le couplage entre spin électronique et nucléaire peut être contrôlé optiquement permettant une manipulation du spin du Mn. Nous avons finalement montré que la combinaison d'une excitation résonante optique et micro-onde peut être utilisée pour détecter optiquement la résonance magnétique d'un Mn dans une boite quantique CdTe.

Mots-clés: Boîte quantique, semiconducteur magnétique dilué, dynamique de spin.

Abstract

We have studied the spin dynamics of an individual Mn atom embedded a CdTe quantum dot. Our results show that the Mn spin relaxation is faster when the quantum dot contains an exciton. This can result in an optical orientation of the Mn spin. The valence band mixing is the critical parameter for the fast relaxation rates of the Mn spin in the exchange field of the exciton. This valence band mixing is controlled by the shape and strain of the quantum dot. The influence of these parameters on the optical pumping dynamics were analyzed in detail. Our simulation of optical pumping are in good agreement with experiments. The coherent dynamics of an individual Mn spin was also investigated. We discussed the influence of the coherent dynamics of the coupled electronic and nuclear spins on the optical pumping. We have shown that optically controlled coupling between electronic and nuclear spins could be used for Mn spin switching. We finally demonstrated that the combination of resonant laser and microwave fields can be used to optically detect the magnetic resonance of a Mn spin in a CdTe quantum dot.

Keywords: Quantum dot, diluted magnetic semiconductor, spin dynamics.